INFLUENCE OF THE SHEAR PARAMETER ON LARGE- AND SMALL-SCALE STATISTICS IN HOMOGENEOUS TURBULENT SHEAR FLOW

A Dissertation

Presented to the Faculty of the Graduate School

of Cornell University

in Partial Fulfillment of the Requirements for the Degree of

Doctor of Philosophy

by

Juan Camilo Isaza Betancourt

May 2009

INFLUENCE OF THE SHEAR PARAMETER ON LARGE- AND SMALL-SCALE STATISTICS IN HOMOGENEOUS TURBULENT SHEAR FLOW

Juan Camilo Isaza Betancourt, Ph.D.

Cornell University 2009

This dissertation consist of three parts.

The first part is a study of the asymptotic behavior of large-scale velocity statistics in an homogeneous turbulent shear flow using direct numerical simulations (DNS) of the incompressible Navier-Stokes equations on a 512^3 grid, and with viscous rapid distortion theory (vRDT). We use a novel pseudo-spectral algorithm that allows us to set the initial value of the shear parameter in the range 3–30 without the shortcomings of previous numerical approaches. We find there is an explicit dependence of the early-time behaviour on the initial value of the shear parameter. Moreover, the long-time asymptotes of large-scale quantities such as the ratio of the turbulent kinetic energy production rate over dissipation rate, the Reynolds stress anisotropic tensor, and the shear parameter itself depend *sensitively* on the initial value of the shear parameter.

In the second part, motivated by the numerical results described above, the sensitivity to the initial value of the shear parameter and Reynolds number is investigated for the first time in a wind tunnel. Using an active grid, the initial value of Reynolds number based on the Taylor microscale is varied over the range $100 \leq R_\lambda \leq 250$. The shear is generated using screens of different solidities followed by a series of straightening channels (Garg and Warhaft (1998)), allowing us to vary the initial value of the shear parameter over the modest range $6 \leq S_0^* \leq 12$.

We find that the longtime behavior of the shear parameter depends on its initial value over the non-dimensional time interval $5 \leq \mathcal{S}t \leq 25$, but is less sensitive to the initial value of the Reynolds number. The ratio of the turbulent kinetic energy production over dissipation rate appears to show a similar dependence on the initial value of the shear parameter, but there is more significant scatter in the data. We find that the turbulent kinetic energy grows with downstream distance, in agreement with previous work, and that its growth rate too is a stronger function of the initial shear parameter than the initial Reynolds number.

The last part consist of a study of the influence of the shear parameter on velocity-gradient statistics such as the rate-of-strain tensor and vorticity. We find that the tails of the probability distribution function of components of the vorticity vector and the rate-of-strain tensor approach a Gaussian distribution with increasing shear parameter. Results are compared with the predictions of vRDT. We also find that increasing the shear parameter causes the main contribution to enstrophy production to shift from the nonlinear terms to the rapid terms (terms that involve the mean strain and vorticity) due to the alignments of the vorticity and the rate-of-strain field.

BIOGRAPHICAL SKETCH

Juan Camilo Isaza Betancourt was born in Colombia in 1973. In 1997, Juan obtained his Bachelor of Science in Mechanical Engineering from *Universidad del Norte*, Barranquilla, Colombia. Following his graduation, the author received a scholarship from *Universidad de Los Andes*, Bogota, Colombia to pursue a Master of Science in Mechanical Engineering. After graduating in 1999, the author worked as research engineer for the industry in Colombia. In August 2003 he received a Fulbright Fellowship and joined the Sibley School of Mechanical and Aerospace Engineering at Cornell University to pursue the degree of Doctor of Philosophy. During his studies, he received a Master of Science from Cornell University in 2007.

Esta disertación esta dedicada a mi esposa, quien siempre me ha apoyado en la busqueda de mis sueños

ACKNOWLEDGEMENTS

I especially thank my advisor, Professor Lance R. Collins for his patience, guidance and mentorship during my research. His enthusiasm for turbulence and fluid mechanics are an example to follow. Prof. Collins was always accessible and willing to help during the course of my studies despite his hectic schedule as department director. This research would have not been possible without his assistance. He made my research life at Cornell a very rewarding experience.

I would like to thank the other two members of my Special Committee, Professor Zellman Warhaft and Professor Sidney Leibovich. Professor Warhaft introduce me to the world of experiments in turbulence. His guidance, academic discussions and help during the experiments are greatly appreciated. I had the opportunity of attending a course taught by Professor Leibovich. I will always be grateful for teaching me how to apply to fluid mechanics all the perturbations and asymptotic technics I learnt during my math classes. I would also like to thank Professor S. B. Pope for valuable discussions and suggestions during my studies.

I would like to thank the Fulbright Commission and *Universidad EAFIT*, Medellin, Colombia for their support. Thanks to David E. Sonnefeld for providing the time and support to complete this dissertation.

My deepest gratitude to my parents Franklin and Beatriz who taught me responsibility. My father for setting the example of dedication to a life of work. My mother for her unconditional and constant support when I encounter difficulties. There is no words to describe her everlasting love for me. Specially, I would like to thank Olga and Alberto. They took me into their family since the moment I met them. Their generosity, example and wisdom will be always be treasured. I thank my sister Claudia for her words of advice.

In my daily work at Cornell I have been blessed with a friendly and cheerful group of fellow students. In particular, I would like to thank Vaithianathan T. my office mate during my first years in Ithaca. Nicole Sharp for teaching me the art of making hot wires and her help during my experiments. Juan Salazar for all the enlightening discussions about turbulence, class work and fluid mechanics. Kyle Brucker for a copy of his spectral code.

Special thanks to all my friends from Puerto Rico. My time at Cornell would not have been so enjoyable without them. The BBQs, parties, boxing nights will always be cherished. In particular, Felipe Santiago, a very good friend, whose friendship has supported, enlightened, and entertained my life in Ithaca. Nelson Morales who is friend always willing to lend a hand. Wilhelm Hernandez, the first Puerto Rican I met and a fellow student during my first year in Ithaca. I will always remember the time we spent riding horses in Colombia.

My friends German and Pilar. They provided uncountable times of entertainment.

I would like to thank my wonderful wife, Eliana Nossa. Her love, encouragement, companionship and support had made our years together a pleasure. Finally, to God who makes all possible.

TABLE OF CONTENTS

LIST OF TABLES

LIST OF FIGURES

CHAPTER 1

ON THE ASYMPTOTIC BEHAVIOUR OF LARGE-SCALE TURBULENCE IN HOMOGENEOUS SHEAR FLOW[1]

1.1 Introduction

Homogeneous turbulent shear flow (hereafter HTSF) is among the canonical flows considered to be the 'building blocks' of turbulence. It is the next step up in complexity from isotropic turbulence. This flow has many of the features found in wall-bounded flows, e.g., off-diagonal Reynolds stress components, turbulence production and hairpin vortices, without introducing the complexities of a fully inhomogenous turbulence. Consequently, this flow has been widely investigated in experiments, direct numerical simulations (hereafter DNS) and theoretically. Despite the attention it has received over the past 40+ years, there remain fundamental questions about the longtime behaviour of the flow that have yet to be satisfactorily resolved. In this study, we consider these issues using DNS and by applying rapid distortion theory.

In the classical view of HTSF (Tavoularis (1985); see also §5.4.5 in Pope (2000) for a simple derivation), the turbulent kinetic energy at long times grows according to

$$q^2(t) = q_r^2 \exp(\sigma \mathcal{S} t) \tag{1.1}$$

where $q^2 \equiv \overline{u_i' u_i'}$ is twice the turbulent kinetic energy, $\mathcal{S}$ is the uniform mean shear rate, σ is a yet-undefined constant, and the subscript '$_r$' indicates a reference value. Much of the literature supports $\sigma > 0$, although, as noted below, this is not universal. As noted by Jacobitz et al. (1997) for stratified turbulence and

[1] submitted to the Journal of Fluid Mechanics

Schumacher et al. (2003) in their study of the small scales, two initial parameters characterize HTSF: the Reynolds number (here we use the Reynolds number based on the Taylor microscale, $R_\lambda \equiv q^2\sqrt{5/(3\epsilon\nu)}$, where ϵ is the dissipation rate and ν is the kinematic viscosity of the fluid); and the non-dimensional 'shear parameter' defined as $S^* \equiv \mathcal{S}q^2/\epsilon$. The latter is a measure of the strength of the shear relative to the turbulence time scale—$S^* \gg 1$ implies strong shear (note that $S^* \sim 30$ in a boundary layer). Technically, asymptotically strong shear would imply the more stringent condition: $\mathcal{S}\tau_\eta \gg 1$, where $\tau_\eta \equiv (\nu/\epsilon)^{1/2}$ is the Kolmogorov time scale, or equivalently $S^* \gg R_\lambda$. This condition is rarely satisfied in DNS or experiments due to different, but important intrinsic limitations to both approaches.

Experimental measurements of a nearly HTSF are often made in a wind tunnel or water tunnel by passing turbulence through a screen with variable solidity that produces a nearly uniform mean velocity gradient across the tunnel. The resulting turbulence is not perfectly homogeneous, as the turbulence across any cross section of the tunnel will have evolved for a period of time that too varies across the tunnel with the mean velocity. Hence there will be some turbulent transfer of kinetic energy in the direction of the mean gradient. The assumption made in most experiments is that this spatial diffusion of turbulent energy is small as compared to the source and sink terms. This assumption can be justified by computing the turbulent flux. Indeed, the turbulent flux is one or more orders of magnitude below the source and sink terms (Harris et al. (1977)).

Whether the asymptotic state of HTSF is a function of the initial value of either or both parameters remains controversial. Experiments have generally yielded $\sigma > 0$ (e.g., Harris et al. (1977); Tavoularis and Corrsin (1981); Rohr et al. (1988); Tavoularis and Karnik (1989); DeSouza et al. (1995)), although with values that

vary with the flow parameters (e.g., Garg and Warhaft (1998)) and possibly the apparatus (Rose (1966, 1970); Champagne et al. (1970)). Tavoularis (1985) attempted to explain these discrepancies based on the initial value of the mean shear with some success.

Rohr et al. (1988) measured turbulence intensities in a water tunnel designed to allow them to vary the mean shear while keeping the center line velocity of the tunnel constant. They found that the turbulence intensities grew faster for the higher shear rates at the same centerline speed. They also were able to vary the initial integral length scale of the turbulence and found that this too influenced the growth rate of the turbulence intensity (i.e., σ). Notice that both of these results are an indirect indication of sensitivity to the shear parameter since it could have been defined in terms of the integral length scale as follows: $S^* = \mathcal{S}L_{11}/q$, where L_{11} is the integral length scale. Similar results were obtained by Rose (1970), although subsequent concerns have been raised about the relatively short test section ($\mathcal{S}t \leq 3$). So while trends indicate some sensitivity to the shear parameter, it is clear that a comprehensive understanding of how σ depends upon the two initial parameters has yet to be developed.

There are two important challenges to the experiments that, to some extent, have limited their ability to address this question. First, the maximum value of $\mathcal{S}t$ that can be achieved is limited by the length of the wind tunnel to ≤ 20 for most experiments. It is difficult to tell if the asymptotic regime has been fully achieved. Some argue that it depends on the number of large eddy turnover times that have transpired, which is even more limited by the length of the tunnel. Second, while it is possible to explore a broad range of Reynolds numbers using an active grid (Mydlarski and Warhaft (1996)), it is difficult in the wind tunnel to vary the shear

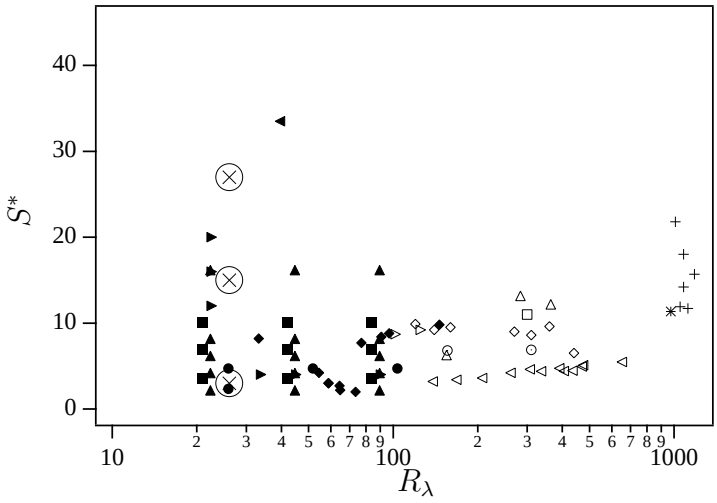

Figure 1.1: Initial values of the Reynolds number and the shear parameter for previous DNS (solid symbols) and operational values for previous experiments (open symbols) of homogeneous turbulent shear flow. DNS: ● Rogers et al. (1986), ◀ Lee et al. (1990), ▶ Jacobitz et al. (1997), ▲ Shih et al. (2000), ♦ Schumacher (2004) and ■ Yu and Girimaji (2005). Experiments: ○ Champagne et al. (1970), △ Tavoularis and Corrsin (1981), □ Harris et al. (1977), ◇ Tavoularis and Karnik (1989), + DeSouza et al. (1995), ⊙ Garg and Warhaft (1998), ∗ Shen and Warhaft (2000), ◁ Ferchichi and Tavoularis (2000) and ▷ Rohr et al. (1988). The new runs from this study are designated by ⊗.

parameter over a wide range. With the exception of DeSouza et al. (1995), the experiments are generally limited to $S^* \leq 10$, which while greater than unity, cannot be considered asymptotically large.

DNS of HTSF likewise have yielded mixed results. For example, Jacobitz et al. (1997) and Jacobitz and Sarkar (1999) in DNS studies of uniformly sheared, stratified flows (at their lowest Richardson number) found that the asymptotic state of the flow depended sensitively on both the Reynolds number and the shear parameter. At low values of S_0^* the turbulence grew (i.e., $\sigma > 0$), but at larger values of S_0^* the turbulence decayed for all the initial values of Reynolds number they investigated. Shih et al. (2000) found a similar result, but argued that the sensitivity to

S_0^* vanishes at large enough values of the Reynolds number ($R_\lambda \geq 80$). Lee et al. (1990) did not consider this question directly, but in figure 4 of their paper they showed the asymptote for S^* to be sensitive to its initial value, S_0^*.

There have been numerical studies of flows closely related to HTSF as well. Yu and Girimaji (2005) applied a lattice Boltzmann algorithm to turbulent Couette flow and considered the early-time solution far from the boundaries to be similar to HTSF. They observed exponential growth of the kinetic energy and found only a weak sensitivity of the flow to S_0^* and a much stronger sensitivity to the initial value of R_λ. Schumacher (2004) studied turbulent flow confined between two free-slip planes subject to a body force that varies linearly from the top plane to the bottom. The resulting flow achieved a steady state at long times, implying $\sigma = 0$. Of course, there is likely significant influence of the bounding planes on the longtime behaviour of the turbulence, and hence this particular result may be an artifact of the flow specification.

Figure 1.1 shows a compilation of the S^*–R_λ parameter space that has been explored by DNS (solid symbols) and experiments (open symbols) in the literature, with the newest runs from this study designated by $\otimes$. For DNS, the standard definitions of S^* and R_λ apply, whereas for the experiments, various surrogates have been employed. For example, ϵ has been obtained as the imbalance of the turbulent kinetic energy production and growth (Harris et al. (1977); Tavoularis and Corrsin (1981); Tavoularis and Karnik (1989); DeSouza et al. (1995)), or based on some combination of velocity derivatives (Rohr et al. (1988); Garg and Warhaft (1998); Shen and Warhaft (2000)). The Taylor microscale was often estimated using one component of velocity, $\lambda = \overline{u^2}/\overline{(\partial u/\partial x)^2}$. An exception is DeSouza et al. (1995), who used the following empirical estimate: $\lambda^2 = 12\nu q^2/\epsilon$. In some cases

(Garg and Warhaft (1998); Shen and Warhaft (2000)), the definition of S^* reported in the paper differed from our definition. To compare with the other experiments, we recalculated those quantities using the approximation $q^2 = \overline{u^2} + 2\overline{v^2}$. However, this correction could not be applied to the data of Ferchichi and Tavoularis (2000), as they only reported one component of the velocity; instead we assumed $q^2 = 2\overline{u^2}$.

Despite these unavoidable inconsistencies in the parameter definitions, figure 1.1 shows reasonably well the regions of the parameter space that have been explored by simulations and experiments. In particular, it is apparent that DNS has had difficulty exploring both high Reynolds number and high shear parameter. Most DNS are based on the algorithm by Rogallo (1981), which requires remeshing at odd integer values of $\mathcal{S}t$ (i.e., $\mathcal{S}t = 1$, 3, 5, etc.). Remeshing, combined with dealiasing leads to a sudden loss in both the turbulent kinetic energy and turbulent energy dissipation rate. For higher shear rates, this loss can be as large as 20–40%. Lee et al. (1990) reached $S_0^* \sim 30$ using the Rogallo code by turning off the remeshing step. They argued that at high shear rates, the adverse effect of the frequent remeshing exceeds the benefits, particularly in light of the relatively short physical time of the simulation. In contrast, experiments are able to span a much broader range of Reynolds numbers, but they too are limited to a modest range of the shear parameter.

The shortcomings of the Rogallo algorithm at high S_0^* have been addressed by a new algorithm (Brucker et al. (2007)). Their approach too is based on a pseudospectral algorithm for the Navier-Stokes equations; however, the field variables in physical space are evaluated on an orthogonal mesh in the laboratory frame instead of the deforming mesh used by the Rogallo algorithm. The resulting DNS has smaller aliasing errors, and no jumps in the kinetic energy or dissipation rate,

since the remeshing step has been eliminated. In this investigation, we apply the new algorithm to a series of 512^3 DNS of shear flows with initial shear parameters over the range 3–30. Owing to the stringent resolution requirements enforced in this study (see §1.3.3 for details), the range of Reynolds numbers was relatively small ($26 \leq R_\lambda \leq 63$); however, the results were found to depend only weakly on this parameter. We present new findings for the asymptotic behaviour of the large-scale quantities, as well as attempt to sort out the inconsistencies in the previous literature.

Additionally, to assist in the interpretation of the high-shear results, we apply rapid distortion theory (hereafter RDT) to HTSF. Scaling arguments suggest that for cases in which the shear parameter is high, the nonlinear turbulence–turbulence interactions can be neglected from the equation of motion. A review of the theory can be found in Savill (1987) and more recently in Hunt and Carruthers (1990). RDT has been applied to *inviscid* HTSF by Moffat (1967), Townsend (1970), and more recently by Rogers (1991), who developed analytical expressions for the short- and long-time behaviour of the Reynolds stress components. However, the Reynolds number and shear parameter are not defined in the inviscid limit, and hence this RDT analysis cannot be used to investigate the significance of these parameters on the longtime behaviour of the turbulence. RDT has also been applied to *viscous* HTSF (Deissler (1961); Fox (1964); Thacker et al. (1999)); however, their results do not consider the significance of the shear parameter on the turbulence evolution.

In this study, we obtain analytical expressions for the short-time behaviour of the turbulent Reynolds stresses, kinetic energy production over dissipation rate, and the shear parameter. The results explicitly show how the two parameters

influence the short-term behaviour. Second, we numerically evaluate the viscous RDT integrals to obtain predictions for the asymptotic behaviour of HTSF at long times. Comparing viscous RDT to DNS helps explain why nonlinear effects eventually become important, and suggests possible modifications to the theory that could account for these effects.

The paper is organized as follows. Section 1.2 discusses the governing equations for HTSF, with the equations for the large-scale turbulence statistics provided in §1.2.4. Results from the DNS are presented in §1.3 followed by the viscous RDT analysis in §1.4. Conclusions are given in §1.5.

1.2 Homogeneous Turbulent Shear Flow

1.2.1 Governing Equations

We are interested in the flow of an incompressible fluid in a periodic box of length 2π in each direction. The governing equations for the fluid are

$$\frac{\partial u_i}{\partial x_i} = 0 \ , \tag{1.2}$$

$$\frac{\partial u_i}{\partial t} + u_j \frac{\partial u_i}{\partial x_j} = - \frac{\partial (p/\rho)}{\partial x_i} + \nu \frac{\partial^2 u_i}{\partial x_j \partial x_j} \ , \tag{1.3}$$

where u_i is the velocity vector, ρ is the fluid density, ν is the kinematic viscosity, and p is the pressure.

Introducing the Reynolds decomposition, $u_i = U_i + u_i'$ and $p = P + p'$, where capital letters represent mean quantities and prime letters are the fluctuating quantities. We define $U_i = (\mathcal{S} x_2, 0, 0)$, where $\mathcal{S}$ is the spatially uniform mean shear rate

imposed on the flow. Invoking homogeneity and combining and simplifying the terms that involve the mean flow, the final form of the evolution equation for the fluctuating velocity is

$$\frac{\partial u_i'}{\partial t} + \underbrace{\mathcal{S}x_2\frac{\partial u_i'}{\partial x_1} + \mathcal{S}\delta_{i1}u_2'}_{\text{rapid}} + \underbrace{u_j'\frac{\partial u_i'}{\partial u_j'}}_{\text{slow}} = -\frac{\partial(p'/\rho)}{\partial x_i} + \nu\frac{\partial^2 u_i'}{\partial x_j \partial x_j} \ . \tag{1.4}$$

The terms that are proportional to the mean shear rate $\mathcal{S}$ are labeled 'rapid' and the nonlinear terms are labeled 'slow'. Taking the divergence of (1.4) while invoking the continuity relationship shown in (1.2) yields the following Poisson equation for the pressure

$$\frac{1}{\rho}\frac{\partial^2 p'}{\partial x_i \partial x_i} = -\underbrace{2\mathcal{S}\frac{\partial u_2'}{\partial x_1}}_{\text{rapid}} - \underbrace{2\frac{\partial u_i'}{\partial x_j}\frac{\partial u_j'}{\partial x_i}}_{\text{slow}} \ . \tag{1.5}$$

1.2.2 Initial Conditions

The initially isotropic velocity field was generated using a random phase algorithm with a prescribed initial energy spectrum, $E_0(k_0)$, given by

$$E_0(k_0) = C_\kappa \epsilon_0^{2/3} \kappa_0^{-5/3} \begin{cases} (k_0/\kappa_0)^2 & k_0 < \kappa_0 \\ (k_0/\kappa_0)^{-5/3} & \kappa_0 \leqslant k_0 \leqslant \kappa_\eta \\ 0 & k_0 > \kappa_\eta \end{cases} \ , \tag{1.6}$$

where k_0 is the initial wavenumber, $C_\kappa \approx 1.5$ is the Kolmogorov constant, ϵ_0 is the initial energy dissipation rate, κ_0 defines the location of the peak in the energy spectrum, and κ_η is the maximum energy-containing wavenumber, defined to be consistent with ϵ_0 as

$$\frac{\kappa_\eta}{\kappa_0} \equiv \left[\frac{2\epsilon_0^{1/3}}{3\nu C_\kappa \kappa_0^{4/3}} + \frac{11}{15}\right]^{3/4} \ . \tag{1.7}$$

The spectrum includes an energy containing range proportional to k_0^2 in order to minimize the time required for the simulation to reach the self-similar state.

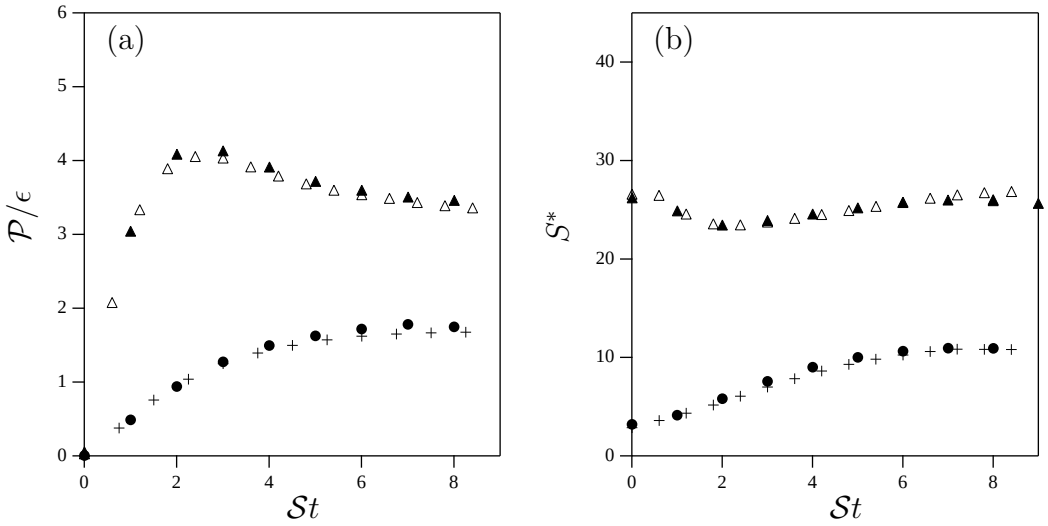

Figure 1.2: Temporal evolution of (a) $\mathcal{P}/\epsilon$ and (b) S^* for Gaussian turbulence with $S_0^* = 3$ + and 27 $\triangle$, and for an isotropic field in which the turbulence has decayed until the velocity derivative skewness, $M_3 \equiv \overline{(\partial u/\partial x)^3} / \left[\overline{(\partial u/\partial x)^2}\right]^{3/2}$, has reached the fully developed value of -0.4 with $S_0^* = 3$ $\bullet$ and 27 $\blacktriangle$. The initial Reynolds number is $(R_\lambda)_0 = 26$.

To check whether the results depend upon the Gaussian velocity field that results from the random-phase initialization, we compared them to separate runs that first let the turbulence decay without mean shear until the velocity derivative skewness, $M_3 \equiv \overline{(\partial u/\partial x)^3} / \left[\overline{(\partial u/\partial x)^2}\right]^{3/2}$, had reached the fully developed value of -0.4 (Tavoularis and Corrsin (1981)), so that the small scales were in a more natural state before applying the uniform shear. The comparison is shown in figure 1.2. As you can see, the large scales are not significantly affected by this change in the initial velocity field, and hence the Gaussian initial velocity field was used throughout this study.

1.2.3 Parameters

Homogeneous turbulent shear flow is characterized by two initial parameters: the Reynolds number defined as $R_\lambda \equiv q^2\sqrt{5/(3\nu\epsilon)}$ and the shear parameter defined as $S^* \equiv \mathcal{S}q^2/\epsilon$. The first is a measure of the ratio of the largest to the smallest turbulence length or time scales, while the second is the ratio of the largest turbulence time scale to the mean shear time scale, taken as $1/\mathcal{S}$. It is customary to define a non-dimensional time $\beta \equiv \mathcal{S}t$, which corresponds to the total strain due to the mean shear.

1.2.4 Reynolds Averaged Equations

The exact equations governing the four nonzero components of the average Reynolds stress are (Pope (2000))

$$\frac{dR_{11}}{dt} = \mathcal{P}_{11} + \Pi_{11} - \epsilon_{11} \ , \tag{1.8a}$$

$$\frac{dR_{22}}{dt} = +\Pi_{22} - \epsilon_{22} \ , \tag{1.8b}$$

$$\frac{dR_{33}}{dt} = +\Pi_{33} - \epsilon_{33} \ , \tag{1.8c}$$

$$\frac{dR_{12}}{dt} = \mathcal{P}_{12} + \Pi_{12} - \epsilon_{12} \ , \tag{1.8d}$$

where

$$R_{ij} \equiv \overline{u_i' u_j'} \ , \tag{1.9}$$

$$\mathcal{P}_{ij} \equiv -R_{ik}\frac{\partial \overline{u}_j}{\partial x_k} - R_{jk}\frac{\partial \overline{u}_i}{\partial x_k} \ , \tag{1.10}$$

$$\Pi_{ij} \equiv \overline{\frac{p'}{\rho}\left(\frac{\partial u_i'}{\partial x_j} + \frac{\partial u_j'}{\partial x_i}\right)} \ , \tag{1.11}$$

$$\epsilon_{ij} \equiv 2\nu\overline{\frac{\partial u_i'}{\partial x_k}\frac{\partial u_j'}{\partial x_k}} \ . \tag{1.12}$$

The source terms for HTSF take the form: $\mathcal{P}_{11} = -2\mathcal{S}R_{12}$ and $\mathcal{P}_{12} = -\mathcal{S}R_{22}$. Taking half of the trace of (1.8) yields the transport equation for the turbulent kinetic energy

$$\frac{dq^2/2}{dt} = \mathcal{P} - \epsilon \ , \tag{1.13}$$

where $\mathcal{P} \equiv \mathcal{P}_{11}/2$ and $\epsilon \equiv \epsilon_{ii}/2$. To analyze the self-similar regime of HTSF, it is useful to consider the anisotropic Reynolds stress tensor, $b_{ij} \equiv R_{ij}/q^2 - \delta_{ij}/3$. We expect this tensor to approach a constant in the self-similar regime. The exact governing equations for the four nonzero components of the anisotropic tensor are as follows

$$\frac{1}{\mathcal{S}}\frac{db_{11}}{dt} = 2\left(b_{11}+1/3\right)\left(b_{12}+1/S^*\right) - 2b_{12} + \tilde{\Pi}_{11} - \tilde{\epsilon}_{11} \ , \tag{1.14a}$$

$$\frac{1}{\mathcal{S}}\frac{db_{22}}{dt} = 2\left(b_{22}+1/3\right)\left(b_{12}+1/S^*\right) + \tilde{\Pi}_{22} - \tilde{\epsilon}_{22} \ , \tag{1.14b}$$

$$\frac{1}{\mathcal{S}}\frac{db_{33}}{dt} = 2\left(b_{33}+1/3\right)\left(b_{12}+1/S^*\right) + \tilde{\Pi}_{33} - \tilde{\epsilon}_{33} \ , \tag{1.14c}$$

$$\frac{1}{\mathcal{S}}\frac{db_{12}}{dt} = 2b_{12}\left(b_{12}+1/S^*\right) - \left(b_{22}+1/3\right) + \tilde{\Pi}_{12} - \tilde{\epsilon}_{12} \ , \tag{1.14d}$$

where $\tilde{\Pi}_{ij} \equiv \Pi_{ij}/\mathcal{S}q^2$ and $\tilde{\epsilon}_{ij} \equiv \epsilon_{ij}/\mathcal{S}q^2$.

1.3 Direct Numerical Simulations

1.3.1 Numerical Method

The DNS code integrates the continuity relationship (1.2) and the equation for the fluctuating velocity (1.4). The boundary condition in the x_2 direction is not periodic in the laboratory frame of reference due to the presence of the uniform shear. Figure 1.3 shows a schematic of the boundary condition in two dimensions. The dashed lines show the deforming frame of reference in which the flow is periodic.

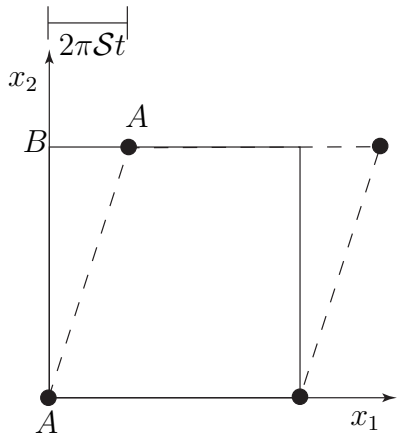

Figure 1.3: Schematic of the shear periodic boundary conditions in two dimensions. Mean shear of magnitude $\mathcal{S}$ lies in the vertical direction. Solid lines indicate orthogonal frame; dashed lines indicate deforming frame in which boundary conditions are periodic. Black dots are periodic points.

The solid lines indicate the orthogonal laboratory frame of reference. Forward and reverse spectral transforms for a generic variable ζ, expressed in terms of the orthogonal frame of reference, are shown below (Brucker et al. (2007))

$$\zeta(\mathbf{x},t) = \frac{1}{N^3}\sum_{\mathbf{k}}\hat{\zeta}(\mathbf{k},t)\exp\left[I\left(k_i x_i - \mathcal{S}tk_1x_2\right)\right] , \tag{1.15}$$

$$\hat{\zeta}(\mathbf{k},t) = \sum_{\mathbf{x}}\zeta(\mathbf{x},t)\exp\left[-I\left(k_i x_i - \mathcal{S}tk_1x_2\right)\right] , \tag{1.16}$$

where $I \equiv \sqrt{-1}$. The cross term in the exponential, $\mathcal{S}tk_1x_2$, arises due to the shear-periodic boundary condition. As a consequence of this term, it is not possible to calculate the forward and reverse transforms using a standard three-dimensional (3D) Fast Fourier Transform (FFT).

Rogallo (1981) resolved this issue by transforming (1.4) into a coordinate system that deforms with the mean flow. In this moving frame of reference, the spectral transform reduces to the conventional 3D FFT, allowing the use of a standard numerical algorithm. However, mean shear progressively distorts the mesh in physical space, leading to a growth in aliasing errors from the pseudospectral

evaluation of the nonlinear terms on the deformed mesh. To relieve this problem, Rogallo introduced a re-meshing step. As mentioned earlier, re-meshing with dealiasing leads to a sudden loss in both the turbulent kinetic energy and turbulent energy dissipation rate.

We developed an alternate algorithm that works directly with (1.15) and (1.16) in the orthogonal (laboratory) frame of reference. The challenge was to accomplish the 3D transform, with the phase shift, in $O(N^3 \ln N)$ operations, where N is the number of grid points in each direction. This was done by decomposing the three-dimensional transform into a sum of products of one- and two-dimensional transforms. To illustrate this point, we show the procedure for evaluating a forward transform.

The first step is to transform x_1, x_3 to k_1, k_3 by calling N two-dimensional real $\rightarrow$ complex FFTs yielding for an arbitrary physical-space variable $\phi(x_1, x_2, x_3)$

$$\check{\phi}(k_1, x_2, k_3) = \sum_{x_1} \sum_{x_3} \phi(x_1, x_2, x_3) \exp\left[-I\left(k_1 x_1 + k_3 x_3\right)\right] \ . \tag{1.17}$$

We then phase shift the result to accommodate the uniform mean shear

$$\tilde{\phi}(k_1, x_2, k_3) \equiv \check{\phi}(k_1, x_2, k_3) \exp\left[I\mathcal{S}t k_1 x_2\right] \tag{1.18}$$

The transform is completed by calling N^2 one-dimensional complex $\rightarrow$ complex FFTs to obtain

$$\hat{\phi}(k_1, k_2, k_3) = \sum_{x_2} \tilde{\phi}(k_1, x_2, k_3) \exp\left[-I k_2 x_2\right] \ . \tag{1.19}$$

The first calculation over planes will scale like $O(N \times N^2 \ln N)$ operations, the multiplication step $O(N^3)$, and the final transform over pencils like $O(N^2 \times N \ln N)$, yielding an overall scaling of $O(N^3 \ln N)$ operations.

We can similarly outline the reverse transform. The first step is to perform N^2 one-dimensional complex $\rightarrow$ complex pencil transformtions to obtain

$$\tilde{\phi}(k_1, x_2, k_3) = \frac{1}{N} \sum_{k_2} \hat{\phi}(k_1, k_2, k_3) \exp\left[I k_2 x_2\right] \ . \tag{1.20}$$

Next is the multiplication step

$$\check{\phi}(k_1, x_2, k_3) \equiv \tilde{\phi}(k_1, x_2, k_3) \exp\left[-I\mathcal{S}t k_1 x_2\right] \ , \tag{1.21}$$

followed by N two-dimensional complex $\rightarrow$ real, plane FFTs, yielding the desired transform

$$\phi(x_1, x_2, x_3) = \frac{1}{N^2} \sum_{k_1} \sum_{k_3} \check{\phi}(k_1, x_2, k_3) \exp\left[I\left(k_1 x_1 + k_3 x_3\right)\right] \ . \tag{1.22}$$

Again, the overall calculation scales as $O(N^3 \ln N)$ operations.

The approach is to solve the equations derived by Rogallo (1981) in Fourier space utilizing the above inverse transform to obtain the variables in physical space for the purpose of evaluating nonlinear products pseudospectrally. The algorithm has been implemented in a distributed computational environment using message passing interface (MPI). The data is decomposed into two-dimensional slabs that are distributed among the processors. Further details of the code and its validation against the Rogallo algorithm and experiments are discussed extensively in Brucker et al. (2007).

1.3.2 DNS results

DNS have been carried out at three values of the initial shear parameter, $S_0^* = 3$, 15 and 27 and two initial Reynolds numbers, $(R_\lambda)_0 = 26$ and 40. The results for the normalized turbulent kinetic energy, q^2/q_0^2, and dissipation rate, ϵ/ϵ_0 at the

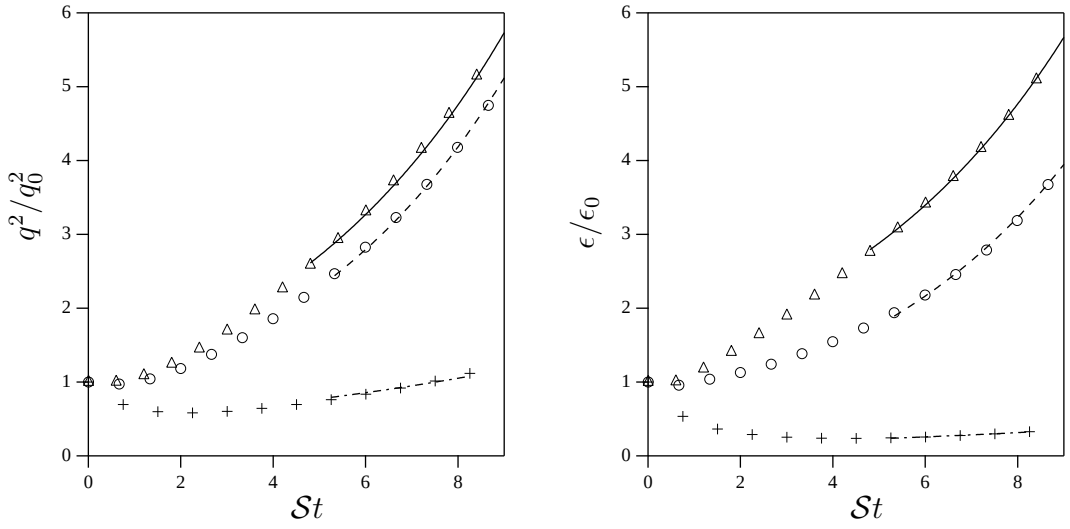

Figure 1.4: Time evolution of the normalized turbulent kinetic energy, q^2/q_0^2, and normalized dissipation rate, ϵ/ϵ_0 for + $S_0^* = 3$, ◯ $S_0^* = 15$, and △ $S_0^* = 27$. Initial Reynolds number $(R_\lambda)_0 \sim 26$. The lines represent least squares fits to (1.23) and (1.24). The fitted values of σ are reported in Table 1.1.

lower initial Reynolds number are shown in figure 1.4. The lines represent least squares fits to the expressions

$$q^2 = q_r^2 \exp\left[\sigma \mathcal{S}\left(t - t_0\right)\right] , \tag{1.23}$$

$$\epsilon = \epsilon_r \exp\left[\sigma \mathcal{S}\left(t - t_0\right)\right] , \tag{1.24}$$

where q_r^2, ϵ_r, σ and t_0 are fitting parameters. In general, we observe exponential growth for both variables, with exponents that depend sensitively on the initial shear parameter (see Table 1.1). The results are qualitatively consistent with earlier DNS (Lee et al. (1990)) and experiments (Harris et al. (1977); Tavoularis and Corrsin (1981); Rohr et al. (1988); Tavoularis and Karnik (1989); DeSouza et al. (1995)). Figure 1.5 shows the evolution of the Reynolds number and energy spectra for the lowest shear parameter. Once again, the growth in the Reynolds number is consistent with the earlier literature. The initial energy spectrum is defined in §1.2.2. With time, the spectrum evolves in both directions as expected. We do not

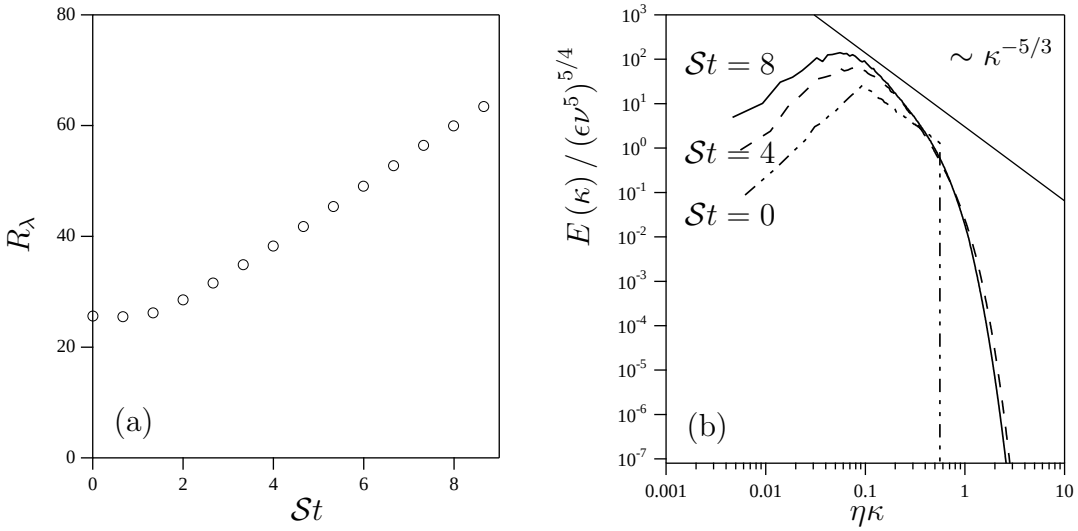

Figure 1.5: Time evolution of (a) R_λ and (b) the non-dimensional, three-dimensional energy spectrum, at the indicated values of $\mathcal{S}t$ for $S_0^* = 27$ and $(R_\lambda)_0 = 26$.

observe an inertial range in these simulations due to the modest Reynolds numbers (with the relatively strict resolution requirement we have adopted, as discussed in §1.3.3).

Figure 1.6 shows the temporal evolution of the velocity derivative skewness, M_3. The derivative skewness can be related to the turbulent energy cascade through the Karman–Howarth equation (Pope (2000)), and is therefore considered a measure of the degree to which the nonlinear terms have reached their equilibrium. We show results for initially Gaussian turbulence ($M_3(0) = 0$) subject to mean shear with $S_0^* = 3$, 15 and 27, and for isotropic turbulence that initially decayed until $M_3 \sim -0.4$ before being subjected to mean shear with $S_0^* = 3$ and 27. Following the application of mean shear, we observe M_3 decreases to a minimum and then slowly increases with time. The curves for the Gaussian turbulence, and for the isotropic turbulence that had decayed, approach each other by $\mathcal{S}t \sim 4$, suggesting little sensitivity to the initial skewness. The fact that M_3 reaches a minimum over

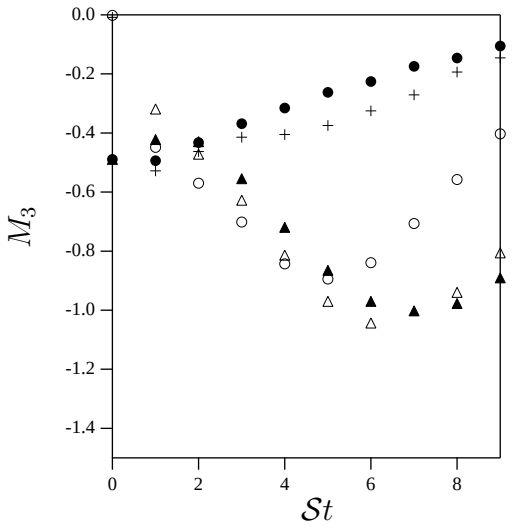

Figure 1.6: Time evolution of the skewness of the velocity derivative, M_3 for Gaussian turbulence ($M_3(0) = 0$) with three initial values of the shear parameter: $S_0^* = 3$ +, 15 ◯ and 27 △ and isotropic turbulence that initially decayed until $M_3 \sim -0.4$ and then was subjected to mean shear with $S_0^* = 3$ • and 27 ▲.

the period of our simulations supports our contention that the nonlinear terms have had adequate time to equilibrate with the flow. The result is qualitatively consistent with the experimental data compiled by Tavoularis et al. (1978), who found $-M_3$ decreased with increasing Reynolds number over the range $10 \leq R_\lambda \lesssim 200$; however, their analysis considered only the Reynolds number, whereas the results in figure 1.6 show a clear dependence on the shear parameter as well. We interpret the minimum and subsequent growth of M_3 at longer times as an indication that classical energy transfer by the nonlinear terms is growing weaker with increasing $\mathcal{S}t$. Recall that energy also is being 'transferred' from low to high wavenumbers due to the linear stretching associated with the mean shear flow (Lumley (1964); Lumley and Panofsky (1964)). Particularly at the higher values of the shear parameter, this linear transfer becomes the dominant mode of energy transfer, consistent with RDT. The results shown in figure 1.2 also support this view. The evolution of $\mathcal{P}/\epsilon$

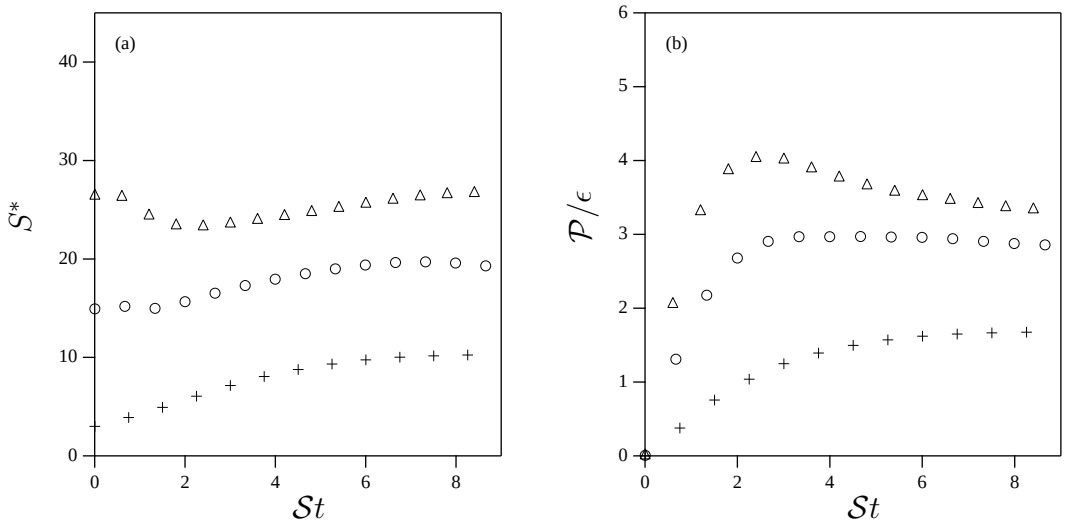

Figure 1.7: Time evolution of (a) the shear parameter S^* and (b) $\mathcal{P}/\epsilon$ (b) at + $S_0^* = 3$, ◯ $S_0^* = 15$, and △ $S_0^* = 27$. The initial Reynolds number is $(R_\lambda)_0 \sim 26$. The asymptotic values are reported in Table 1.1.

and S^* are only weakly affected by allowing the turbulence to decay initially so that M_3 approaches its equilibrium value of -0.4. Collectively, these results suggest that the dominant mechanism for energy transfer, particularly at larger values of S_0^*, is due to the linear stretching by the mean shear that is captured by RDT. This notion has been discussed by Lumley (1964) and Lumley and Panofsky (1964) for a boundary layer. The ultimate breakdown of RDT therefore involves other nonlinear effects that are discussed in §1.4.3.

To quantitatively analyze the self-similar regime of HTSF, it is useful to consider non-dimensional quantities that approach an asymptote at long times. We then can study the dependence of the asymptotes on the two parameters (Reynolds number and shear parameter). Figure 1.7 shows the time evolution of S^* and $\mathcal{P}/\epsilon$ from the DNS. As you can see, both quantities approach an asymptote that depends sensitively upon the initial value of S^*.

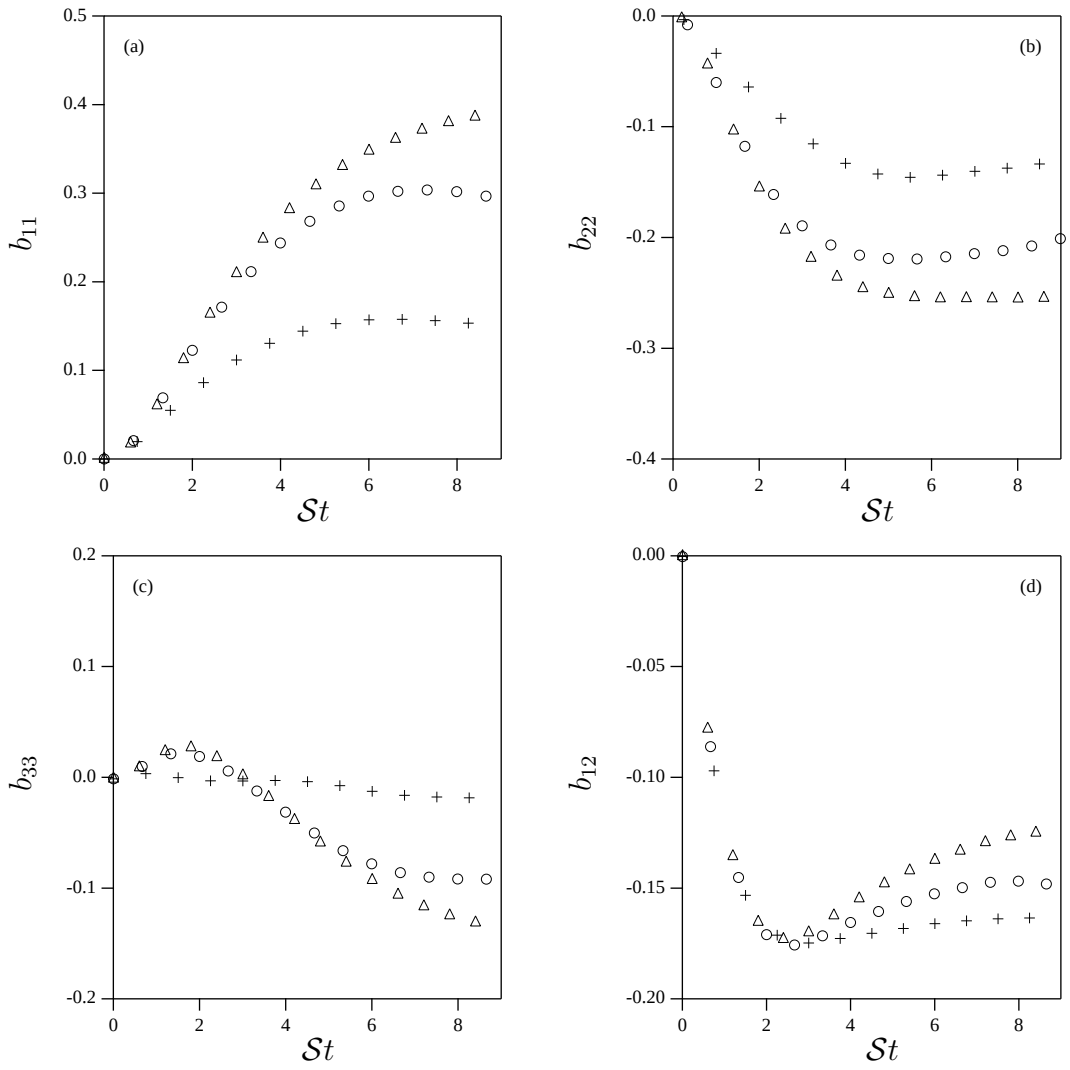

Figure 1.8: Time evolution of four components of the anisotropic Reynolds stress tensor: (a) $b_{11}(\mathcal{S}t)$; (b) $b_{22}(\mathcal{S}t)$; (c) $b_{33}(\mathcal{S}t)$; and (d) $b_{12}(\mathcal{S}t)$ at + $S_0^* = 3$, ◯ $S_0^* = 15$ and △$S_0^* = 27$. Initial Reynolds number $(R_\lambda)_0 \sim 26$.

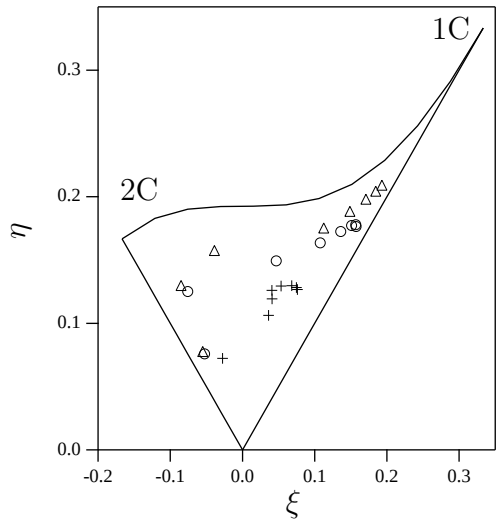

Figure 1.9: Plot of the Lumley triangle in the plane of invariants $(\tilde{\eta}, \xi)$ of the Reynolds stress anisotropy tensor. The vertices correspond to two-component (2C) and one-component (1C) turbulence, as indicated. The points correspond to $S_0^* = 3$ +, $S_0^* = 15$ ◯, and $S_0^* = 27$ △, with an initial Reynolds number $(R_\lambda)_0 \sim 26$. Notice the points appear to approach a constant fixed point that depends on the initial shear parameter.

By definition we can write

$$b_{12} = \frac{\mathcal{P}/\epsilon}{S^*} \ . \tag{1.25}$$

As $\mathcal{P}/\epsilon$ and S^* approach constants at long times, (1.25) implies b_{12} will do the same. Figure 1.8 shows the four nonzero components of the anisotropic Reynolds stress tensor. Notice that each component approaches a constant at long times that depends on S_0^*. We can analyze the anisotropy of the turbulence by considering the invariants of the anisotropy tensor, b_{ij}. The first invariant (the trace) is zero by definition. The second and third invariants are respectively: $II \equiv b_{ij}b_{ji}$ and $III \equiv b_{ij}b_{jk}b_{ki}$. If we then define $3\tilde{\eta}^2 = -2II$ and $2\xi^3 = III$, we can construct the evolution of the turbulence on the so-called 'Lumley triangle.' Figure 1.9 shows the evolution of the turbulence at the three values of the initial shear parameter. The vertices labeled 2C and 1C indicated two-component and one-component tur-

bulence respectively. Initially the curves begin at (0,0), corresponding to isotropic turbulence. The curves approach the 2C vertex at early times, but eventually come to a steady value (fixed point) near the 1C vertex, to a degree that increases with increasing initial shear parameter. Note that inviscid RDT predicts that the turbulence approaches the 1C vertex in the limit $\mathcal{S}t \to \infty$ (Pope (2000)).

We further analyze the asymptotic behaviour of b_{ij} by seeking a steady state solution to (1.14). From the DNS we compute $\tilde{\Pi}_{ij}$ and $\tilde{\epsilon}_{ij}$ and solve (1.14) for b_{ij}, neglecting the transient term on the left hand side. A summary of all of the terms, including a comparison of the prediction of (1.14) with the DNS asymptote taken from figure 1.8, is shown in table 1.1. Overall there is very good agreement between the two, moreover (1.14) captures all of the trends with S_0^* even though the time dependent term has been neglected. A similar result was obtained by Lee and Chung (1995), who solved model equations for b_{ij} and found that the steady state was sensitive to S_0^*. Note that these results are consistent with the exponential growth in q^2 and ϵ observed in Fig. 1.4. This can be seen by rewriting the turbulent kinetic energy equation (1.13) as follows

$$\frac{1}{\mathcal{S}q^2}\frac{dq^2}{dt} = 2b_{12}\left(\frac{\epsilon}{\mathcal{P}} - 1\right) = \sigma \ . \tag{1.26}$$

As b_{12} and $\mathcal{P}/\epsilon$ approach constants, we expect the same for σ, implying exponential growth of the turbulent kinetic energy at a rate that depends sensitively on S_0^*.

While the sensitivity to the shear parameter is evident in our results, we see very little sensitivity to the Reynolds number. Figure 1.10a shows a compilation of runs at $S_0^* = 3$ and 27 and $(R_\lambda)_0$ over the range 27–40. Here the results are somewhat less definitive because of the limited range of Reynolds number that we could sample (with our stringent resolution requirements). However, we note that a strong Reynolds number dependence would be inconsistent with a self-similar

Table 1.1: Asymptotic values of $\tilde{\Pi}_{ij}$, $\tilde{\epsilon}_{ij}$, b_{ij}, S^*, $\mathcal{P}/\epsilon$ and σ for each of the three values of S_0^*. The second column of b_{ij} is computed from (1.14). The first column of σ is obtained from (1.26) while the second column is determined by fitting the results shown in figure 1.4. Notice that the asymptotic value changes as a function of the initial shear parameter, and that the level of anisotropy of the flow decreases as the shear parameter increases.

i–j	$\tilde{\Pi}_{ij}$	$\tilde{\epsilon}_{ij}$	b_{ij}	b_{ij} (1.14)	S_0^*	S^*	$\mathcal{P}/\epsilon$	σ (1.26)	σ (DNS fit)
1–2	0.156	-0.014	-0.165	-0.166	3	10.3	1.6	0.12	0.10
1–1	-0.090	0.082	0.154	0.168					
2–2	0.036	0.045	-0.137	-0.140					
3–3	0.054	0.068	-0.019	-0.028					
1–2	0.086	-0.004	-0.149	-0.159	15	19.6	2.8	0.19	0.20
1–1	-0.055	0.060	0.300	0.352					
2–2	0.021	0.015	-0.210	-0.208					
3–3	0.034	0.027	-0.092	-0.146					
1–2	0.050	-0.002	-0.126	-0.139	27	26.6	3.4	0.17	0.18
1–1	-0.031	0.049	0.391	0.484					
2–2	0.012	0.008	-0.255	-0.254					
3–3	0.019	0.018	-0.144	-0.229					

regime (with constant σ) since the Reynolds number grows with increasing $\mathcal{S}t$ (see figure 1.5a). Figure 1.10b shows the same data in the form of a parameter: S^* vs R_λ. The nearly horizontal lines at the three values of S^* is consistent with the apparent weak Reynolds number dependence. We do point out that there might be a 'threshold' Reynolds number that must be exceeded to achieve self-similarity. In DNS done at very low shear parameter (not shown), we observed the turbulence decays (i.e., $\sigma < 0$). It's possible this is linked to the relatively

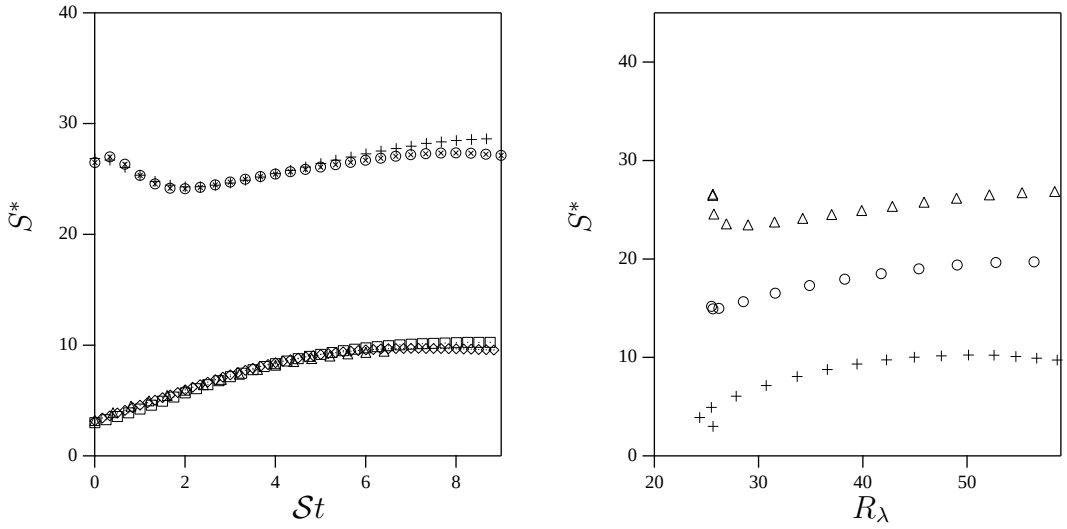

Figure 1.10: (a) Effect of initial Reynolds number on the asymptotic value of S^* for two initial values of S_0^*. $\boxdot$ $(R_\lambda)_0 = 27$, $\Diamond$ $(R_\lambda)_0 = 33$, $\triangle$ $(R_\lambda)_0 = 40$, $\otimes$ $(R_\lambda)_0 = 30$ and $+$ $(R_\lambda)_0 = 26$. (b) Parameter plot S^* versus R_λ for the three different shear rates.

small initial Reynolds number in our DNS. That is, if the initial Reynolds number is so small that the nonlinear interactions are negligible by the time the DNS has achieved appreciable strain (say $\mathcal{S}t \sim 1$), the system cannot initiate exponential growth of the kinetic energy.

1.3.3 Discussion of DNS results

The conclusions drawn in §1.3.2 are not completely consistent with some earlier DNS results. For example, Yu and Girimaji (2005) found that the asymptotes for the turbulence statistics in their flow were insensitive to the initial shear parameter. Shih et al. (2000) concluded there are three regimes: (i) at low Reynolds numbers, HTSF is sensitive to the shear parameter and the Reynolds number; (ii) at intermediate Reynolds numbers, HTSF is sensitive to the Reynolds number and

is independent of the shear parameter; and (iii) at very high Reynolds numbers, HTSF is independent of both the shear parameter and the Reynolds number. Jacobitz et al. (1997) found that the large-scale turbulence statistics are independent of Reynolds number for the higher Reynolds numbers in their study, but they identified three regimes for the shear parameter: (i) at low S_0^* the turbulence decays (i.e., $\sigma < 0$); (ii) at moderate S_0^* the turbulence grows exponentially; and (iii) for $S_0^* > 6$ the turbulence decays. Similar results were reported by Jacobitz and Sarkar (1999).

The origin of these discrepancies is not clear. However, we have discovered that an important consideration with all HTSF simulations is numerical resolution. The difficulty arises from the fact that the integral length scale L_{11} increases and the Kolmogorov length $\eta \equiv (\nu^3/\epsilon)^{1/4}$ decreases in time (see Fig. 1.5). Hence, DNS can only observe a finite window of time (currently $\mathcal{S}t \leq 10$) before loss of resolution at the large and/or small scales causes the simulation to fail. Ideally DNS should fail at the large and small scales simultaneously, as this maximizes the temporal window of the simulation. We have chosen the peak wavenumber, κ_0, and the fluid viscosity, ν, to control the initial value of the longitudinal length scale and the Kolmogorov scale respectively (see 1.6) so that the near ideal simulation is achieved. At the large scale, we monitor L_{11}/L, where $L = 2\pi$ is the box size, to make sure the large scales are well resolved. We initially considered the large scales well resolved when $L_{11}/L \leq 0.1$. However, we also track the slope dL_{11}/dt, which we expect to be positive, based on the arguments presented earlier. At the small scale we track $k_{\max}\eta$, where $k_{\max}$ is the maximum resolved wavenumber, as a measure of the resolution of the small scales. The DNS is considered resolved when $k_{\max}\eta \geq 1$. Figure 1.11 demonstrates the importance of maintaining resolution of the small scales. Notice that at the moment that the condition is violated the

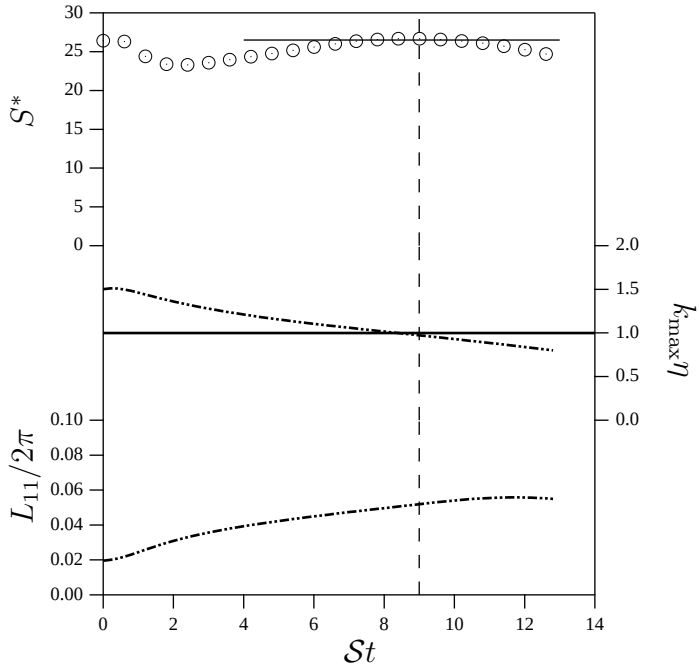

Figure 1.11: Effect of under-resolution at the small scales on the asymptotic value of S^*.

asymptotic value of S^* is lost. We attribute the deviation from the asymptote to loss of resolution of the large and/or small scales. This may explain at least some of the discrepancies in the literature. For example, the study by Shih et al. (2000) that found no dependence on the shear parameter was done at much lower resolution (grid size of 128^3) and yet had higher Reynolds numbers than the present study.

A second complication with some of the numerical studies is the use of flows that are not precisely HTSF. For example, the simulation of Schumacher (2004) that imposes a linear body force produces a flow that is similar to, but not precisely the same as HTSF. This is especially true for the large scales, that in their flow achieve a steady state with $\mathcal{P}/\epsilon = 1$, while we observe indefinite growth, corresponding to $\mathcal{P}/\epsilon > 1$. The simulation of Yu and Girimaji (2005) too is not strictly HTSF. They studied Couette flow and restricted their attention to the center of the channel

Table 1.2: Asymptotic values of b_{12} and S^* for the indicated homogeneous shear flow experiments. Notice that the asymptotic value changes as a function of the shear parameter, and that the anisotropy of the flow decreases as the asymptotic value of the shear parameter increases. The fourth column ($\mathcal{S}t$) indicates the duration of time the asymptotic level was observed.

Ref	b_{12}	S^*	$\mathcal{S}t$
Tavoularis and Karnik (1989)	-0.16	8.6	10–28
Tavoularis and Corrsin (1981)	-0.14	12.5	8–12
DeSouza et al. (1995)	-0.11	21.8	11–16

where the turbulence is nearly homogeneous. Nevertheless, there are aspects of this flow that will systematically deviate from HTSF, particularly when considering the longtime asymptote, as Couette flow will eventually approach a steady state. In our opinion, it is not straightforward to know when these slight deviations from true HTSF will begin to affect the dynamics of the large scales.

Given the conflicts in the DNS literature, we seek further evidence from experiments to support our findings. The work of Tavoularis (Tavoularis and Corrsin (1981); Tavoularis and Karnik (1989); DeSouza et al. (1995)) spans the broadest range of the shear parameter. The asymptotic values reported in these studies show a systematic dependence of the longtime asymptotes of b_{12} on the shear parameter. Table 1.2 shows a compilation of their results, along with the range of $\mathcal{S}t$ that was observed in their wind tunnel. The asymptotes are in quantitative agreement with the values found from DNS (see table 1.1), supporting our conclusion about the importance of S_0^*, and implicitly confirming the conclusion about the insensitivity to the Reynolds number, which varies strongly along the length of the wind tunnel.

1.4 Rapid Distortion Theory

As suggested by Townsend (1976); Hunt and Carruthers (1990); Lee et al. (1990); Rogers (1991) and others, when the mean deformation rate is large compared to the turbulence time-scales (*i.e.* $S^* \gg 1$), equation (1.4) can be linearized by neglecting turbulence-turbulence interactions. Solutions to the linearized equations are often referred to as Rapid Distortion Theory (RDT). The most commonly used form of the theory is based on the Euler equations, where the viscous terms also have been neglected. We shall refer to this as inviscid RDT or 'iRDT.' The justification often made for neglecting the viscous terms is that, in the absence of the nonlinear terms that are responsible for the energy cascade, the viscous terms are expected to be negligible. The resulting solution of the iRDT equations for the velocity (and all related turbulence statistics) depends solely on the total strain, $\beta \equiv \mathcal{S}t$, and is independent of the shear rate (so long as it is large enough to justify the RDT assumptions).

Our objective here is to understand the relevance of the initial Reynolds number and shear parameter, both of which depend upon the energy dissipation rate. iRDT cannot be used to consider this question. Instead, we analyze the RDT approximation to the full Navier-Stokes equation that includes the viscous terms (referred to hereafter as 'vRDT'). As the viscous terms are linear, the resulting solution remains analytic, and is only slightly more complex than iRDT.

1.4.1 Basic Formulation

The vRDT equations can be solved in Fourier space yielding (Moffat (1967); Townsend (1970); Maxey (1982); Rogers (1991))

$$\hat{\mathbf{u}}'(\mathbf{k},t) = \exp\left(-\Gamma\right)\mathbf{A}\cdot\hat{\mathbf{u}}'(\mathbf{k}_0,0)\ , \tag{1.27}$$

where $\hat{\mathbf{u}}'(\mathbf{k},t)$ is the Fourier transform of the fluctuating velocity at time t, given the initial velocity $\hat{\mathbf{u}}'(\mathbf{k}_0,0)$. Note that the mean shear causes the wavevector $\mathbf{k}$ to be a function of time. If we define the initial wavevector as $\mathbf{k}_0 \equiv (k_1,k_2,k_3)$, then the wavevector at time t is given by $\mathbf{k} \equiv (k_1, k_2 - k_1\mathcal{S}t, k_3)$. Γ and the transformation matrix $\mathbf{A}$ are defined as

$$\Gamma = \nu t\left[k_0^2 - k_1k_2\mathcal{S}t + \frac{(k_1\mathcal{S}t)^2}{3}\right]\ , \tag{1.28}$$

$$\mathbf{A}(\mathbf{k},t) = \begin{bmatrix} 1 & \frac{k_0^2}{\left(k_1^2+k_3^2\right)}\left(-\frac{k_3^2}{k_0^2}P + \frac{k_1^2}{k_0^2}Q\right) & 0 \\ 0 & \frac{k_0^2}{k^2} & 0 \\ 0 & \frac{k_1k_3}{\left(k_1^2+k_3^2\right)}\left(P+Q\right) & 1 \end{bmatrix}\ , \tag{1.29}$$

where $k_0^2 \equiv \mathbf{k}_0\cdot\mathbf{k}_0$, $k^2 \equiv \mathbf{k}\cdot\mathbf{k}$, and the functions P and Q are given by

$$P = \frac{k_0^2}{k_1\sqrt{k_1^2+k_3^2}}\left(\arctan\alpha - \arctan\tau\right)\ , \tag{1.30}$$

$$Q = \frac{\mathcal{S}t\left(k_0^2 - 2k_2^2 + k_1k_2\mathcal{S}t\right)}{k^2}\ . \tag{1.31}$$

The angles α and τ are

$$\alpha = \frac{k_2}{\sqrt{k_1^2+k_3^2}}\quad,\quad \tau = \frac{k_2 - k_1\mathcal{S}t}{\sqrt{k_1^2+k_3^2}}\ . \tag{1.32}$$

The above expressions allow us to evolve forward an arbitrary initial spectral velocity, $\hat{\mathbf{u}}'(\mathbf{k}_0,0)$. The initial velocity is assumed to be isotropic and Gaussian, with a 3D velocity spectrum defined as

$$\Phi_{ij}^0\left(\mathbf{k}_0,0\right) = \frac{E_0\left(k_0\right)}{4\pi k_0^2}\left(\delta_{ij} - \frac{k_ik_j}{k_0^2}\right)\ , \tag{1.33}$$

where $E_0(k_0)$ is the initial energy spectrum. The 3D spectrum at time t is then obtained from the following mapping

$$\Phi_{ij}(\mathbf{k},t) = e^{(-2\Gamma)} A_{ip} A_{jq} \Phi^0_{pq}(\mathbf{k_0},0) \ . \tag{1.34}$$

Arbitrary single-point statistics are determined from integrals of the spectrum, for example

$$\begin{aligned} R_{ij}(t) &= \iiint D_\nu A_{ip} A_{jq} \Phi^0_{ij}(\mathbf{k_0},0)\, d\mathbf{k} \ , & (1.35)\\ \epsilon(t) &= 2\nu \iiint k^2 D_\nu A_{ip} A_{iq} \Phi^0_{ij}(\mathbf{k_0},0)\, d\mathbf{k} \ , & (1.36)\\ \Pi^{\mathrm{r}}_{ij} &= \overline{\frac{p^{\mathrm{r}}}{\rho}\left(\frac{\partial u'_i}{\partial x_j} + \frac{\partial u'_j}{\partial x_i}\right)} \\ &= -2\mathcal{S} \iiint \left[\frac{k_i k_1}{k^2}\Phi_{j2}(\mathbf{k},t) + \frac{k_j k_1}{k^2}\Phi_{i2}(\mathbf{k},t)\right] d\mathbf{k} \ , & (1.37) \end{aligned}$$

where p^{r} is the solution to (1.5) based on the 'rapid' term only. These relationships will be used to predict the evolution of various large-scale, single-point quantities that will be compared to the DNS results.

1.4.2 Viscous RDT at short times

The initial development of the turbulence can be analyzed analytically by performing an asymptotic expansion of the vRDT solution (1.35) and (1.36) in the limit $\beta \equiv \mathcal{S}t \to 0$. We begin by defining the n^{th} moment of the initial energy spectrum as

$$\frac{I_n}{2} = \nu^n \int_0^\infty k^{2n} E_0(k_0)\, dk_0 \ . \tag{1.38}$$

The initial turbulent kinetic energy and dissipation rate are then $q_0^2 = I_0$ and $\epsilon_0 = I_1$ respectively. Using (1.35) and (1.36), we obtain the following evolution

equations for the kinetic energy and dissipation rate

$$\frac{q^2}{q_0^2}(\beta) \sim 1 - \frac{2}{S_0^*}\beta + \left(\frac{2}{15} + 2M_2\right)\beta^2 + \left(-\frac{4}{3}M_3 - \frac{16}{45}\frac{1}{S_0^*}\right)\beta^3 + \left(\frac{2}{3}M_4 + \frac{26}{45}M_2\right)\beta^4 + \cdots , \tag{1.39a}$$

$$\frac{\epsilon}{\epsilon_0}(\beta) \sim 1 - 2N_2\beta + \left(\frac{1}{3} + 2N_3\right)\beta^2 + \left(-\frac{4}{3}N_4 - \frac{46}{45}N_2\right)\beta^3 + \left(\frac{1}{105} + \frac{2}{3}N_5 + \frac{68}{45}N_3\right)\beta^4 + \cdots , \tag{1.39b}$$

where $M_n \equiv I_n/\left(q_0^2\mathcal{S}^n\right)$ and $N_n \equiv I_n/\left(\epsilon_0\mathcal{S}^{n-1}\right)$. The equations for $\mathcal{P}/\epsilon$ and S^* are

$$\begin{aligned}\frac{\mathcal{P}}{\epsilon}(\beta) \sim{}& \frac{2}{15}S_0^*\beta + \left(-\frac{1}{5} + \frac{4}{15}N_2S_0^*\right)\beta^2 \\ &+ \left(-\frac{2}{5}N_2 + \frac{8}{15}N_2^2S_0^* + \frac{2}{15}M_2S_0^* - \frac{4}{15}N_3S_0^* - \frac{2}{45}S_0^*\right)\beta^3 \\ &+ \left(\frac{2}{45} - \frac{4}{5}N_2^2 + \frac{2}{3}N_3 - \frac{2}{45}M_3S_0^* - \frac{28}{675}N_2S_0^* + \frac{4}{15}M_2N_2S_0^*\right. \\ &\left.+ \frac{16}{15}N_2^3S_0^* - \frac{16}{15}N_2N_3S_0^* + \frac{8}{45}N_4S_0^*\right)\beta^4 + \cdots ,\end{aligned} \tag{1.40a}$$

$$\begin{aligned}S^*(\beta) \sim{}& S_0^* + \left(-2 + 2N_2S_0^*\right)\beta \\ &+ \left(-4N_2 - \frac{1}{5}S_0^* + 2M_2S_0^* + 4N_2^2S_0^* - 2N_3S_0^*\right)\beta^2 \\ &+ \left(\frac{14}{45} - 8N_2^2 + 4N_3 - \frac{4}{3}M_3S_0^* - \frac{2}{45}N_2S_0^* + 8N_2^3S_0^* - 8N_2N_3S_0^* + \frac{4}{3}N_4S_0^*\right)\beta^3 \\ &+ \left(-\frac{4}{45}N_2 - 16N_2^3 + 16N_2N_3 - \frac{8}{3}N_4 + \frac{4}{45}M_2S_0^* + \frac{2}{3}M_4S_0^* - \frac{8}{3}M_3N_2S_0^*\right. \\ &+ \frac{28}{45}N_2^2S_0^* + 8M_2N_2^2S_0^* + 16N_2^4S_0^* - \frac{4}{9}N_3S_0^* - 4M_2N_3S_0^* \\ &\left.- 24N_2^2N_3S_0^* + 4N_3^2S_0^* + \frac{16}{3}N_2N_4S_0^* - \frac{2}{3}N_5S_0^* + \frac{2}{35}S_0^*\right)\beta^4 + \cdots .\end{aligned} \tag{1.40b}$$

The expansions reveal an explicit dependence of all turbulence statistics on S_0^* and an implicit dependence on the shape of the initial energy spectrum (and hence R_λ) through the integrals I_n. Figure 1.12 shows a comparison between the DNS and vRDT solutions for $\mathcal{P}/\epsilon$. The expansion captures the early time development

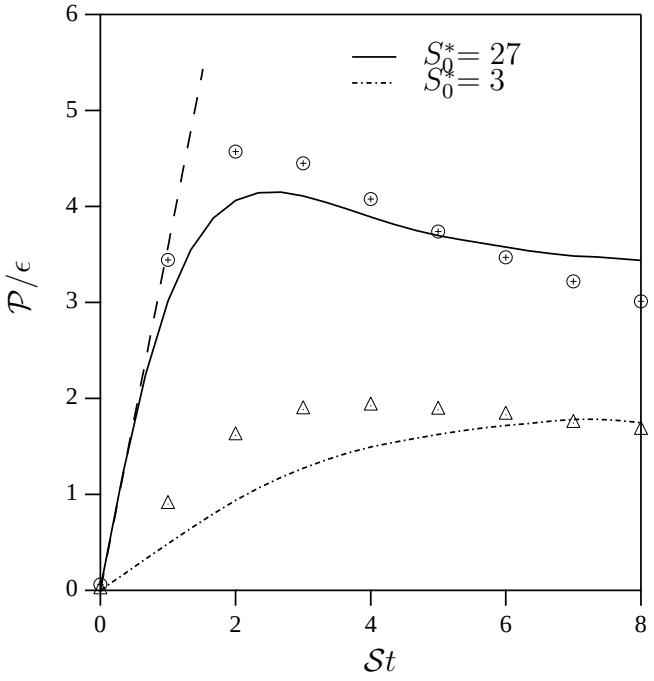

Figure 1.12: Comparison of the time evolution $\mathcal{P}/\epsilon$ from vRDT (*markers*) and DNS (*lines*) for the indicated initial values of S_0^* and $(R_\lambda)_0 \sim 26$. The dashed lines shows the expansion given by equation 1.40a

well ($\mathcal{S}t \lesssim 2$), particularly at the higher value initial shear parameter, which is consistent with the underlying assumptions of the theory.

We also can derive analytical expressions for the anisotropic Reynolds stress tensor

$$\frac{R_{11}}{q_0^2}(\beta) \sim \frac{1}{3} - \frac{2}{3}\frac{1}{S_0^*}\beta + \left(\frac{2}{21} + \frac{2}{3}M_2\right)\beta^2 + \left(-\frac{4}{9}M_3 - \frac{68}{315}\frac{1}{S_0^*}\right)\beta^3 + \left(-\frac{1}{1485} + \frac{2}{9}M_4 + \frac{88}{315}M_2\right)\beta^4 + \cdots , \tag{1.41a}$$

$$\frac{R_{22}}{q_0^2}(\beta) \sim \frac{1}{3} - \frac{2}{3}\frac{1}{S_0^*}\beta + \left(-\frac{4}{105} + \frac{2}{3}M_2\right)\beta^2 + \left(-\frac{4}{9}M_3 + \frac{44}{315}\frac{1}{S_0^*}\right)\beta^3 + \left(\frac{3}{385} + \frac{2}{9}M_4\beta^4 + \frac{52}{315}M_2\right)\beta^4 + \cdots , \tag{1.41b}$$

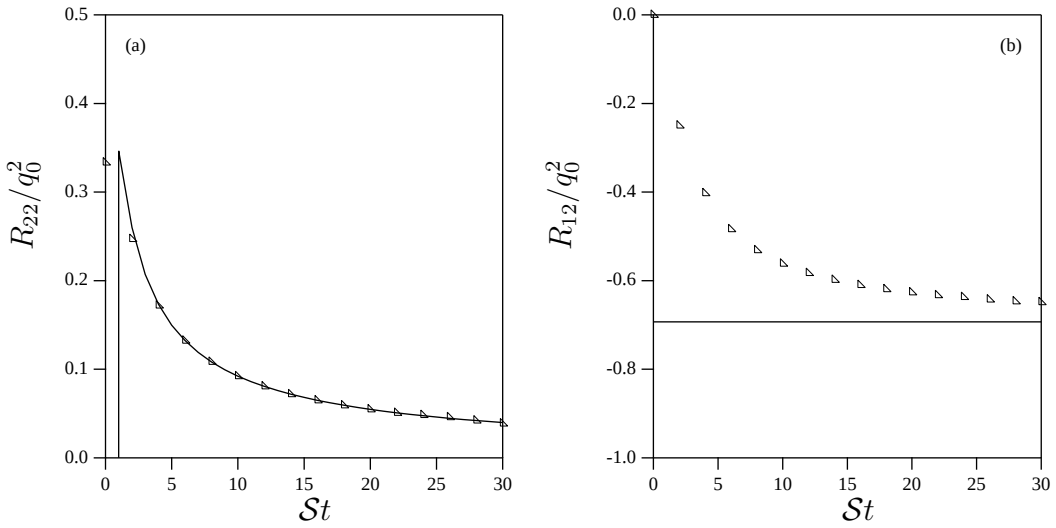

Figure 1.13: Test of the numerical scheme for evaluating the integrals at long times. (a) Comparison of numerical evaluation of *inviscid* RDT equations (markers) for R_{22} with the asymptotic prediction (lines) $\ln(4\beta)/(4\beta)$ of Rogers (1991). (b) Comparison of R_{12} with the asymptotic prediction of $-\ln(2)$ also by Rogers (1991).

$$\frac{R_{33}}{q_0^2}(\beta) \sim \frac{1}{3} - \frac{2}{3}\frac{1}{S_0^*}\beta + \left(\frac{8}{105} - \frac{2}{3}M_2\right)\beta^2 + \left(-\frac{4}{9}M_3 - \frac{88}{315}\frac{1}{S_0^*}\right)\beta^3 + \left(-\frac{74}{10395} + \frac{2}{9}M_4\beta^4 + \frac{146}{315}M_2\right)\beta^4 + \cdots , \tag{1.41c}$$

$$\frac{R_{12}}{q_0^2}(\beta) \sim \frac{2}{15}\beta - \frac{1}{5}\frac{1}{S_0^*}\beta^2 + \frac{2}{15}M_2\beta^3 - \left(\frac{2}{45}M_3 + \frac{1}{45}\frac{1}{S_0^*}\right)\beta^4 - \left(\frac{188}{135135} - \frac{2}{45}M_2\right)\beta^5 + \cdots . \tag{1.41d}$$

Notice that setting $M_n = 0$ and $S_0^* = \infty$ the above equations reduce to the inviscid expansions derived by Rogers (1991).

1.4.3 Viscous RDT at long times

It is not possible to derive an analytical solution to the vRDT equations that is valid for all time. Instead we must numerically evaluate the integrals shown in

(1.35)–(1.37). The integrals are most easily computed in spherical coordinates, with the axis oriented such that $k_1 = k\cos\theta$, $k_2 = k\sin\theta\sin\phi$, $k_3 = k\sin\theta\cos\phi$ and $d\mathbf{k} = k^2\sin\theta dk d\theta d\phi$. To improve the accuracy of the numerical integration, it is convenient to replace the initial energy spectrum with an exponential function of the following form

$$E_0(k_0) = c_1 k_0^2 \exp\left(-c_2 k_0^2\right) \ , \tag{1.42}$$

where c_1 and c_2 are adjustable parameters. Using this form of the spectrum, it is possible to analytically evaluate the semi-infinite integrals over the wavenumber k (Thacker et al. (1999)). Numerical integration is then only required over the angles θ and ϕ. The numerical integrals were performed using a two-dimensional Simpson's rule (Press et al. (1999)). The angular grid was refined until convergence was achieved. To test the accuracy of our numerical scheme, we show in figure 1.13 a comparison between the asymptote for $R_{22}(\beta)/q_0^2$ and $R_{12}(\beta)/q_0^2$ in the limit $\beta \to \infty$ for the inviscid case (i.e., $\nu = 0$) that was derived by Rogers (1991) with the numerical results (symbols). The good agreement confirms the numerical procedure.

Figure 1.14 shows the evolution of S^* and $\mathcal{P}/\epsilon$ predicted by vRDT for $0 \leq \mathcal{S}t \leq 80$. We see that vRDT predicts indefinite growth of S^*, but that $\mathcal{P}/\epsilon < 1$ at long times and hence the eventual decay of the turbulence (i.e., $\sigma < 0$ for $\beta \to \infty$). It also predicts $b_{12} \to 0$ at long times (see figure 1.15) making the production term in the turbulent kinetic energy balance equation approach zero. These long-time predictions are inconsistent with most DNS and virtually all of the experiments. Interestingly, the predicted growth of S^* with time superficially strengthens the assumptions of the theory, making the cause for its breakdown at long times unclear.

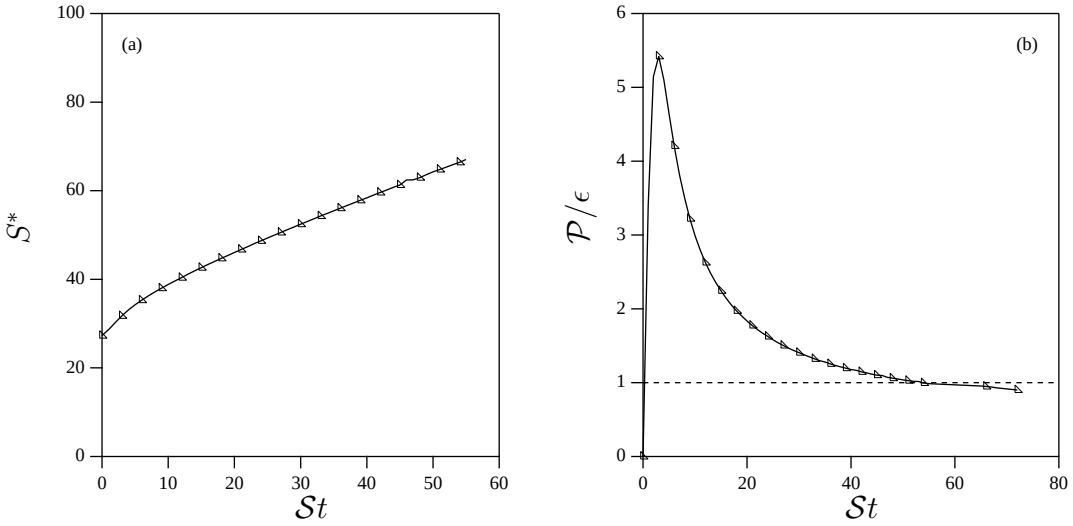

Figure 1.14: Time evolution S^* and $\mathcal{P}/\epsilon$ from vRDT for an initial value of $S_0^* = 27$ and $R_\lambda \sim 26$. Notice that $\mathcal{P}/\epsilon$ goes below one showing that the turbulence will decay at long times.

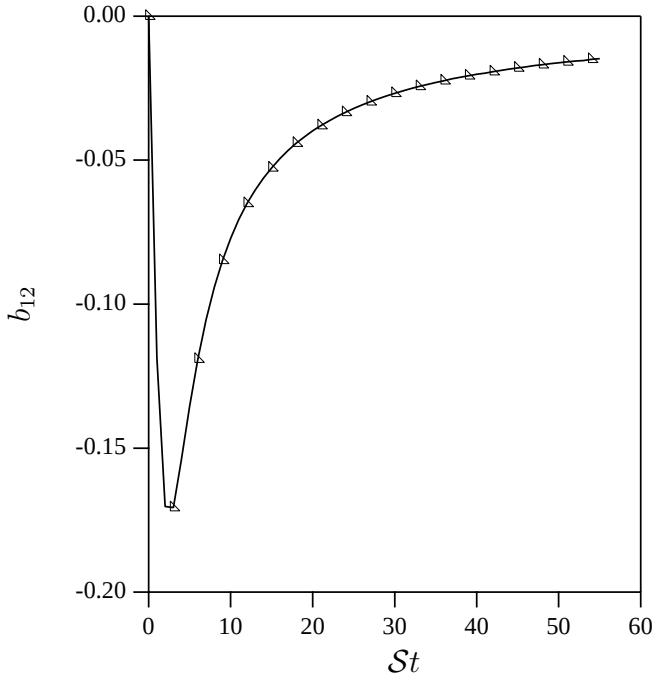

Figure 1.15: Time evolution b_{12} from vRDT for an initial value of $S_0^* = 27$ and $R_\lambda \sim 26$.

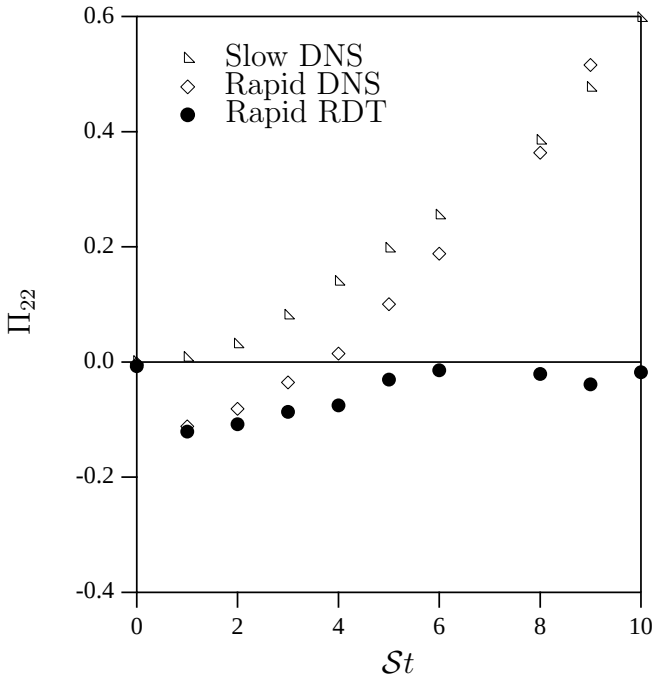

Figure 1.16: Time evolution of the rapid pressure-strain correlation Π_{22}^{r} (see (1.37) for the definition) from DNS and vRDT, and the slow pressure-strain correlation Π_{22}^{s} (see (1.44) for the definition) from DNS for $S_0^* = 27$ and $R_\lambda \sim 26$.

Clues to the cause of the failure of the theory can be found by considering the balance equation for R_{22} (1.8b). The only source for this component of the Reynolds stress is due to the pressure-strain term Π_{22}. Recalling that only the 'rapid' terms are retained in vRDT (see (1.37)) we can write

$$\Pi_{22}^{\mathrm{r}} = -2\mathcal{S} \iiint \exp\left[-2\frac{\beta\nu}{\mathcal{S}}\left(k_0^2 - \beta k_1 k_2 + \frac{\beta^2 k_1^2}{3}\right)\right] \times E_0\left(k_0\right) \frac{\left(k_2 - \beta k_1\right) k_1 \left(k_1^2 + k_3^2\right)}{4\pi \left(k_0^2 + \beta^2 k_1^2 - 2\beta k_1 k_2\right)^3} \, d\mathbf{k} \; . \tag{1.43}$$

The integrand of (1.43) goes to zero as $\beta \to \infty$ due to the unbounded (negative) growth of the exponent and the term in the denominator: $k_0^2 + \beta^2 k_1^2 - 2\beta k_1 k_2$. Consequently, vRDT predicts $R_{22} \to 0$ at long times. Figure 1.16 shows that the rapid term is initially negative (a sink) and approaches zero at long times. The resulting two-dimensional turbulence has no sources for any of the components of

the Reynolds stress, and so they all eventually decay (figure 1.15). We define the 'slow' pressure-strain correlation as

$$\Pi_{ij}^{\mathrm{s}} \equiv \overline{\frac{p^{\mathrm{s}}}{\rho}\left(\frac{\partial u_i'}{\partial x_j} + \frac{\partial u_j'}{\partial x_i}\right)}\,, \tag{1.44}$$

where p^{s} refers to the solution of the Poisson equation for the pressure (1.5) based solely on the slow term on the right hand side. In figure 1.16, we see that the rapid and slow contributions to the same component of the pressure-strain correlation behave differently. The nonlinear slow term acts as a *source* of R_{22} that eventually causes the rapid term to change sign and become a source as well. Thus, the slow pressure-strain term Π_{22}^{s} is essential for sustaining the three-dimensionality of the turbulence that enables the source terms to exceed the sinks and the turbulence to grow indefinitely (Deissler (1970)). These results suggest a simple fix of vRDT at long times may be the introduction of a nonlinear model for Π_{22}^{s}, such as the pressure-strain model of Rotta (1951).

1.5 Conclusions

In this study, we investigated the asymptotic behaviour of homogeneous turbulent shear flow using a combination of direct numerical simulations and viscous Rapid Distortion Theory. The DNS was performed using a code that allows the shear rate to be varied over a wide range (Brucker et al. (2007)). Over the window of time that the simulations retain good resolution of large and small scales, DNS predicts the large scales approach a self-similar state that is sensitive to the initial value of the shear parameter, S_0^*, and insensitive to the initial Reynolds number. The results are consistent with the body of work by Tavoularis and coworkers that showed a similar dependence of the self-similar regime on the shear parameter,

and (implicitly) no sensitivity to the Reynolds number that was growing along the length of the wind tunnel. There remain inconsistencies with earlier DNS studies that we cannot fully explain. We demonstrated the importance of grid resolution and note that some of these studies may have suffered from insufficient grid resolution (based on the size of the grid and the value of the Reynolds number in the simulation). Unfortunately, all DNS studies have this potential effect coming into play. To minimize this possibility, we implemented stringent resolution requirements that ultimately limited the range of Reynolds numbers that could be achieved ($26 \leq R_\lambda \leq 63$). The relative insensitivity to Reynolds number gives us confidence that these results are general and not an artifact of the moderate Reynolds numbers in the study.

Following earlier investigations, we analyzed the short and long term behaviour of shear flow using rapid distortion theory. The analytical solution to vRDT for short times is in excellent agreement with the DNS at high values of the shear parameter. The results show how S_0^* and R_λ enter into the solution. Analyzing this result helps explain the strong sensitivity of the large-scale turbulence statistics to the shear parameter and the weak sensitivity to the Reynolds number (the dependence on R_λ enters implicitly through its effect on the spectral moments, I_n). Numerical evaluation of the vRDT integrals for long times, however, yields results that are completely inconsistent with the DNS and experiments. In particular, the turbulent kinetic energy and viscous dissipation rate are found to decay to zero at long times. The cause has been traced to the pressure strain terms for the velocity component in the shear direction. The rapid component initially acts as a sink term, as does viscous dissipation. In the absence of the 'slow' component arising from the nonlinear convective terms, vRDT predicts this component of the Reynolds stress decays to zero. The other components of the Reynolds stress then

have no source term and so they all decay. In the DNS, the 'slow' pressure–strain term counteracts this tendency, eventually causing the rapid term to change sign. The two pressure–strain terms, acting together as sources, maintain the three-dimensionality of the turbulence, thereby allowing for the indefinite growth of all components of the Reynolds stress tensor. This suggests a simple fix of the theory, namely to include a model for the nonlinear pressure-strain term acting in the shear direction.

The high degree of sensitivity of the outcome of homogeneous turbulent shear flow to small changes in the relative size of the components of the Reynolds stress may explain why the longtime asymptotic behaviour remains so controversial.

The authors thank Z. Warhaft and K. A. Brucker for their valuable input. This work was supported by the National Science Foundation under grants PHY-0554675 and CBET-0756510. JCI was partially supported by a fellowship from the Fulbright Commission.

CHAPTER 2

EXPERIMENTAL INVESTIGATION OF THE LARGE-SCALE VELOCITY STATISTICS IN HOMOGENEOUS TURBULENT SHEAR FLOW[1]

2.1 Introduction

Homogeneous turbulent shear flow (hereafter HTSF) is among the canonical turbulent flows that is considered to be one of the 'building blocks' of turbulence. Consequently, this flow has been widely investigated in experiments (Rose (1966, 1970); Champagne et al. (1970); Harris et al. (1977); Rohr et al. (1988); Tavoularis and Corrsin (1981); Tavoularis and Karnik (1989); DeSouza et al. (1995); Garg and Warhaft (1998); Shen and Warhaft (2000)), direct numerical simulations (hereafter DNS) (Lee et al. (1990); Jacobitz et al. (1997); Jacobitz and Sarkar (1999); Shih et al. (2000); Schumacher et al. (2003); Yu and Girimaji (2005); Isaza and Collins (2009)) and theoretically (Deissler (1961); Fox (1964); Moffat (1967); Hunt and Carruthers (1990); Rogers (1991); Lee and Chung (1995)).

Two initial parameters characterize HTSF (Schumacher et al. (2003)): the Reynolds number (here we use the Reynolds number based on the Taylor microscale, $R_\lambda \equiv \lambda u'/\nu$, where λ is the Taylor microscale, u' is the rms turbulence velocity in the downstream direction and ν is the kinematic viscosity of the fluid); and the non-dimensional 'shear parameter' defined as $S^* \equiv \mathcal{S}q^2/\epsilon$, where $q^2 \equiv \overline{u_i u_i}$ is twice the turbulent kinetic energy, $\mathcal{S}$ is the uniform mean shear rate, and ϵ is the turbulent dissipation rate. Despite the attention it has received over the past 40+ years, there remain fundamental questions about the longtime behavior of the flow

[1]accepted for publication in Physics of Fluids

that have yet to be satisfactorily resolved. In particular, whether the asymptotic state of HTSF is a function of the initial value of either or both parameters remains controversial.

The DNS literature offers contradictory views. The numerical studies by Jacobitz et al. (1997); Jacobitz and Sarkar (1999) and Shih et al. (2000) of uniformly sheared, stratified flows at their lowest value of the Richardson number of 0.02 (which is close to neutral conditions) found that the asymptotic state of the flow depends sensitively on both the Reynolds number and the shear parameter. However, Shih et al. (2000) argued that the sensitivity to S_0^* (the subscript '$_0$' indicates the initial value of the quantity) vanishes at sufficiently large values of the Reynolds number ($R_\lambda \geq 80$). On the other hand, in a DNS study of Couette flow, Yu and Girimaji (2005) observed a weak sensitivity of the flow to S_0^* and a much stronger sensitivity to $(R_\lambda)_0$. Finally, the study by Lee et al. (1990) does not consider this question directly, but they show the asymptote for S^* to be sensitive to its initial value, S_0^* (see Fig. 4 of their paper).

Experiments too have offered only a partial answer to the same question. This is in part due to a lack of a systematic study in which the initial values of S^* and $R_\lambda$have been varied. The majority of the previous work was done for only one particular value of the shear parameter (Champagne et al. (1970); Harris et al. (1977)). The earlier experiments by Rose (1966, 1970) did not report the value of S^*. The more recent work of Tavoularis and Corrsin (1981), Tavoularis and Karnik (1989) and DeSouza et al. (1995) report values of S^* in the range 5.6 to 9.9 and 8.6 to 21.8 respectively. They find evidence of a self-similar regime with constant $\mathcal{P}/\epsilon$ and exponential growth of the turbulent kinetic energy, where $\mathcal{P} \equiv -\mathcal{S}\overline{uv}$ is the rate of production of turbulent kinetic energy and ϵ is the rate of dissipation of

turbulent kinetic energy. While systematic studies of the dependence of HTSF on S^* were not done, compiling results from Tavoularis and Corrsin (1981); Tavoularis and Karnik (1989) and DeSouza et al. (1995) shows a consistent trend with S^* (see Table 2.3). Rohr et al. (1988) indirectly considered the effect of the initial shear parameter on the evolution of the turbulence. They investigated the effect of varying the initial value of the integral length scale of the turbulence and separately the mean shear rate on the downstream development of the turbulence intensities. They found that turbulence intensities grew faster with increasing mean shear rate and decayed, remained constant or grew depending on the initial integral length scale. The connection of these results to the shear parameter is made clear by recognizing that it equivalently could be defined as: $S^* = \mathcal{S}L_{11}/u$, where L_{11} is the integral length scale and u is the rms of the longitudinal velocity. Qualitatively similar results were obtained by Rose (1970), although subsequent concerns have been raised about the relatively short test section of that experiment ($\mathcal{S}t \leq 3$). While the results of Rohr et al. (1988) are compelling, there has yet to be a systematic experimental investigation of the influence of S_0^* and $(R_\lambda)_0$ on the long-time behavior of the large-scale turbulence statistics.

In a recent numerical and theoretical study, Isaza and Collins (2009) investigated the sensitivity of the large scale statistics in HTSF to S_0^* and $(R_\lambda)_0$. They concluded that the asymptotic behavior of the large-scale statistics is a strong function of the initial value of shear parameter, and only weakly depends on the Reynolds number contrary to earlier DNS (see Fig. 2.1). However, they also showed that the asymptotic value predicted by DNS is very sensitive to the resolution of the simulations, limiting the maximum value of $(R_\lambda)_0$ and the maximum time the simulation can be run.

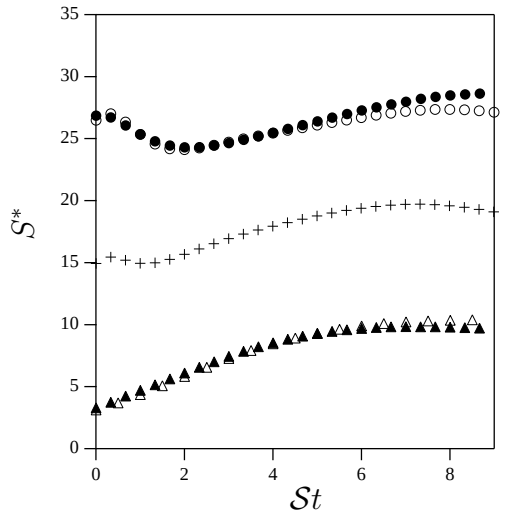

Figure 2.1: Time evolution of the shear parameter S^* from DNSIsaza and Collins (2009) for an initial value of the Reynolds number, $(R_\lambda)_0$, of 26 (open symbols), and 40 (solid symbols). The initial shear parameters are: $S_0^* = 3$ $\triangle$; $S_0^* = 15$ +; and $S_0^* = 27$ $\bigcirc$.

Given these limitations in the DNS, we decided to investigate the question of the asymptotic regime experimentally. Using an active grid (Mydlarski and Warhaft (1996)) and a passive grid (Comte-Bellot and Corrsin (1966)), we vary the initial $R_\lambda$over the range 100–250 and reach a maximum $R_\lambda$of nearly 450 at the end of the test section. We obtain two different initial values of the shear parameter by using two configurations of the shear generator (Garg and Warhaft (1998)). For the first time experimentally, we obtain the evolution of large scale quantities such as the turbulent kinetic energy, production of turbulent kinetic energy over turbulent dissipation rate, and the shear parameter as a function of the initial $R_\lambda$and initial S^*. Additionally, we address the question of the sensitivity to S_0^* and compare with the results of the DNS by Isaza and Collins (2009).

The paper is organized as follows. Sections 2.2 and 2.3 discuss the experimental methods and the characteristics of the flow respectively. Results and discussion are presented in Section 2.4 and conclusions are given in Section 2.5.

2.2 Experimental methods

2.2.1 The wind tunnel and the shear generator

Experiments are conducted in a vertical, open-circuit wind tunnel with a 40.65 $\times$ 40.65 cm^2 cross-section and that is 4.5 m long. Figure 2.2 shows a schematic drawing of the tunnel and the coordinate system used. The tunnel is described in greater detail in Sirivat and Warhaft (1983). After the contraction, the flow passes through either an active grid operating in a random mode to achieve a higher Reynolds number (detailed design and operation is described in Mydlarski and Warhaft (1996)), or directly to the shear generator (described below) that acts as a passive grid.

Mean shear is generated by placing a screen made up of eight segments of varying flow resistance after the grid. The screen is similar in design to the one used by Garg and Warhaft (1998). The segments are composed of 5 cm wide strips of fine screens and perforated metal plates of different solidities. Immediately following the shear generator, the flow passes through eight channels, 53.3 cm long and 2.54 cm wide, that straighten the flow and prevent the formation of large-scale structures in the span-wise direction. The channels are made from seven 0.16 cm thick aluminum plates. The mean shear is varied by changing the tunnel speed and by adjusting the shear generator and straighteners.

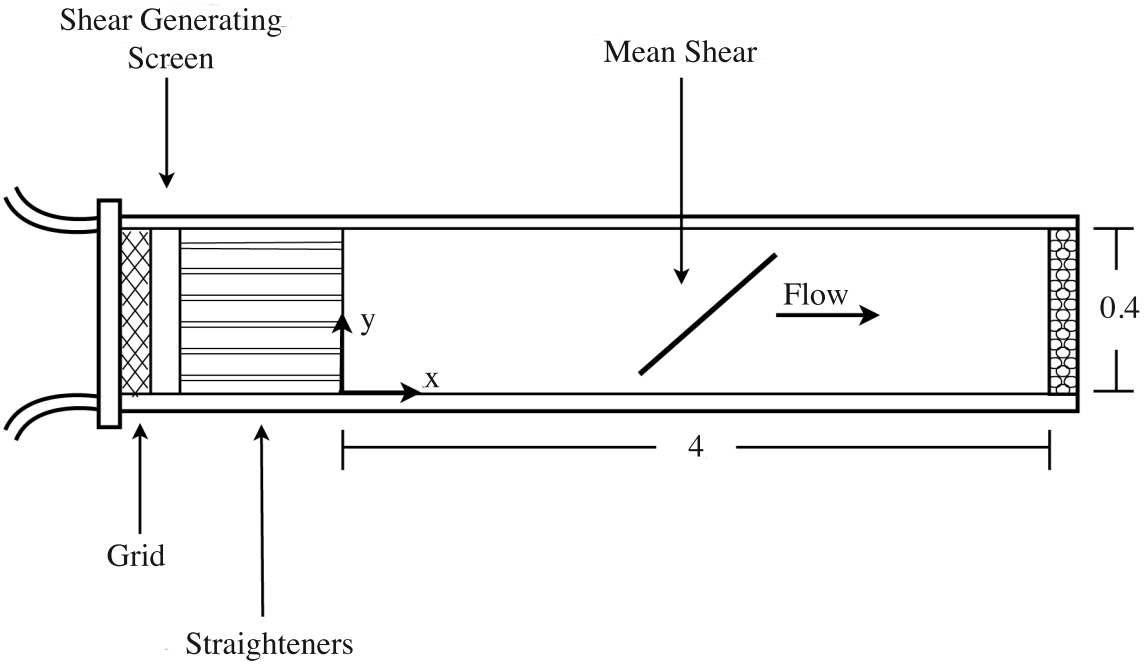

Figure 2.2: Sketch of the wind tunnel setup, with coordinate axes as indicated and all dimensions in meters. The width of the tunnel, $d = 40.65$ cm and the distance between the flow straighteners, $h = 2.54$ cm. The flow passes through a 9:1 contraction upstream of the grid. The linear mean profile is created by the screens of the shear generator followed by the flow straighteners. Downstream measurement stations are located at: $x/h = 56.2$, 76.9, 96.6 and 116.3, while the cross-stream measurement stations are at: $y/d = 0.11$, 0.23, 0.36, 0.42, 0.49, 0.54, 0.61, 0.73 and 0.86.

2.2.2 Instrumentation

The velocity is determined using a TSI X-wire probe that measures the longitudinal and one transverse component of velocity (u and v respectively) simultaneously. The tungsten wires are 3.05μm in diameter with a length-to-diameter ratio of about 200. The probes are connected to a Dantec 55M01 constant-temperature anemometer operated at an overheat ratio of 1.8. All of the signals are high-pass filtered at 0.01 Hz and low-pass filtered (varying from 800 Hz to 8000 Hz depending

on the value of R_λ) to eliminate low- and high-frequency noise. The data is digitized using a 12 bit A/D converter and typically 10^6 samples are taken for each data record. The time series is sampled at twice the low pass cutoff frequency used. The X-wire data is calibrated using the effective angle approach of Browne et al. (1989).

2.2.3 Data analysis

In this study, the Reynolds number is defined in terms of the Taylor-microscale, λ, as $R_\lambda = \lambda u'/\nu$, where

$$\lambda = \left[\overline{u^2}/\overline{(\partial u/\partial x)^2}\right]^{1/2}. \tag{2.1}$$

The longitudinal velocity derivative in the x-direction is determined using Taylor's hypothesis based on the local mean velocity, i. e., $\partial(\,)/\partial x \equiv -\overline{U}(y)^{-1}\,\partial(\,)/\partial t$. The highest turbulence intensities measured at the highest shear rate and highest Reynolds number obtained are less than 16%, making the maximum error incurred by using Taylor's hypothesis less than 4% (Heskestad (1965)).

As mentioned in the introduction, the non-dimensional 'shear parameter' is defined as $S^* \equiv \mathcal{S}q^2/\epsilon$. Since we only measure two components of the turbulent velocity (u and v), estimates for q^2 and ϵ in this non-isotropic flow are needed. The turbulent kinetic energy can be written as

$$q^2 = (1+\alpha)\left(\overline{u^2} + \overline{v^2}\right). \tag{2.2}$$

where α is defined as the ratio $\overline{w^2}/\left(\overline{u^2} + \overline{v^2}\right)$. We estimate $\alpha = 0.43$ from previous experiments that measured the three velocity components u, v and w (Tavoularis and Corrsin (1981); Rohr et al. (1988); Tavoularis and Karnik (1989); DeSouza et al. (1995)).

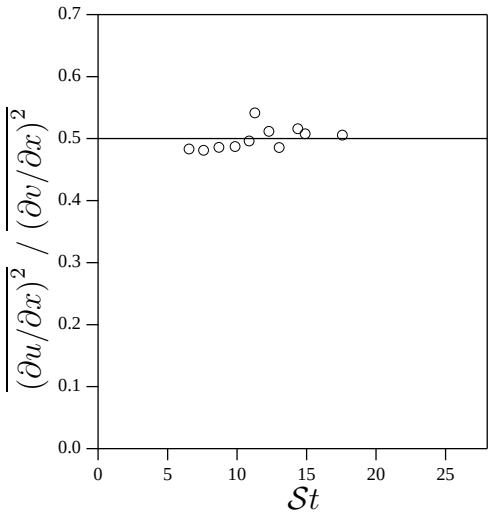

Figure 2.3: Ratio of $\overline{(\partial u/\partial x)^2}/\overline{(\partial v/\partial x)^2}$ as a function of the non-dimensional time $\mathcal{S}t$ for an initial Reynolds number of 100. The horizontal line represents the isotropic value of 0.5

The turbulent dissipation rate is estimated based on the derivative of the time series of $u(t)$ and $v(t)$. Figure 2.3 shows the ratio between $\overline{(\partial u/\partial x)^2}$ and $\overline{(\partial v/\partial x)^2}$. The ratio is close to the isotropic value of 0.5 suggesting the small-scales are nearly isotropic. The turbulent dissipation rate is therefore estimated assuming local isotropy in the velocity derivatives:

$$\epsilon = \nu \left(\overline{\frac{\partial u_i}{\partial x_k} \frac{\partial u_i}{\partial x_k}} \right) \sim \nu \left[\overline{\beta \left(\frac{\partial u}{\partial x} \right)^2 + \gamma \left(\frac{\partial v}{\partial x} \right)^2} \right]. \tag{2.3}$$

where β and γ are chosen to be 3 and 6 respectively to match the number of strain (3) and shear (6) terms in the exact expression for ϵ. The value obtained was 10–20% below the dissipation calculated by integrating the corresponding energy spectra (see Fig. 2.4)

$$\epsilon = \nu \left[\beta \int_0^\infty \kappa_1^2 E_{11}(\kappa_1)\, d\kappa_1 + \gamma \int_0^\infty \kappa_1^2 E_{22}(\kappa_1)\, d\kappa_1 \right]. \tag{2.4}$$

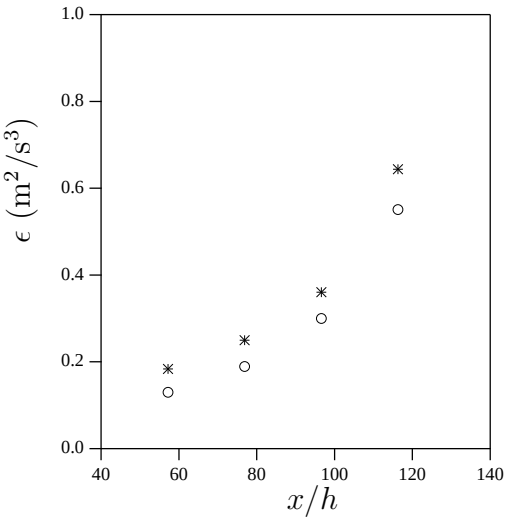

Figure 2.4: Turbulent dissipation rate ϵ calculated using Eqs. (2.3) $\bigcirc$ and (2.4) $*$ for $S^* = 16.1$ and $R_\lambda = 457.6$.

2.3 Flow characteristics

Table 2.1 shows some of the flow characteristics measured at the center of the tunnel at $x/h = 96.6$ for the active and passive grid. We also include the measurements by Tavoularis and Corrsin (1981) for reference. Although, the mean shear that we achieve is lower than theirs, turbulent quantities are of the same order of magnitude. Notice that the nondimensional values ($\mathcal{P}/\epsilon$ and S^*) from the active grid are comparable to their flow even though the values of $R_\lambda$are quite different.

Figure 2.5 shows measurements of the mean velocity profiles $\overline{U}\,(y)$ for the active and passive grid at four downstream locations: $x/h = 56.2$ +; $x/h = 76.9$ $\bigcirc$; $x/h = 96.6$ $\Diamond$; and $x/h = 116.3$ $\Box$. The linearity of the flow is excellent at all measurement locations.

Figure 2.6 shows typical cross-stream profiles of the turbulent intensities $u' = \sqrt{\overline{u^2}}$ and $v' = \sqrt{\overline{v^2}}$ normalized by the mean velocity along the center line of the

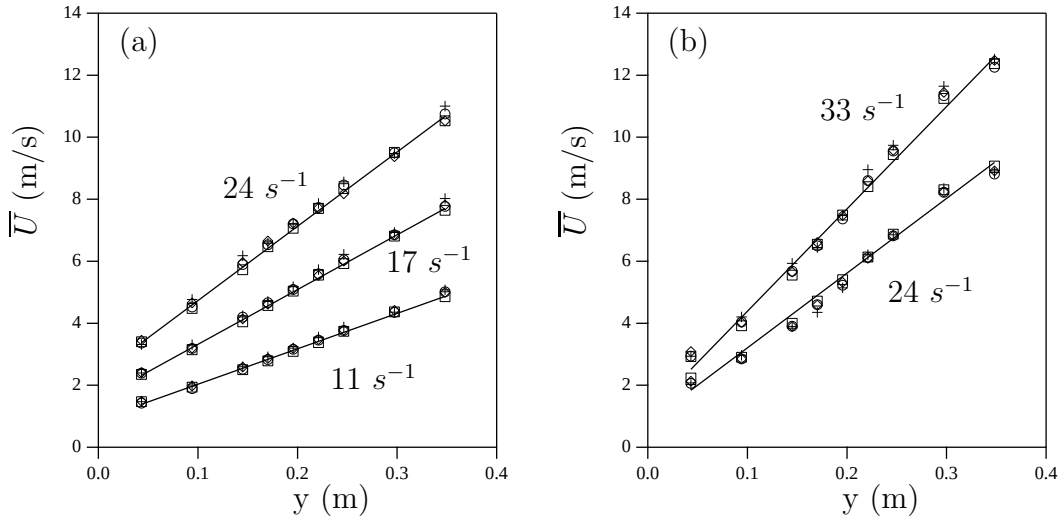

Figure 2.5: Mean Velocity for the (a) active and (b) passive grid at $x/h =$ 56.2 +; $x/h = 76.9$ ◯; $x/h = 96.6$ ◊; and $x/h = 116.3$ □.

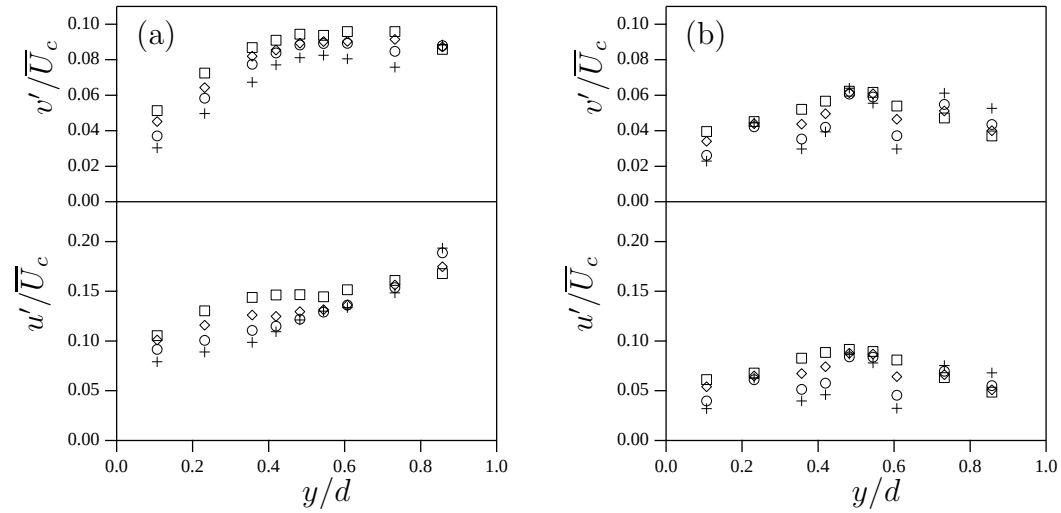

Figure 2.6: Normalized turbulence intensities $u' = \sqrt{\overline{u^2}}$ and $v' = \sqrt{\overline{v^2}}$ for the (a) active and (b) passive grid at $x/h = 56.2$ +; $x/h = 76.9$ ◯; $x/h = 96.6$ ◊; and $x/h = 116.3$ □. Both cases are for a value of the mean shear $\mathcal{S} = 24$ s^{-1}. The turbulence measurements were done in the region ($0.35 < y/d < 0.65$).

Table 2.1: Flow parameters for the active and passive grid in the self similar region of the flow. The measurements are made at the center of the tunnel and downstream distance of $x/h = 96.6$. The kinematic viscosity ν is 1.5×10^{-5} m^2/s. T&C refers to Tavoularis and Corrsin (1981). The value of ϵ reported by T&C was calculated as the imbalance between the turbulent production and the growth of turbulent kinetic energy, neglecting the other transport terms.

	Active Grid	Passive Grid	T&C
$\mathcal{S}$ (s^{-1})	24	24	46.8
$x/h =$	96.6	96.6	90
$-\rho_{uv}$	0.38	0.44	0.45
R_λ	457.6	158.9	128
ϵ (m^2/s^3)	1.81	0.99	1.9
$l = u^3/\epsilon$ (m)	0.27	0.065	0.076
η (mm)	0.21	0.25	0.204
λ (mm)	8.9	6.1	5.8
$\mathcal{P}/\epsilon$	1.97	1.51	1.81
$S^* = \mathcal{S}q^2/\epsilon$	16.1	10.11	12.63

tunnel, $\overline{U}_c$, for the active and passive grids. While the mean profiles are nearly perfectly linear there is much greater scatter in the turbulence intensities in the y-direction. However, they remain relatively constant near the center of the tunnel.

Notice that $u'/\overline{U}_c$, for the active grid (Fig. 2.6a), increases from the low-speed-side to the high-speed-side of the tunnel for the locations close to the grid and flattens off at further downstream locations. By contrast, $v'/\overline{U}_c$ remains relatively flat in the central part of the flow. A similar trend was reported by Rohr et al. (1988) (see Fig. 3 in their paper) and Tavoularis and Karnik (1989) (see Fig. 1 in their paper). In the present experiment, the systematic inhomogeneity of $u'/\overline{U}_c$ is

due to the larger longitudinal-scale introduced by the active grid. Notice that this inhomogeneity is not present in the passive grid data shown in Fig. 2.6(b).

Additionally, it can be seen that the fluctuations grow faster with downstream distance on the low-speed-side than on the high-speed-side of the tunnel. Indeed, for the furthest downstream measurement location, the turbulent intensity decreases. This variable growth rate also has been reported by Rohr et al. (1988) and may be explained in terms of the clock time of the flow as a function of y. Turbulent structures advected by a lower mean velocity have interacted longer with the mean shear at a given distance downstream compared to another y section that has a higher mean velocity. Plotting the development of the turbulence as a function of the total strain, defined here based on a local Taylor's hypothesis to be $\mathcal{S}t = \mathcal{S}x/\overline{U}(y)$, captures this unequal growth rate. Figure 2.7 shows an example of the time evolution of q^2 measured at nine stations across the tunnel (y-direction) plotted against the downstream distance (a) and total strain (b). The data collapses well when plotted against the total strain.

The cross correlations of u and v, defined as $\rho_{uv} \equiv \overline{uv}/\left(\overline{u^2}\ \overline{v^2}\right)^{1/2}$, are in agreement with previous experiments (Champagne et al. (1970); Harris et al. (1977); Tavoularis and Corrsin (1981); Tavoularis and Karnik (1989)) (see Fig. 2.8). The data show some scatter but the center core is relatively homogeneous.

Figure 2.9 shows typical one-dimensional spectra of the longitudinal and transverse velocity for the active (a) and passive (b) grid measured at the center of the tunnel and $x/h = 116.3$. The inset shows the same spectra compensated for the inertial range scaling. Notice that there is an inertial range of approximately one decade for the active grid data, but a much more limited inertial range for the passive grid due to its lower value of R_λ.

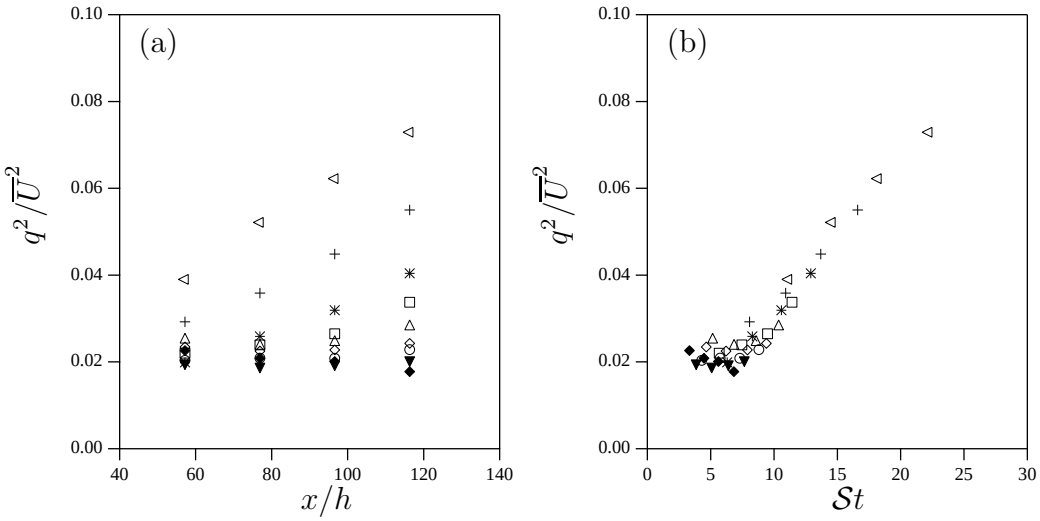

Figure 2.7: Evolution of $q^2/\overline{U}^2$ plotted against (a) the downstream distance x/h and (b) the total strain $\mathcal{S}t$. The data is for the active grid with a value of the mean shear $\mathcal{S} = 17$ s^{-1}. Each marker corresponds to the following cross-stream locations: $y/d = 0.11$ ◁; $y/d = 0.23$ +; $y/d = 0.36$ ∗; $y/d = 0.42$ □; $y/d = 0.49$ △; $y/d = 0.54$ ♢; $y/d = 0.61$ ◯; $y/d = 0.73$ ▼ and $y/d = 0.86$ ♦.

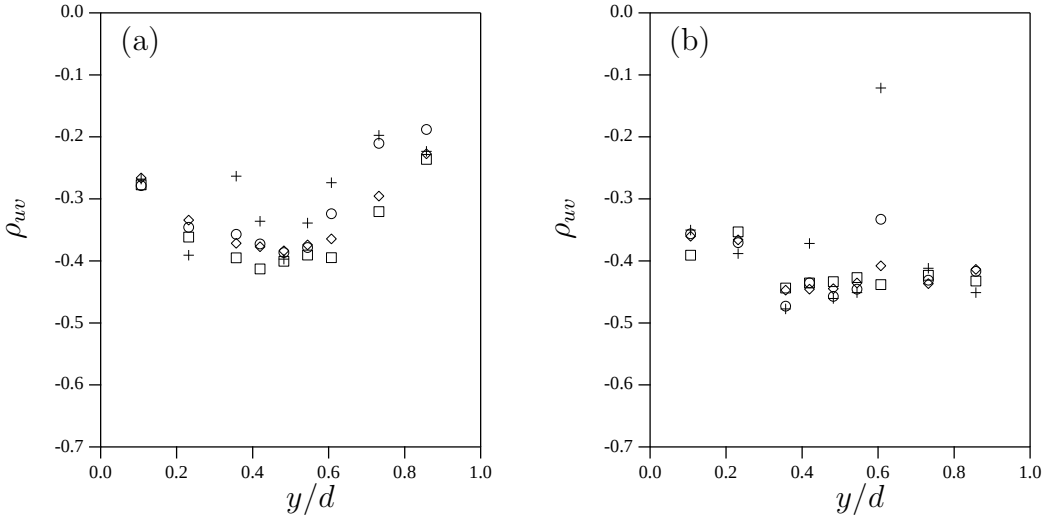

Figure 2.8: Cross correlation for the (a) active and (b) passive grid with a mean shear $\mathcal{S} = 24$ s^{-1} and locations $x/h = 56.2$ +; $x/h = 76.9$ ◯; $x/h = 96.6$ ♢; and $x/h = 116.3$ □.

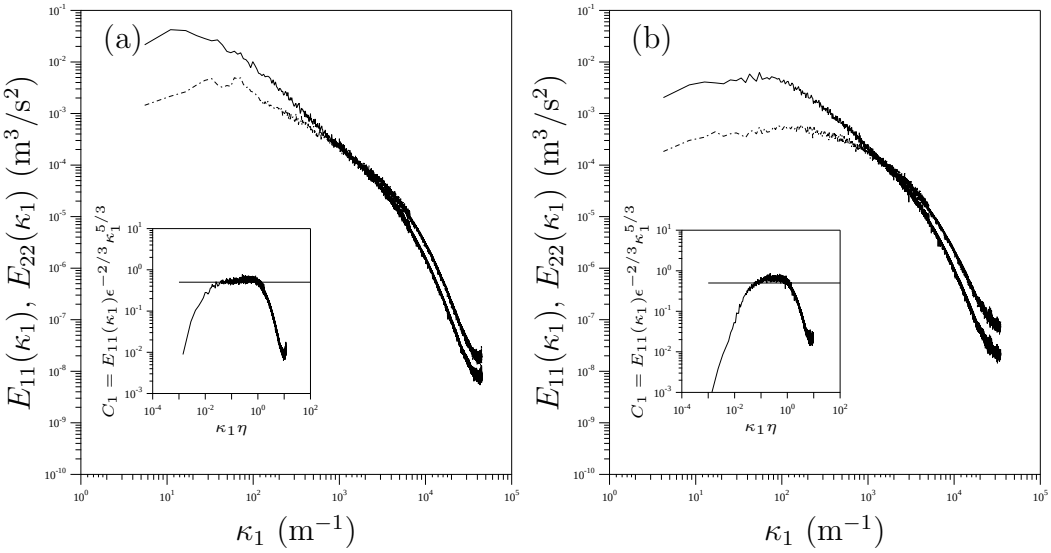

Figure 2.9: Longitudinal velocity spectrum $E_{11}(\kappa_1)$ (solid line) and transverse velocity spectrum $E_{22}(\kappa_1)$ (dashed line) measured at the center of the tunnel and $x/h = 116.3$ for the (a) active and (b) passive grids. $\kappa_1 \equiv 2\pi f/\overline{U}_c$ is the longitudinal wavenumber. R_λ=450 and 150 for the active and passive grids respectively. The inset shows the longitudinal velocity spectrum in compensated coordinates. The horizontal lines are at 0.5, the accepted value of the Kolmogorov constant C_1.Saddoughi and Veeravalli (1994)

2.4 Asymptotic Behavior

The classical analysis of HTSF (see for example Pope (2000); Tavoularis (1985)) assumes the turbulence is characterized by a single time scale (the integral time scale) and predicts that the turbulent kinetic energy at long times grows exponentially

$$q^2(t) = q_r^2 \exp(\sigma \mathcal{S} t) \tag{2.5}$$

where σ is the growth rate and q_r^2 is a reference value. The growth rate can be inferred from the turbulent kinetic energy equation (Isaza and Collins (2009))

$$\frac{1}{\mathcal{S}q^2}\frac{dq^2}{dt} = 2b_{12}\left(\frac{\epsilon}{\mathcal{P}} - 1\right) = \sigma\ , \tag{2.6}$$

where $b_{12} = \overline{uv}/q^2$ is the anisotropic Reynolds stress and $\mathcal{P} = -\mathcal{S}\overline{uv}$ is the turbulent kinetic energy production rate. Notice that an exponential growth of q^2 implies b_{12} and $\mathcal{P}/\epsilon$ approach constant values in the self-similar regime. By definition

$$S^* = -\frac{\mathcal{P}/\epsilon}{b_{12}} \; ; \tag{2.7}$$

implying, S^* too must approach an asymptotic value consistent with the evolution of b_{12} and $\mathcal{P}/\epsilon$. In the present experiment, we measure b_{12}, $\mathcal{P}/\epsilon$ and S^* for two different initial values of S^* and three initial values of R_λ. In the graphs presented below (Figs. 2.10–2.14), we have eliminated the points close to both walls, and have focused on the central core where the flow is relatively homogeneous ($0.35 \leq y/d \leq 0.65$).

Figure 2.10a shows the evolution of S^* for initial values of $R_\lambda \sim 100, 150$ and 250 and two values of S_0^*. The asymptote of S^* approaches a value that depends upon the initial value of the shear parameter, but is nearly independent of $(R_\lambda)_0$. The behavior of b_{12}, shown in Fig. 2.10b, shows some influence of the shear parameter at smaller $\mathcal{S}t$, but the asymptote is less certain due to the scatter in the data. In general, we observe much greater scatter in the velocity cross correlation $\overline{uv}$ than is observed for the other statistics, and hence all statistics involving the cross correlation show the same scatter. Both observations are consistent with what was found in the DNS,(Isaza and Collins (2009)) to within the experimental error. In the DNS study, we were able to vary the initial shear parameter by nearly one order of magnitude ($S_0^* = 3$, 15 and 27). The asymptotic values for S^*, $\mathcal{P}/\epsilon$ and b_{12} are summarized in Table 2.2. Notice that S^* is most sensitive to the initial shear parameter, followed by $\mathcal{P}/\epsilon$ and b_{12} is the least sensitive. This can be explained by considering the relationship: $\mathcal{P}/\epsilon = -b_{12}S^*$. With increasing S_0^*, the magnitude of b_{12} decreases while S^* increases causing the net dependence of $\mathcal{P}/\epsilon$ on S_0^* to be weaker than that for S^*. In the experiment, we vary S_0^* by a factor of 2 (6 and

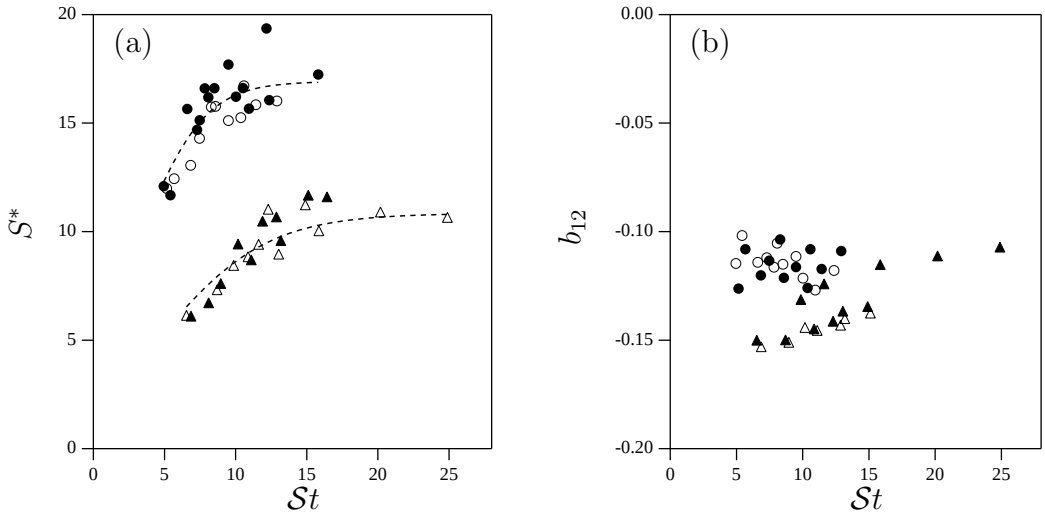

Figure 2.10: Temporal evolution of (a) S^* and (b) b_{12} for $S_0^* = 6$ and $(R_\lambda)_0$ =100 $\triangle$ and 150 $\blacktriangle$; and for $S_0^* = 12$ and $(R_\lambda)_0$ =100 $\circ$ and 250 $\bullet$. The dashed line in (a) is a least squares fit to the equation $y = Ax/(1+x)$. Based on this fit, the longtime values for S^* are 10 and 16.

Table 2.2: Asymptotes of S^*, $\mathcal{P}/\epsilon$ and b_{12} for the indicated values of S_0^* from the DNS study of Isaza and Collins (2009).

S_0^*	3	15	27
S^*	10.3	19.6	26.6
$\mathcal{P}/\epsilon$	1.6	2.8	3.4
b_{12}	-0.165	-0.159	-0.139

12) and observe a commensurately smaller change in the asymptotes of each of the variables. The experiments show a consistent trend with the DNS, namely S^* is most sensitive to S_0^* and b_{12} is the least sensitive, and the directions of all of the trends are the same.

The results shown in Figs. 2.10 and 2.11 are consistent with an exponential growth of q^2 (see (2.5) and (2.6)). Figure 2.12 shows the evolution of $q^2/\overline{U}^2$. The dashed lines indicate exponential fits of the data, although over such a limited

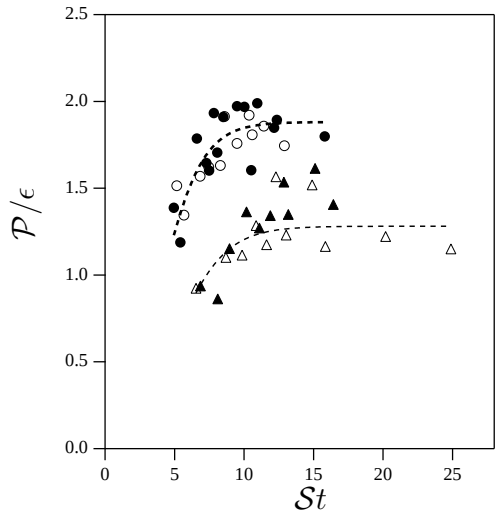

Figure 2.11: Temporal evolution of $\mathcal{P}/\epsilon$ (symbols as in Fig. 2.10). The dashed lines are least square fits to the equation $y = Ax/(1+x)$. Based on these fits, the longtime values for $\mathcal{P}/\epsilon$ are 1.28 and 1.89.

range of $\mathcal{S}t$ a linear fit is also possible. The values of σ are greater than zero in all the cases and depend upon S_0^* as implied by the behavior of $\mathcal{P}/\epsilon$ and b_{12}. The values of σ are reported in the figure.

The sensitivity to the shear parameter is evident in Figs. 2.10–2.12. However, we see far less dependence on $(R_\lambda)_0$. Figures 2.10a and 2.11 show the evolution of the shear parameter and $\mathcal{P}/\epsilon$ respectively for several initial values of the Reynolds number. Although there is some scatter, the data suggests that the flow is evolving to an asymptote that is independent of Reynolds number, implying the constant σ too is independent of the R_λ. Figure 2.12 shows the time evolution of the turbulence kinetic energy showing that σ is indeed insensitive to $(R_\lambda)_0$. We note that a strong Reynolds number dependence would be inconsistent with a self-similar regime (with constant σ) since the Reynolds number too would be growing exponentially, hence modifying the exponent. This is the first time that the influence of $R_\lambda$on statistics such as b_{12}, S^* and $\mathcal{P}/\epsilon$ has been measured experimentally.

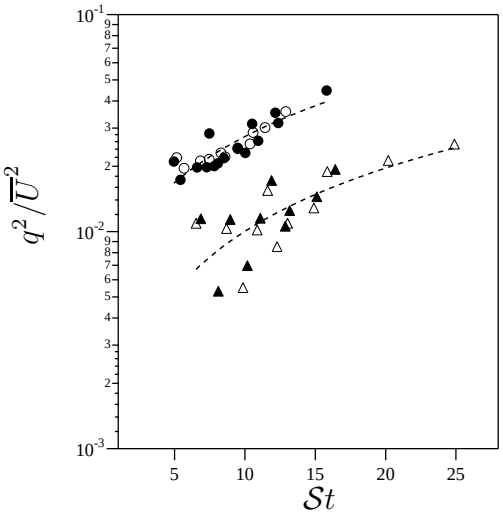

Figure 2.12: Time evolution of the turbulent kinetic energy. Symbols are the same as in Fig. 2.10. The dashed line is a least squares fit to the expression $y = A\exp\left[\sigma\mathcal{S}\left(t - t_0\right)\right]$, where A, σ and t_0 are fitting parameters. Note that $\sigma = 0.10$ for $S_0^* = 6$ and $\sigma = 0.27$ for $S_0^* = 12$.

Similar to the turbulent kinetic energy, it has been shown that the longitudinal lengthscale, $L_{11} = \int_0^\infty f_{11}(r)dr$ (where $f_{11}(r) = \overline{u(x,y,z)u(x+r,y,z)}/\overline{u^2}$) grows downstream in a HTSF. Champagne et al. (1970); Harris et al. (1977); Tavoularis and Corrsin (1981) and Rohr et al. (1988) suggested a linear growth. More recently, Tavoularis and Karnik (1989) suggested a power law claiming that its exponent is independent of the shear or any other parameter on the flow. Here we examine whether the growth rate depends upon the initial value of S_0^* and/or $(R_\lambda)_0$.

Champagne et al. (1970); Tavoularis and Corrsin (1981) and Tavoularis and Karnik (1989) measured L_{11} by integrating the corresponding autocorrelation to its first zero and using Taylor's hypothesis. Harris et al. (1977) and Rohr et al. (1988) inferred its value by extrapolating the zero-frequency intercept of the one-dimensional spectrum (Comte-Bellot and Corrsin (1971) used this approach for their isotropic experiment). We obtained L_{11} by integrating the longitudinal au-

tocorrelation to its first zero. Figure 2.13(a) shows the results for the two initial values of S_0^*. Note that the result for $S_0^* = 12$ and $(R_\lambda)_0 = 250$ is not shown because the autocorrelation functions for that case were not long enough to cross zero. Also shown in Fig. 2.13(b) are the corresponding large eddy length scales defined as $\ell \equiv \overline{u^2}^{3/2}/\epsilon$. We see that all length scales are growing with increasing $\mathcal{S}t$. Interestingly, if we compare the slopes we see that L_{11} grows more slowly at $S_0^* = 12$ (slope = 0.0017) as compared to $S_0^* = 6$ (slope = 0.0028); whereas the reverse is true for ℓ (slope = 0.0014 for $St_0^* = 6$ versus 0.012 for $St_0^* = 12$). The very different growth rates for the two length scales suggests the large scales are not in equilibrium. We show the un-normalized (dimensional) length scales in this figure because there is no natural external length scale to use and the initial length scale is difficult to estimate, particularly at the lower shear parameter. We feel plotting the dimensional data is more insightful than if we attempt to extrapolate the initial length scale, given the scatter in the data. As with the other statistics, both length scales appear to be more sensitive to S_0^* than $(R_\lambda)_0$.

2.5 Conclusions

In this study, we have investigated the dependence of the self-similar behavior of HTSF on S_0^* and $(R_\lambda)_0$. Our results show a systematic dependence of the asymptotic values of the parameters S^*, b_{12} and $\mathcal{P}/\epsilon$ upon S_0^* but not upon $(R_\lambda)_0$, in agreement with the earlier DNS study (Isaza and Collins (2009)). As noted in Section 2.1, there has been controversy in the literature over whether the large scale statistics depend upon the initial values of R_λ and S^*. Previous experiments have not investigated their influence directly; however, upon compiling the reported asymptotic values of b_{12} and S^* from the experiments of Tavoularis and Corrsin

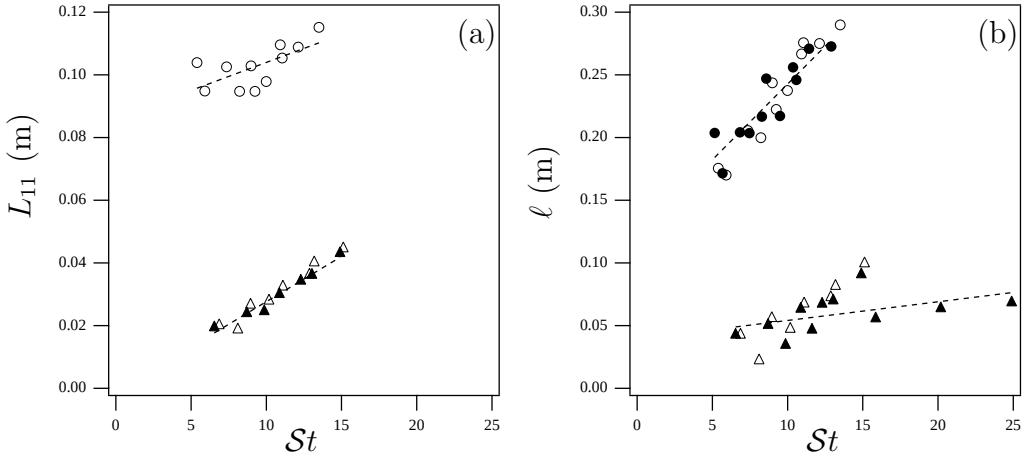

Figure 2.13: Evolution of (a) the longitudinal integral length scale L_{11} and (b) the large eddy scale $\ell \equiv \overline{u^2}^{3/2}/\epsilon$ (symbols as in Fig. 2.10). Note that the case $S_0^* = 12$ and $(R_\lambda)_0 = 250$ is not included in (a) because the autocorrelation functions for that case were not long enough to cross zero.

Table 2.3: Asymptotic values of b_{12} and S^* for various homogeneous shear flow experiments. Notice that the asymptotic value changes as a function of the shear parameter, and that the anisotropy of the flow decreases as the shear parameter increases. The fourth column ($\mathcal{S}t$) indicates the duration of time the asymptotic level was observed. T&K, T&C and DS refer to Tavoularis and Karnik (1989); Tavoularis and Corrsin (1981) and DeSouza et al. (1995) respectively.

Ref	b_{12}	S^*	$\mathcal{S}t$
T&K	-0.16	8.6	10–28
T&C	-0.14	12.5	8–12
DS	-0.11	21.8	11–16

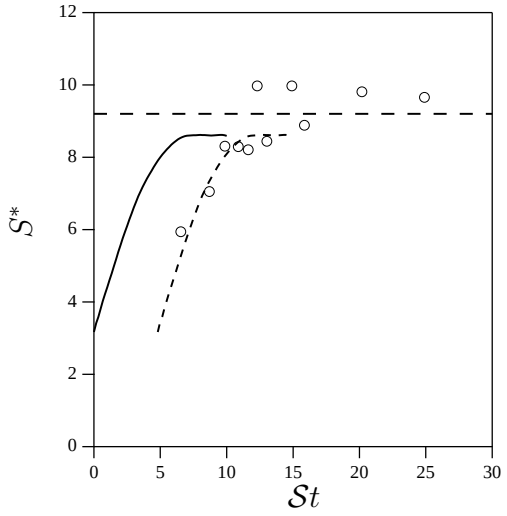

Figure 2.14: Evolution of S^* from DNS of Isaza and Collins (2009) (line) and experiments (markers). The dashed curve is the DNS results with a virtual origin shifted to match the experimental data. The horizontal dashed line represents the asymptotic value predicted by the experiments. The initial $R_\lambda$is 100 for the experiment and 26 for the DNS.

(1981); Tavoularis and Karnik (1989) and DeSouza et al. (1995) we observe a systematic dependence of the longtime asymptotes of b_{12} on the shear parameter, consistent with our findings. Table 2.3 shows a compilation of their results, along with the range of $\mathcal{S}t$ obtained in their wind tunnels. Notice also that previous experimental results (e.g., Table 2.3) implicitly confirm the conclusion about the insensitivity to the Reynolds number, which varies strongly along the length of the wind tunnel. A strong Reynolds number dependence would be inconsistent with a self-similar regime (with constant σ) since the Reynolds number too would be growing and hence modifying the exponent.

Additionally, we approximately match the conditions of one of the DNS reported in Isaza and Collins (2009) with one experiment. Figure 2.14 shows the comparison. Notice that the initial $R_\lambda$is different in the two cases due to the limitations of the DNS, but as we have shown the value of $(R_\lambda)_0$ does not influence the

long term behavior of the statistics. There is reasonable agreement in the trends between the DNS and the experiments. Both show that the flow approaches a self-similar state with a constant value of S^*, although the experimental points appear to be shifted in time by an amount $\mathcal{S}t_0 \sim 5$. To demonstrate this point, we show the DNS results with a virtual origin shifted to match the experimental data (dashed line). The experimental results extend the trend of the DNS to $\mathcal{S}t \sim 28$.

The authors are indebted to Nicole Sharp for fruitful discussions and for her assistance with the experiments. This work was supported by the National Science Foundation under grants PHY-0554675 and CBET-0756510. JCI was partially supported by a fellowship from the Fulbright Commission.

CHAPTER 3

EFFECT OF THE SHEAR PARAMETER ON VELOCITY-GRADIENT STATISTICS IN HOMOGENEOUS TURBULENT SHEAR FLOW[1]

3.1 Introduction

In recent papers (Isaza and Collins (2009); Isaza et al. (2009)), the authors considered the importance of the initial conditions on the asymptotic state of homogeneous turbulent shear flow (hereafter HTSF). Schumacher et al. (2003) identified two independent initial parameters: the Reynolds number (here defined based on the Taylor microscale, $R_\lambda \equiv \lambda u'/\nu$, where λ is the Taylor microscale, u' is the turbulence intensity in the streamwise direction and ν is the kinematic viscosity of the fluid); and the non-dimensional 'shear parameter' defined as $S^* \equiv \mathcal{S}q^2/\epsilon$, where $q^2 \equiv \overline{u_i u_i}$ is twice the turbulent kinetic energy, $\mathcal{S}$ is the uniform mean shear rate, and ϵ is the turbulent dissipation rate. The classical analysis of HTSF (e.g., Tavoularis (1985)) assumes the existence of a self-similar regime with exponential growth of the turbulent kinetic energy and dissipation rate of the form: $q^2(t) = q_r^2 \exp(\sigma \mathcal{S} t)$ and $\epsilon(t) = \epsilon_r \exp(\sigma \mathcal{S} t)$, where q_r^2 and ϵ_r are reference values of q^2 and ϵ respectively and σ is presumed to be a universal constant that is independent of the initial parameters. Furthermore, the large eddy turnover time $\epsilon(t)/q^2(t)$ is expected to approach a constant that is proportional to $\mathcal{S}^{-1}$, again with a coefficient that is taken to be independent of the initial parameters. This is equivalent to assuming S^* approaches a universal constant at long times. If turbulence were single-scaled (i.e., turbulent eddies possessing a single length and time

[1] to be submitted to the Journal of Fluid Mechanics

scale) that outcome would be guaranteed by the structure of the governing equations. However, turbulence contains a full spectrum of scales that each interact differently with the mean shear, making this outcome less certain.

This is evident in looking at the evolution of the shear parameter as a function of time. According to the classical viewpoint, the curves should approach an equilibrium value S^*_∞ as $\mathcal{S}t \to \infty$ that is independent of the initial parameters. Isaza and Collins (2009) investigated this behaviour using direct numerical simulations (DNS) by varying the initial value of the shear parameter over the range $3 < S^*_0 < 27$ (the subscript '$_0$' indicates the initial value of the quantity). Figure 3.1(a) shows the evolution of the shear parameter as a function of the non-dimensional time $\mathcal{S}t$. As you can see, the asymptote is a strong function of the initial value of the shear parameter, contradicting the classical analysis. To extend the period of time over which we could observe the behaviour of S^* and to test the results of the DNS, Isaza et al. (2009) performed the equivalent study experimentally in a wind tunnel outfitted with an active grid (Mydlarski and Warhaft (1996)). The results shown in figure 3.1(b) are qualitatively similar and confirm the relative sensitivity of the asymptote to the initial value of the shear parameter. The figure also shows that the initial value of the Reynolds number has only a weak effect on the asymptote over the range of the two studies: $26 \leq (R_\lambda)_0 \leq 250$. Note also that a strong sensitivity to the Reynolds number would be incompatible with self similarity, as R_λ increases with time and thus parameters such as σ could not be constant if they were implicit functions of R_λ.

Garg and Warhaft (1998), Shen and Warhaft (2000) and Ferchichi and Tavoularis (2000) considered in greater detail velocity derivative statistics and their dependence on the Reynolds number in HTSF at a fixed value of the shear

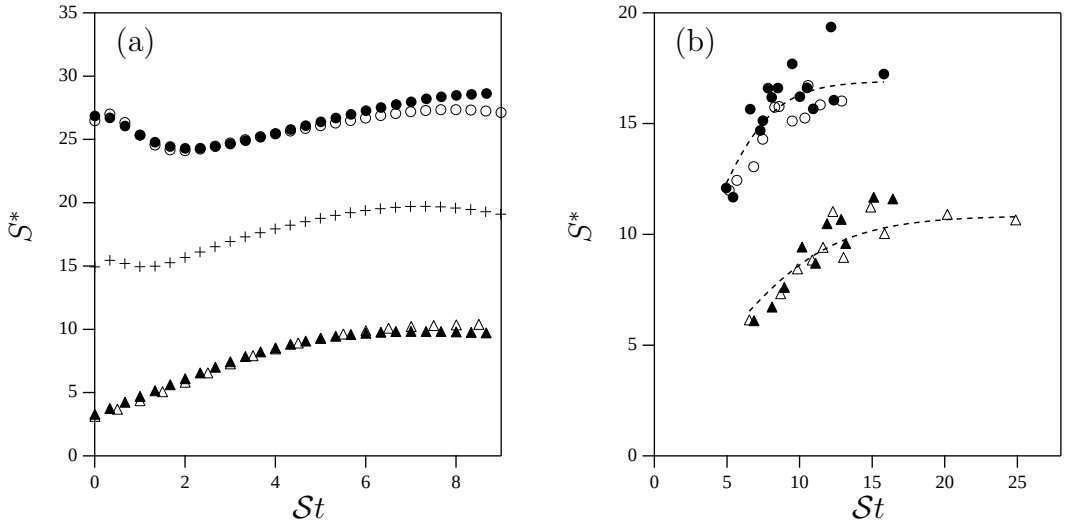

Figure 3.1: Time evolution of the shear parameter S^* from (a) the DNS by Isaza and Collins (2009) and (b) the experiments by Isaza et al. (2009). The experiment have initial values of $S_0^* = 6$ and $(R_\lambda)_0 = 100$ $\triangle$ and 150 $\blacktriangle$; and for $S_0^* = 12$ and $(R_\lambda)_0 = 100$ $\circ$, 250 $\bullet$. The initial Reynolds numbers, $(R_\lambda)_0$, in the DNS are 26 (open symbols), and $(R_\lambda)_0 = 40$ (solid symbols). $S_0^* = 3$ $\triangle$, $S_0^* = 15$ + and $S_0^* = 27$ $\bigcirc$.

parameter. These studies showed systematic variation of the velocity-gradient statistics as a function of the Reynolds number. The observed variation can be best understood based on the local Reynolds number of the flow. Generally the width of probability density functions (PDFs) of the velocity derivative statistics increases with increasing Reynolds number in a manner that is consistent with what is known about isotropic turbulence (see for example figure 5 in Ishihara et al. (2009)). What was somewhat more surprising was that the anisotropy of the small scales also increased with increasing Reynolds number, in contradiction with Kolmogorov's first hypothesis. Note that the dependence on the shear parameter was not considered in these studies.

In this paper, we investigate the effect of the shear parameter on the behaviour of small-scale velocity gradient statistics once the flow has reached its asymptotic

state. The study uses highly resolved DNS of HTSF based on a novel numerical algorithm (Brucker et al. (2007)) that avoids the shortcomings of the algorithm by Rogallo (1981) at high S^*. The code uses a pseudospectral algorithm for the Navier-Stokes equations; however, the field variables in physical space are evaluated on an orthogonal mesh in the laboratory frame instead of the deforming mesh used by the Rogallo algorithm. The resulting DNS has smaller aliasing errors, and no jumps in the kinetic energy or dissipation rate, since the remeshing step has been eliminated. In this study, we apply the new algorithm to a series of 512^3 DNS of shear flows with asymptotic values of the shear parameters in the range 3–27. We present new findings on the effect of this parameter on the rate-of-strain tensor, their probability distributions functions (hereafter PDFs) and their associated eigenvalues and eigenvectors. We also study its effects on the vorticity components, their PDFs and their orientations with respect to the principal rate-of-strain axis as well as the effect of S^* on the enstrophy and enstrophy production. The paper is organized as follows. Section 3.2 discusses the governing equations for HTSF, the equations for the small-scale turbulence, and the numerical method. Results from the DNS are presented in §3.3 followed by the study of the PDFs in the framework of viscous rapid distortion theory in §3.4. Section 3.5 presents a comparison with the experiments by Isaza et al. (2009) and conclusions are given in §3.6.

3.2 Homogeneous Turbulent Shear Flow

3.2.1 Governing Equations

We are interested in the flow of an incompressible fluid in a periodic box of length 2π in each direction. The governing equations for the fluid are

$$\frac{\partial u_i}{\partial x_i} = 0 \ , \tag{3.1}$$

$$\frac{\partial u_i}{\partial t} + u_j \frac{\partial u_i}{\partial x_j} = - \ \frac{\partial (p/\rho)}{\partial x_i} + \nu \ \frac{\partial^2 u_i}{\partial x_j \partial x_j} \ , \tag{3.2}$$

where u_i is the velocity vector, ρ is the fluid density, ν is the kinematic viscosity, and p is the pressure.

Without loss of generality, we take x_1, x_2 and x_3 to be the streamwise, shear and spanwise directions respectively. Introducing the Reynolds decomposition, $u_i = U_i + u_i'$ and $p = P + p'$, where capital letters represent mean quantities and prime letters are the fluctuating quantities. We define $U_i = (\mathcal{S} x_2, 0, 0)$, where $\mathcal{S}$ is the spatially uniform mean shear rate imposed on the flow. Invoking homogeneity and combining and simplifying the terms that involve the mean flow, the final form of the evolution equation for the fluctuating velocity is

$$\frac{\partial u_i'}{\partial t} + \mathcal{S} x_2 \frac{\partial u_i'}{\partial x_1} + \mathcal{S} \delta_{i1} u_2' + u_j' \frac{\partial u_i'}{\partial u_j'} = - \ \frac{\partial (p'/\rho)}{\partial x_i} + \nu \ \frac{\partial^2 u_i'}{\partial x_j \partial x_j} \ . \tag{3.3}$$

Taking the curl of (3.3) yields the evolution equation for the vorticity field

$$\frac{\partial \omega_i}{\partial t} = \left(-\mathcal{S} x_2 \frac{\partial \omega_i}{\partial x_1} - u_k' \frac{\omega_i}{\partial x_k} \right) + \left(\mathcal{S} \omega_2 \delta_{i1} - \mathcal{S} \frac{\partial u_i'}{\partial x_3} + \omega_k \frac{\partial u_i'}{\partial x_k} \right) + \nu \frac{\partial \omega_i}{\partial x_k \partial x_k} \tag{3.4}$$

where,

$$\omega_i = \epsilon_{ijk} \frac{\partial u_k'}{\partial x_j} \tag{3.5}$$

is the fluctuating vorticity and ϵ_{ijk} is the alternating unit tensor.

Multiplying (3.4) by ω_i and averaging yields the equation for the enstrophy ($\zeta \equiv \frac{1}{2}\overline{\omega_i\omega_i}$)

$$\frac{d\zeta}{dt} = 2\underbrace{\overline{\omega_1\omega_2}\mathcal{S}}_{\mathcal{P}_r} + \underbrace{\overline{\omega_i\omega_j s_{ij}}}_{\mathcal{P}_s} - \underbrace{\nu\overline{\frac{\partial\omega_i}{\partial x_p}\frac{\partial\omega_i}{\partial x_p}}}_{\text{viscous}} , \tag{3.6}$$

where $\mathcal{P}_r$ is the production of enstrophy associated with the mean shear (rapid term) and $\mathcal{P}_s$ is the production of enstrophy by the interaction of the vorticity with the fluctuating rate-of-strain tensor (non-linear or slow term), which is defined as

$$s_{ij} = \frac{1}{2}\left(\frac{\partial u_i'}{\partial x_j} + \frac{\partial u_j'}{\partial x_i}\right) . \tag{3.7}$$

3.2.2 Numerical Method

The DNS code integrates the continuity relationship (3.1) and the equation for the fluctuating velocity (3.3). The boundary conditions in the x_2 direction are not periodic in the laboratory frame of reference due to the presence of the uniform shear. Rogallo (1981) resolved this issue by transforming (3.3) into a coordinate system that deforms with the mean flow. In this moving frame of reference, the spectral transform reduces to the conventional 3D FFT, allowing the use of a standard numerical algorithm. However, mean shear progressively distorts the mesh in physical space, leading to a growth in aliasing errors due to the pseudospectral evaluation of the nonlinear terms on the progressively deformed mesh. To relieve this problem, Rogallo introduced a re-meshing step. As mentioned earlier, re-meshing with dealiasing leads to a sudden loss in both the turbulent kinetic energy and turbulent energy dissipation rate which limits the use of the algorithm to moderate values of the shear parameter.

We developed an alternate algorithm that works directly in the orthogonal (laboratory) frame of reference. The challenge was to accomplish the 3D trans-

form, with the phase shift, in $O(N^3 \ln N)$ operations, where N is the number of grid points in each direction. This was accomplished by decomposing the three-dimensional transform into a sum of products of one- and two-dimensional transforms. The performance and validation of this new algorithm with experiments and the Rogallo algorithm are discussed extensively in Brucker et al. (2007).

3.2.3 Initial Conditions and Resolution

To specify the initial conditions for the DNS, we first generate a velocity field using a random phase algorithm with a prescribed initial energy spectrum, $E_0(k_0)$, given by

$$E_0(k_0) = C_\kappa \epsilon_0^{2/3} \kappa_0^{-5/3} \begin{cases} (k_0/\kappa_0)^2 & k_0 < \kappa_0 \\ (k_0/\kappa_0)^{-5/3} & \kappa_0 \leqslant k_0 \leqslant \kappa_\eta \\ 0 & k_0 > \kappa_\eta \end{cases} , \tag{3.8}$$

where k_0 is the initial wavenumber, $C_\kappa \approx 1.5$ is the Kolmogorov constant, ϵ_0 is the initial energy dissipation rate, κ_0 defines the location of the peak in the energy spectrum, and κ_η is the maximum energy-containing wavenumber, defined to be consistent with ϵ_0 as

$$\frac{\kappa_\eta}{\kappa_0} \equiv \left[\frac{2\epsilon_0^{1/3}}{3\nu C_\kappa \kappa_0^{4/3}} + \frac{11}{15} \right]^{3/4} . \tag{3.9}$$

The statistics of the resulting velocity field are Gaussian. As we are interested in investigating how the non-Gaussian velocity derivative statistics are affected by shear, we allow this random field to decay *without* shear until the velocity derivative skewness, $\overline{\left(\frac{\partial u_1}{\partial x_1}\right)^3} / \left(\overline{\left(\frac{\partial u_1}{\partial x_1}\right)^2}\right)^{3/2}$, has reached its asymptotic value of -0.4 (Tavoularis and Corrsin (1981)), indicating the small scales have achieved an equilibrium state. We used this velocity field to initialize the HTSF study.

In a numerical simulation of HTSF the integral length scale $L_{11,1}$ increases and

the Kolmogorov length η decreases in time. Hence, DNS can only observe a finite window of time before loss of resolution at the large and/or small scales causes the simulation to fail. A more detailed discussion about the influence of resolution on the asymptotic state of an HTSF can be found in Isaza and Collins (2009). Ideally DNS should fail at the large and small scales simultaneously, as this maximizes the temporal window of the simulation. At the large scale, we monitor $L_{11,1}/L$, where $L = 2\pi$ is the box size, to make sure the large scales are well resolved. We initially considered the large scales well resolved when $L_{11,1}/L \leq 0.1$. However, we also track the slope $dL_{11,1}/dt$, which we expect to be positive based on experimental measurements (Tavoularis and Corrsin (1981); Rohr et al. (1988); Tavoularis and Karnik (1989); DeSouza et al. (1995); Isaza et al. (2009). At the small scale we track $k_{\max}\eta$, where $k_{\max}$ is the maximum resolved wavenumber and $\eta \equiv (\nu^3/\epsilon)^{1/4}$ is the Kolmogorov length scale, as a measure of the resolution of the small scales. The DNS is considered resolved when $k_{\max}\eta \geq 1$. Figure 3.2 shows the evolution of the Reynolds number from its initial value of 26 and the evolution of the energy spectrum for one of our high shear value simulations ($S^* = 27$). The simulations do not have a significant inertial range, despite the fact that they were performed on a 512^3 grid, due to the relatively stringent resolution conditions we have required (see Isaza and Collins (2009) for a more complete discussion).

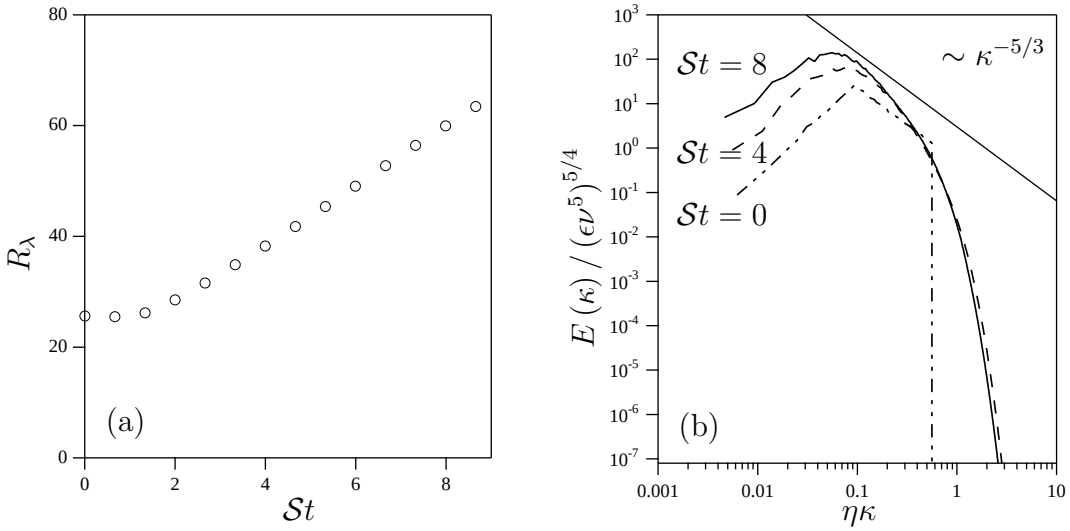

Figure 3.2: Time evolution of (a) R_λ and (b) the non-dimensional, three-dimensional energy spectrum at the indicated values of $\mathcal{S}t$ for $S_0^* = 27$ and $(R_\lambda)_0 = 26$.

3.3 Direct Numerical Simulations

3.3.1 Vorticity Statistics

Figure 3.3 shows the time evolution of the variance of the vorticity components $\overline{\omega_1^2}$, $\overline{\omega_2^2}$ and $\overline{\omega_3^2}$ normalized by the vorticity variance defined as $\omega_{\text{rms}}^2 \equiv \overline{\omega_i^2}$ for $R_\lambda = 26$ and $S_0^* = 3$ and $S_0^* = 26$. The relative magnitude of the three components is affected by the value of the shear parameter. At early times, the components of the vorticity are organized as $\omega_1 > \omega_2 > \omega_3$; however for the higher shear parameter value, ω_3 becomes the largest of three components after $\mathcal{S}t \sim 5$. The increase in ω_3 is accompanied by a decrease in ω_1, with ω_2 relatively unaffected. Recalling that ω_3 is the vorticity component aligned with the mean shear vorticity, its increase suggests that ω_3 has been enhanced by the mean vorticity.

Figure 3.4 shows the evolution of the normalized cross term $\overline{\omega_1\omega_2}$. In both

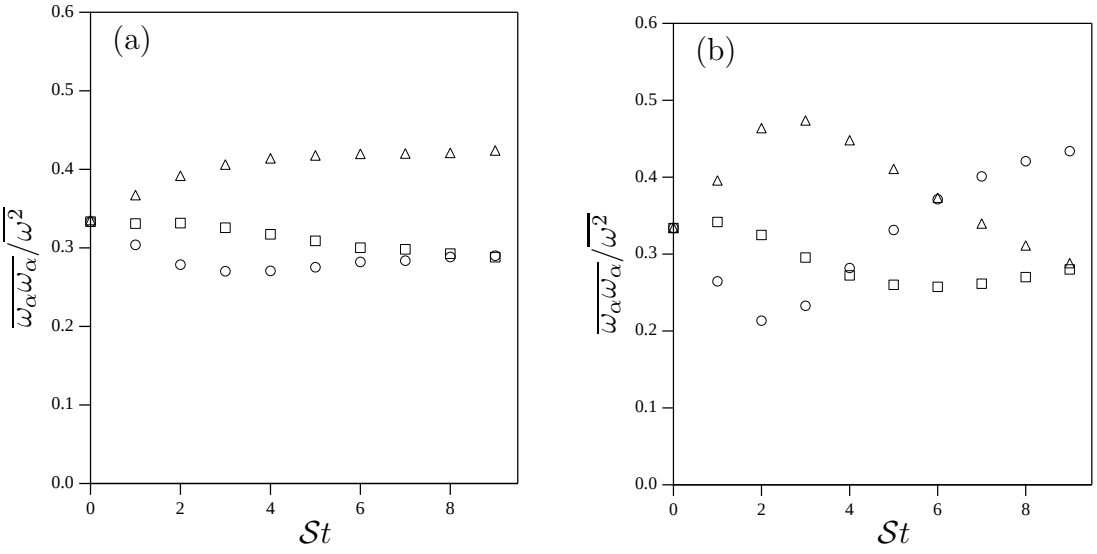

Figure 3.3: Time evolution of the vorticity components $\overline{\omega_\alpha\omega_\alpha}$ normalized by the vorticity magnitude $\overline{\omega^2}$. The markers are: $\triangle$ $\overline{\omega_1^2}/\overline{\omega^2}(\mathcal{S}t)$; $\square$ $\overline{\omega_2^2}/\overline{\omega^2}(\mathcal{S}t)$ and $\circ$ $\overline{\omega_3^2}/\overline{\omega^2}(\mathcal{S}t)$ at (a) $S_0^* = 3$ and (b) $S_0^* = 27$. Initial Reynolds number $(R_\lambda)_0 \sim 26$. No summation in the α indices.

cases ($S_0^* = 3$ and $S_0^* = 26$), it reaches a maximum around $\mathcal{S}t \sim 2$ and decreases thereafter to ~ 0.1. The fact that $\overline{\omega_1\omega_2}$ is greater than zero indicates that the fluctuating vorticity is preferentially inclined towards the streamwise direction by the mean shear. A similar results was found by Kida and Tanaka (1992, 1994) in their simulation with $S_0^* = 16$ and $(R_\lambda)_0 = 16$.

The mean shear also influences higher-order moments of the vorticity field. This is most easily observed by considering the probability density function (PDF) of the vorticity fluctuations. Figure 3.5 shows the PDF of the three components of the vorticity normalized by their standard deviations for two values of the shear parameter ($S^* = 10$ and $S^* = 27$) in the self similar region of the flow at a Reynolds number of 68 in both cases. The PDF of ω_1 is nearly perfectly symmetric, with a skewness $M_3 = \omega_1^3/\left(\overline{\omega_1^2}\right)^{3/2}\Big) = -0.004$ and -0.011 for $S^* = 10$ and $S^* = 27$

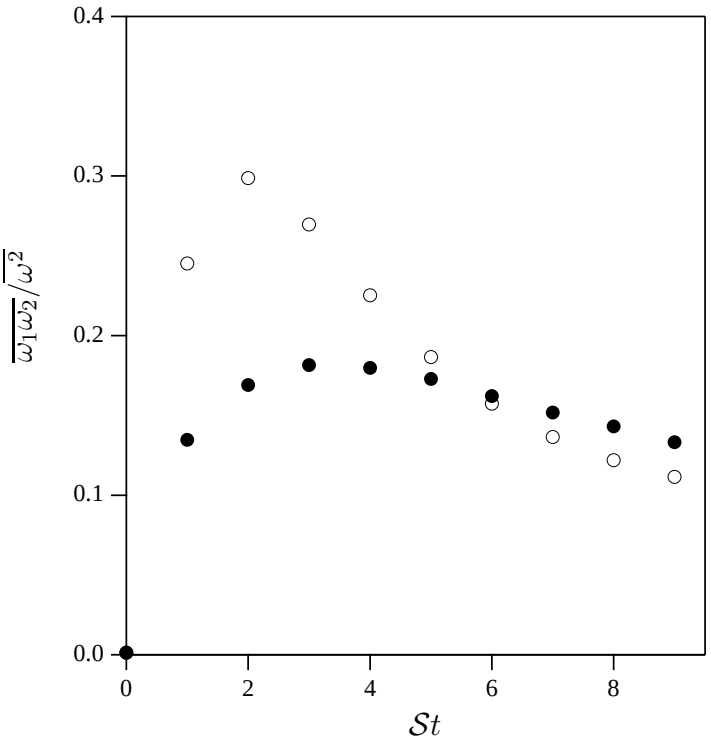

Figure 3.4: Time evolution of the cross term $\overline{\omega_1\omega_2}$ normalized by the vorticity magnitude $\overline{\omega^2}$ at • $S_0^* = 3$ and ◯ $S_0^* = 27$. Initial Reynolds number $(R_\lambda)_0 \sim 26$.

respectively. Notice that the tails of the PDF move inward with increasing S^*, approaching a Gaussian distribution.

Interestingly, the PDF of ω_2 is relatively insensitive to the shear parameter over the range of this study. In contrast, the PDF of ω_3 shows the strongest sensitivity to the shear parameter. In particular, the PDFs at both low and high shear are highly skewed ($M_3 = -0.86$ and -1.07 for $S^* = 10$ and 27 respectively). Moreover, the PDF for positive fluctuations are much more strongly influenced by the increase in the shear parameter than the PDF on the negative side. Recall that the mean vorticity associated with the uniform shear has the form $\Omega = (0, 0, -\mathcal{S})$ and hence mean shear acts *against* positive fluctuations in ω_3. With increasing shear rate those positive fluctuations are progressively reduced, while the negative

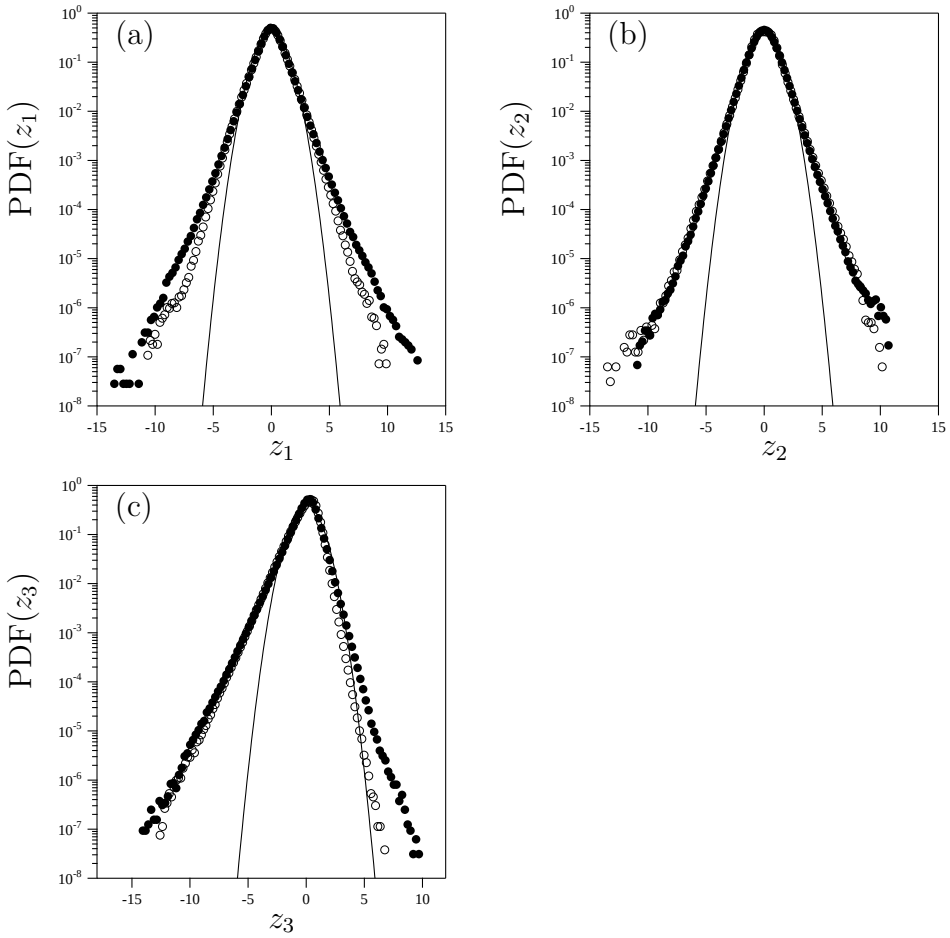

Figure 3.5: Effect of the shear parameter in the PDFs of the three components of the normalized vorticity. $z_i = \omega_i / \overline{\omega_i^2}^{1/2}$ (a) z_1 (b) z_2 and (c) z_3. The markers are: $S^* = 10$ • and $S^* = 27$ ◯. The Reynolds number is $R_\lambda \sim 68$. The solid line is a Gaussian distribution.

fluctuations are nearly unaltered. The skewness reported here is consistent with the results found by Kida and Tanaka (1992) at $S^* = 16$ (see their figure 7).

As is well known, the Reynolds number grows continuously in HTSF after the flow has reached its asymptotic state (Tavoularis and Corrsin (1981); Tavoularis and Karnik (1989); DeSouza et al. (1995); Isaza and Collins (2009); Isaza et al. (2009)). This growth impacts the shape of the tails of the PDFs. To isolate the effect of the Reynolds number on the results, we compare the PDFs of vorticity in

the self-similar regime of the flow, where the shear parameter is nearly constant and the Reynolds number is increasing. Here we report the results for $S^* = 23$ and $\mathcal{S}t = 6$ ($R_\lambda \sim 45$) and $\mathcal{S}t = 9$ ($R_\lambda \sim 68$). Figure 3.6 shows the results. The PDFs of ω_2 and ω_3 indicate that the tails of the PDFs move away from the Gaussian distribution with increasing Reynolds number. Similar results have been found for the fluctuating velocity derivatives (Garg and Warhaft (1998); Ferchichi and Tavoularis (2000); Shen and Warhaft (2000)). The spreading of the tails of the PDF of ω_3 with increasing Reynolds number also has been measured in isotropic (grid) turbulence in the range $27 \leq R_\lambda \leq 100$ by Zhou et al. (2005). The combination of results given in figures 3.5 and 3.6 show that the Reynolds number and shear parameter act in opposite ways on the intermittency of the vorticity field. That is, increasing Reynolds number leads to broader PDFs (higher intermittency) while increasing shear parameter produces the opposite trend.

3.3.2 Rate-of-Strain Statistics

This section examines the effect of S^* on the rate-of-strain tensor statistics. The PDFs of the six components of the rate-of-strain tensor in standardized coordinates are shown in figure 3.7. The PDFs are obtained in the self-similar region of the flow, with $S^* = 10$ and $S^* = 27$ and $R_\lambda = 68$ in both cases. The PDF of s_{11} is negatively skewed with skewness -0.17 and -0.89 for $S^* = 10$ and $S^* = 27$ respectively. In contrast to the trend observed with vorticity shown in figure 3.5, the PDF tail for negative values of s_{11} moves away from the Gaussian distribution with increasing shear parameter. On the other hand, the negative skewness of s_{22} goes from -0.46 for $S^* = 10$ to -0.27 for $S^* = 27$ as the tail moves towards the Gaussian distribution with increasing shear parameter. The PDF for s_{33} is

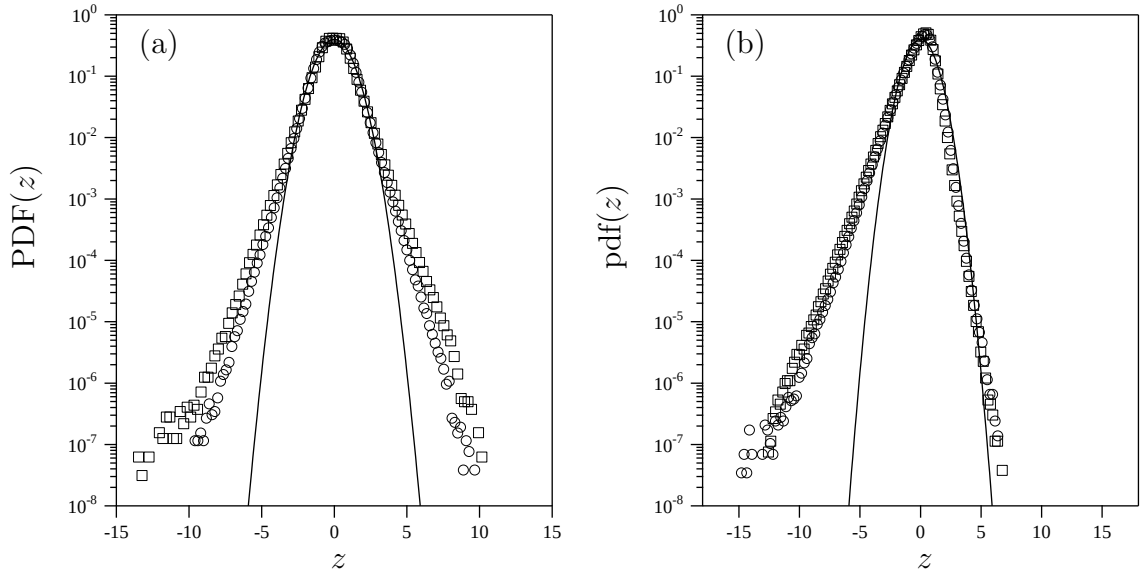

Figure 3.6: Time evolution of the PDF of the normalized vorticity (a) $z = \omega_2/\overline{\omega_2^2}^{1/2}$ and (b) $z = \omega_3/\overline{\omega_3^2}^{1/2}$ at the self-similar state of the flow with a constant value of $S^* = 27$. The symbols are ◯ for $\mathcal{S}t = 6$, $R_\lambda \sim 45$ and □ for $\mathcal{S}t = 9$, $R_\lambda \sim 68$. The solid line is a Gaussian distribution.

very similar to s_{22} with skewness values of -0.40 and -0.19 for $S^* = 10$ and $S^* = 27$ respectively. Very different behaviour is found for the PDFs of the shear components of the rate-of-strain tensor. The PDF for s_{12} is positively skewed and moves towards the Gaussian distribution with increasing shear parameter, whereas the PDF for s_{13} is nearly symmetric and independent of the shear parameter. The PDF for s_{23} too is nearly symmetric, but the tail moves towards the Gaussian distribution with increasing shear parameter.

Figure 3.8 shows $z_{11} = s_{11}/\overline{s_{11}^2}^{1/2}$ and $z_{22} = s_{22}/\overline{s_{22}^2}^{1/2}$ in a frame of reference that is rotated by 45° in the x_1–x_2 plane so that the axes align with the principal axes of the strain component of the mean shear; that is,z_{11} is now aligned with the extensional axis of the mean strain, while z_{22} is aligned with its compressional axis. Consistent with the vorticity statistics (see figure 3.5), we now see that the PDF of

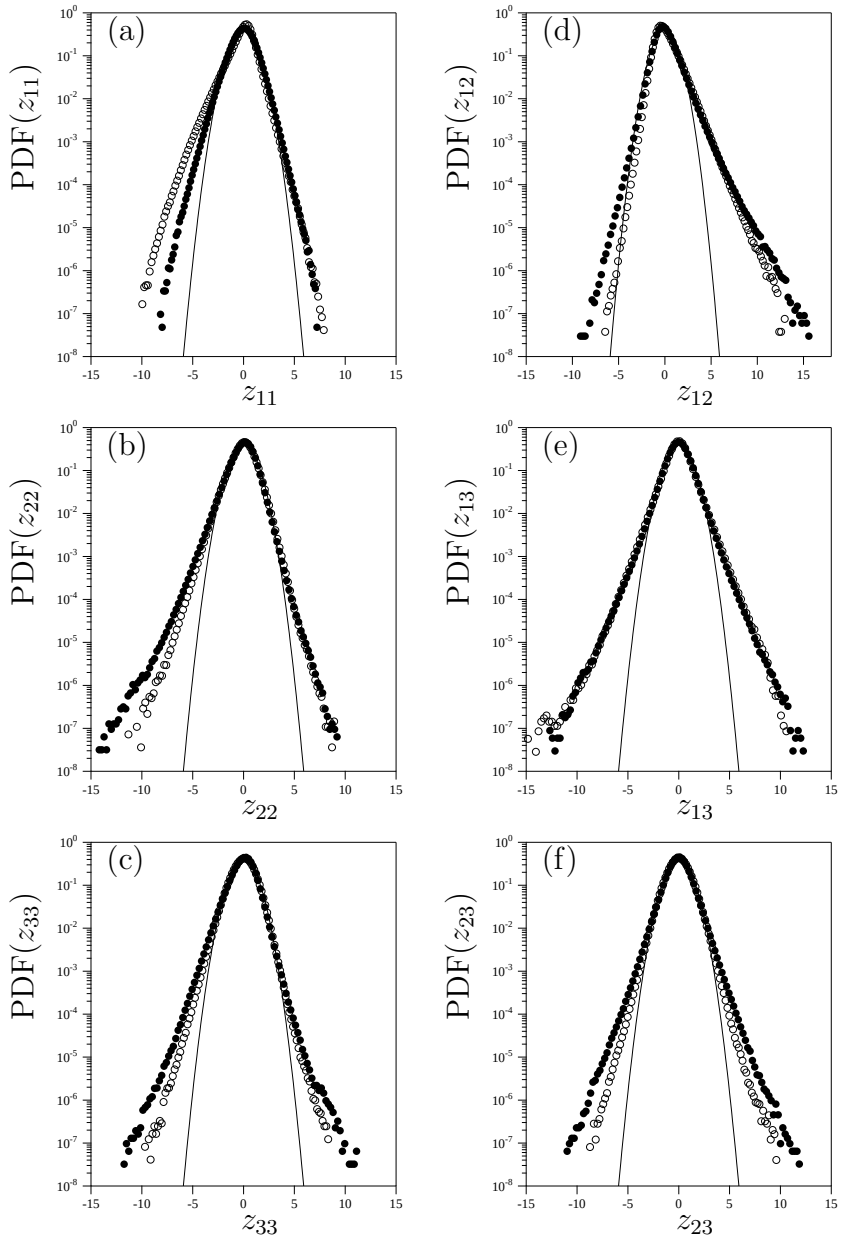

Figure 3.7: Effect of the shear parameter in the PDFs of the six components of the rate-of-strain tensor. Each component is normalized by its standard deviation. $z_{ij} = s_{ij}/\overline{s_{ij}^2}^{1/2}$ (a) z_{11}, (b) z_{22}, (c) z_{33}, (d) z_{12}, (e) z_{13} and (f) z_{23}. The markers are: • $S^* = 10$ and ◯ $S^* = 27$. The Reynolds number is $R_\lambda \sim 68$. The solid line is a gaussian distribution.

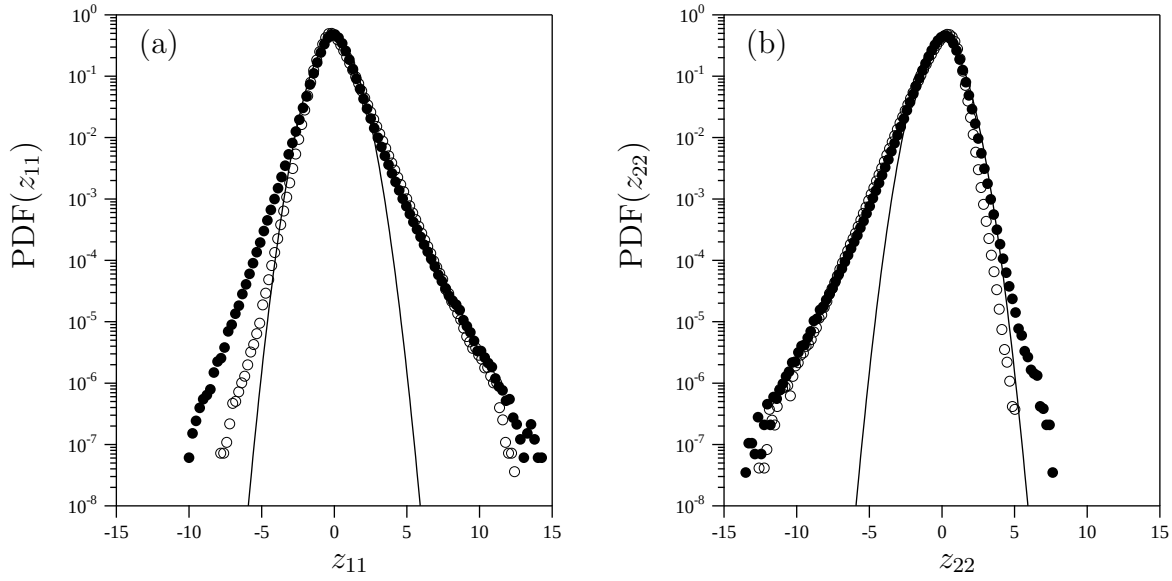

Figure 3.8: PDFs of $z_{11} = s_{11}/\overline{s_{11}^2}^{1/2}$ (left) and $z_{22} = s_{22}/\overline{s_{22}^2}^{1/2}$ for • $S^* = 10$ and ◯ $S^* = 27$ in a frame of reference rotated by 45° in the x_1–x_2 plane so that the frame axes align with the principal axes associated with the strain component of the mean shear.

each component is skewed by the mean strain. Moreover, the side of the PDF that represents fluctuations acting in opposition to the mean strain is more sensitive to the shear parameter. For z_{11} it is the negative fluctuations while for z_{22} it is the positive fluctuations. In this frame of reference, the results are qualitatively consistent with what was seen for the vorticity fluctuations (see figure 3.5).

The eigenvalues of s_{ij} play a key role on the local structure and dynamics of the rate-of-strain and vorticity fields. As with the PDFs of vorticity and strain, the shear parameter has a strong influence on its structure. At each grid point, we compute the eigenvalues (λ_1, λ_2 and λ_3) and the corresponding eigenvectors (Λ_1, Λ_2 and Λ_3) of the strain-rate tensor s_{ij}. The eigenvalues are organized as $\lambda_1 \geq \lambda_2 \geq \lambda_3$. Incompressibility requires $\lambda_1 + \lambda_2 + \lambda_3 = 0$; therefore, $\lambda_1 > 0$ and $\lambda_3 < 0$ and λ_2 could be either positive or negative depending on the magnitude of the others two

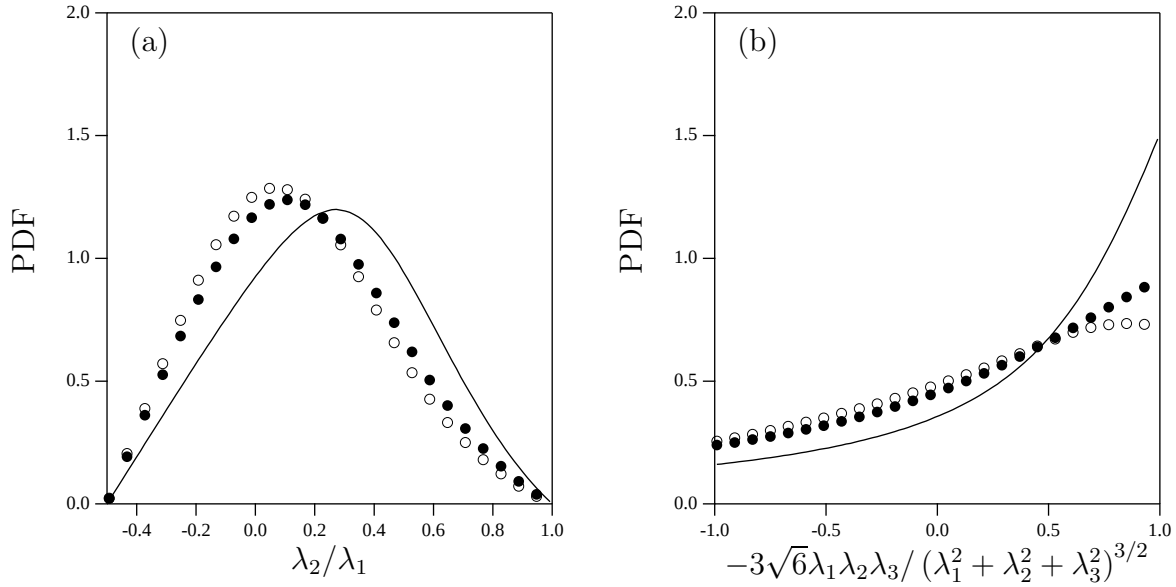

Figure 3.9: PDFs of (a) λ_2/λ_1 and (b) $-3\sqrt{6}\lambda_1\lambda_2\lambda_3/\left(\lambda_1^2+\lambda_2^2+\lambda_3^2\right)^{3/2}$. The markers are: $S^*=10$ • and $S^*=27$ ◯. The value of Reynolds number $R_\lambda=68$. The solid line is for the initial isotropic field.

It has been shown that λ_2 is predominately positive (e.g., see Ashurst et al. (1987); Tsinober et al. (1992); Su and Dahm (1996); Kholmyansky et al. (2001); Gulitski et al. (2007a)). We find that the shear parameter has no effect on the sign of λ_2. To study the relative changes in the eigenvalues quantitatively, it is useful to consider the statistics of the ratio λ_2/λ_1. Figure 3.9(a) shows the PDF of λ_2/λ_1. The most probable eigenvalue ratio $(\lambda_1:\lambda_2:\lambda_3)$ in isotropic turbulence is (3:1:-4), corresponding to $\lambda_2/\lambda_1=1/3$ (Ashurst et al. (1987)). However, the shear parameter moves the peak of the distribution to the left changing the most probable ratio to (10:1:-11) for $S^*=10$ and (17:1:-18) for $S^*=27$. Apparently the mean shear causes the rate-of-strain tensor to move towards local two-dimensionality and increases the tendency for the local formation of line-like concentrations of vorticity. Brasseur and Lin (2005) in their DNS study at $S^*=10$ found similar effects of the mean shear on the turbulence.

Table 3.1: Means and means square of the eigenvalues λ_i of the rate-of-strain tensor normalized by the mean of $s^2 = s_{ij}s_{ij} = \lambda_1^2 + \lambda_2^2 + \lambda_3^2$. Comparison with the experiments by Kholmyansky et al. (2001) and Gulitski et al. (2007a) is included.

Source	S^*	R_λ	$\overline{\lambda_1}/\overline{s^2}^{1/2}$	$\overline{\lambda_2}/\overline{s^2}^{1/2}$	$\overline{\lambda_3}/\overline{s^2}^{1/2}$
DNS	10	68	0.58	0.08	-0.66
DNS	27	68	0.57	0.07	-0.65
Gulitski et al. (2007a)	-	5300	0.51	0.09	-0.60
Kholmyansky et al. (2001)	-	10^4	0.47	0.06	-0.53
	S^*	R_λ	$\overline{\lambda_1^2}/\overline{s^2}$	$\overline{\lambda_2^2}/\overline{s^2}$	$\overline{\lambda_3^2}/\overline{s^2}$
DNS	10	68	0.39	0.04	0.56
DNS	27	68	0.41	0.03	0.56
Gulitski et al. (2007a)	-	5300	0.40	0.04	0.56
Kholmyansky et al. (2001)	-	10^4	0.47	0.06	-0.53

Table 3.1 shows the means and mean squares of the eigenvalues of the rate-of-strain tensor and compares our results with the experiments of Kholmyansky et al. (2001) (atmospheric boundary layer at $R_\lambda = 10^4$) and Gulitski et al. (2007a) (atmospheric surface layer at $R_\lambda = 5300$). The entries in the table reveal that the magnitude of λ_1 and λ_3 is much larger than λ_2 consistent with our findings.

As mentioned by Lund and Rogers (1994), λ_2/λ_1 is not appropriate to study the structure of the strain field because it vanishes at the axisymmetric limit ($\lambda_2 = 0$). Several other choices of parameters have been made in the literature (Kerr (1987); Lund and Rogers (1994); Mullin and Dahm (2006)). We use $-3\sqrt{6}\lambda_1\lambda_2\lambda_3/\left(\lambda_1^2 + \lambda_2^2 + \lambda_3^2\right)^{3/2}$, which is based on the invariants of the rate-of-strain tensor (Betchov (1956)). In isotropic turbulence the most probably state for

the flow is axisymmetric expansion (two positive principal rates of strain). However, the shear parameter has a clear effect on the structure of the strain field as can be seen in figure 3.9(b). Note that a horizontal line in these coordinates corresponds to a structure free (random) rate-of-strain tensor; hence mean shear apparently reduces the structure of HTSF relative to isotropic turbulence. For the low shear parameter case ($S^* = 10$) the most probable state is still axisymmetric expansion but the relative frequency of the state is less than in isotropic turbulence. On the other hand, the high shear parameter case ($S^* = 27$) has a maximum close to ~ 0.9, indicating that the 'limiting case' is no longer the most probable.

3.3.3 Vorticity alignments and enstrophy production

As can be seen in (3.6), the production of enstrophy $\xi \equiv \overline{\omega_i\omega_i}/2$ is given by $\mathcal{P}_s = \overline{\omega_i\omega_j s_{ij}}$ and $\mathcal{P}_r = 2\overline{\omega_1\omega_2}\mathcal{S}$. $\mathcal{P}_s$ can be conveniently written as $\overline{W_i\omega_i}$, where $W_i \equiv \omega_j s_{ij}$ is the 'stretching vector.' The alignment between W_i and ω_i therefore controls the nonlinear production rate of entstrophy. The PDF of the cosine of the angle between W_i and ω_i is shown in figure 3.10 for $S^* = 10$ and $S^* = 27$ and $R_\lambda = 68$. It is apparent that the angle is positively skewed indicating that vortex stretching is dominant over vortex compression (see Tsinober et al. (1992) for a similar results in DNS of isotropic turbulence and Gulitski et al. (2007a) for experiments in the atmospheric boundary layer). On the other hand, at the larger value of the shear parameter there is an increased tendency for misalignment of the two vectors, suggesting that $\mathcal{P}_s$ production is weakened by the stronger mean shear.

$\mathcal{P}_s$ alternatively can be written as $\overline{\omega_i\omega_j s_{ij}} = \overline{\lambda_1\omega_{\Lambda_1}^2 + \lambda_2\omega_{\Lambda_2}^2 + \lambda_3\omega_{\Lambda_3}^2}$, where ω_{Λ_i} is the vorticity vector projected onto the i^{th} eigenvector of the rate-of-strain tensor,

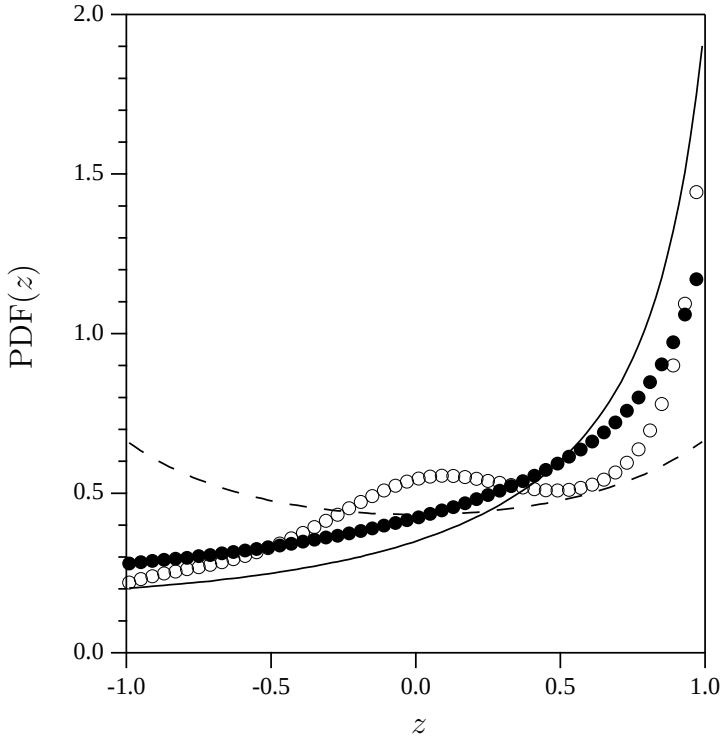

Figure 3.10: PDFs of the cosine of the angle between vorticity and the vortex stretching vector. $z = \cos(\omega, \mathbf{W}) = (\omega \cdot \mathbf{W}) / (\|\omega\| \cdot \|\mathbf{W}\|)$. $\| \ \|$ means magnitude of the quatitity. The markers are: $\bullet S^* = 10$ and $\bigcirc S^* = 27$. The value of Reynolds number $R_\lambda = 68$. The dashed line is a gaussian field. The solid line is the alignment in an isotropic flow.

Λ_i. This representation allows us to re-express $\omega_i \omega_j s_{ij}$ as

$$\omega_i \omega_j s_{ij} = \omega^2 \left[\lambda_1 \cos^2(\omega, \mathbf{\Lambda_1}) + \lambda_2 \cos^2(\omega, \mathbf{\Lambda_2}) + \lambda_3 \cos^2(\omega, \mathbf{\Lambda_3}) \right]. \tag{3.10}$$

Hence, the rate of enstrophy generation depends only on the eigenvalues and the orientation of the the vorticity with the eigenbasis of the strain field.

The reduction in $\mathcal{P}_s$ can be explained by the contribution of each of the $\overline{\lambda_\alpha \omega^2_{\Lambda_\alpha}}$ terms. Figure 3.11 shows their time evolution. For the low-shear case, the main contribution to $\mathcal{P}_s$ is from $\overline{\lambda_1 \omega^2_{\Lambda_1}}$ at all times, in agreement with the recent experiment by Gulitski et al. (2007a), whereas at high shear, the main contribution shifts from $\overline{\lambda_1 \omega^2_{\Lambda_1}}$ to $\overline{\lambda_2 \omega^2_{\Lambda_2}}$ at around $\mathcal{S}t \sim 5$. The shifting of production to $\overline{\lambda_2 \omega^2_{\Lambda_2}}$ can be

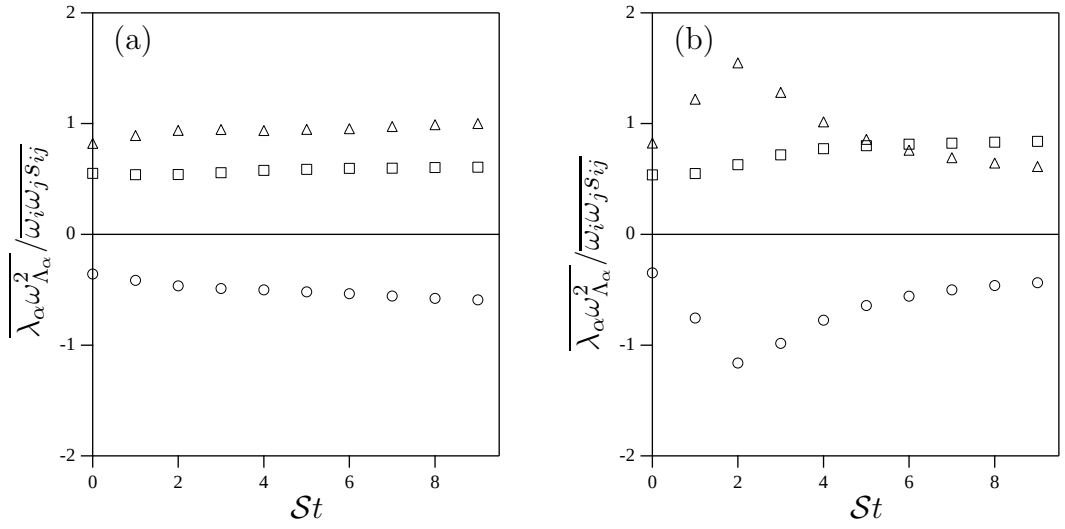

Figure 3.11: Time evolution of each of the enstrophy production terms, $\overline{\lambda_\alpha \omega^2_{\Lambda_\alpha}}$ normalized by the total enstrophy production $\overline{\omega_i \omega_j s_{ij}}$. $\triangle$ $\overline{\lambda_1 \omega^2_{\Lambda_1}}(\mathcal{S}t)$; + $\overline{\lambda_2 \omega^2_{\Lambda_2}}(\mathcal{S}t)$; and $\bigcirc$ $\overline{\lambda_3 \omega^2_{\Lambda_3}}(\mathcal{S}t)$ at (a) $S_0^* = 3$ and (b) $S_0^* = 27$. Initial Reynolds number $(R_\lambda)_0 \sim 26$. No summation in the α indices.

explained by the enhanced alignment between ω and Λ_2 along with the tendence for ω to be perpendicular to Λ_1 (which is the largest positive eigenvalue) with increasing S^*. Figure 3.12 shows the PDF of the cosine of the angle between the vorticity and the eigenvectors of the rate-of-strain tensor. We observe for low shear that the vorticity alignments are very similar to what is found in isotropic turbulence (Ashurst et al. (1987); Kholmyansky et al. (2001); Brasseur and Lin (2005); Hamlington et al. (2008)), i. e., it is preferentially aligned with the intermediate eigenvector and preferentially perpendicular to Λ_3. On the other hand, for high shear we observe the tendency for the vorticity to be perpendicular to Λ_1, which explains the reduction in the term $\overline{\lambda_1 \omega^2_{\Lambda_1}}$. For comparison, the figure includes typical results for an isotropic turbulent flow (solid line) as well as the PDF for the extreme case of no correlation (dashed line). As λ_2 has the smallest magnitude of the three eigenvalues, and the vorticity becomes progressively perpendicular to

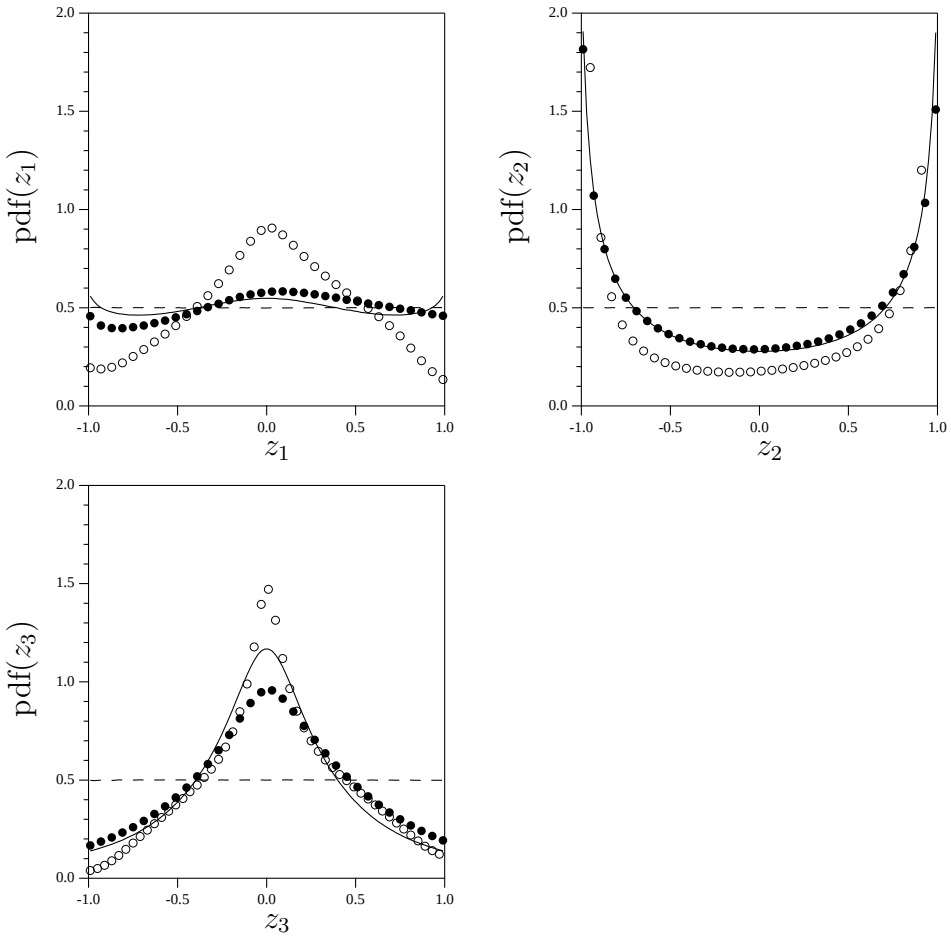

Figure 3.12: PDFs of the cosine of the angle between the vorticity and the eigenvectors of the strain-rate tensor. $z_i = \cos(\omega, \mathbf{\Lambda_i})$.The figure shows the alignment with (a) Λ_1, (b) Λ_2 and (c) Λ_3. $\bullet S^* = 10$ and $\bigcirc S^* = 27$. The value of Reynolds number $R_\lambda = 68$. The solid line is from an isotropic field. The dashed line is for a Gaussian field.

λ_1 with increasing S^*, the production of enstrophy shifts from the non-linear term $\mathcal{P}_s$ to the rapid term $\mathcal{P}_r$ (see (3.6)) with increasing shear parameter. Figure 3.13 shows the percentage of the contribution of the source terms $\mathcal{P}_s$ and $\mathcal{P}_r$ to the enstrophy in the self similar region of the flow for the two cases of shear parameter discussed before. It is clear that the production shifts to the rapid terms.

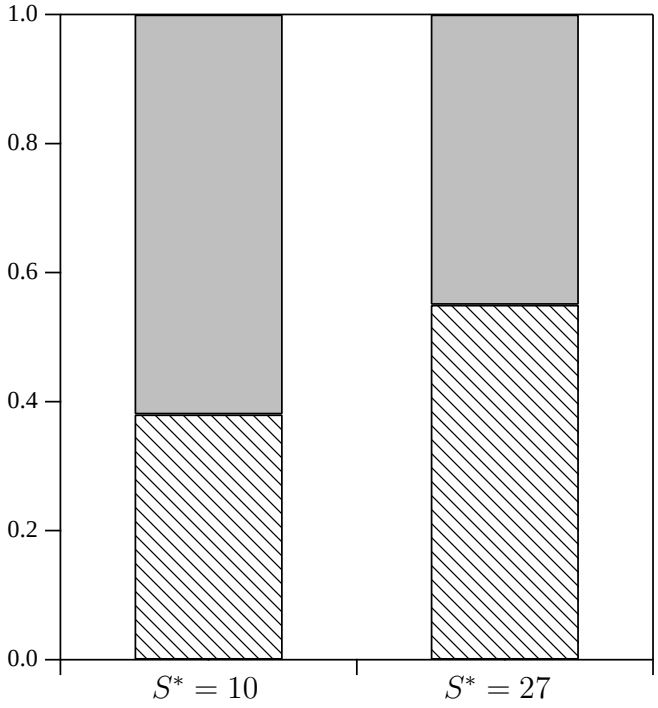

Figure 3.13: Contribution of the source terms to the enstrophy. The filled bar is the non-linear term $\mathcal{P}_s = \overline{\omega_i \omega_j s_{ij}}$, and the dashed bar is the rapid term $\mathcal{P}_r = 2\overline{\omega_1 \omega_2}\mathcal{S}$. The Reynolds number is $R_\lambda \sim 68$.

3.4 Rapid Distortion Theory

Isaza and Collins (2009) considered the behaviour of the large scales using viscous rapid distortion theory or vRDT. The vRDT equations can be solved in Fourier space yielding (Moffat (1967); Townsend (1970); Maxey (1982); Rogers (1991); Isaza and Collins (2009))

$$\hat{\mathbf{u}}'(\mathbf{k}, t) = \exp(-\Gamma)\, \mathbf{A} \cdot \hat{\mathbf{u}}'(\mathbf{k}_0, 0) \ , \tag{3.11}$$

where $\hat{\mathbf{u}}'(\mathbf{k}, t)$ is the Fourier transform of the fluctuating velocity at time t, given the initial velocity $\hat{\mathbf{u}}'(\mathbf{k}_0, 0)$. Note that the mean shear causes the wavevector $\mathbf{k}$ to be a function of time. If we define the initial wavevector as $\mathbf{k}_0 \equiv (k_1, k_2, k_3)$, then the wavevector at time t is given by $\mathbf{k} \equiv (k_1, k_2 - k_1 \mathcal{S}t, k_3)$. Γ and the

transformation matrix $\mathbf{A}$ are defined as

$$\Gamma = \nu t \left[k_0^2 - k_1 k_2 \mathcal{S} t + \frac{(k_1 \mathcal{S} t)^2}{3} \right] , \tag{3.12}$$

$$\mathbf{A}(\mathbf{k}, t) = \begin{bmatrix} 1 & \frac{k_0^2}{\left(k_1^2 + k_3^2\right)} \left(-\frac{k_3^2}{k_0^2} P + \frac{k_1^2}{k_0^2} Q \right) & 0 \\ 0 & \frac{k_0^2}{k^2} & 0 \\ 0 & \frac{k_1 k_3}{\left(k_1^2 + k_3^2\right)} (P + Q) & 1 \end{bmatrix} , \tag{3.13}$$

where $k_0^2 \equiv \mathbf{k}_0 \cdot \mathbf{k}_0$, $k^2 \equiv \mathbf{k} \cdot \mathbf{k}$, and the functions P and Q are given by

$$P = \frac{k_0^2}{k_1 \sqrt{k_1^2 + k_3^2}} \left(\arctan \alpha - \arctan \tau \right) , \tag{3.14}$$

$$Q = \frac{\mathcal{S} t \left(k_0^2 - 2 k_2^2 + k_1 k_2 \mathcal{S} t \right)}{k^2} . \tag{3.15}$$

The angles α and τ are

$$\alpha = \frac{k_2}{\sqrt{k_1^2 + k_3^2}} \quad , \quad \tau = \frac{k_2 - k_1 \mathcal{S} t}{\sqrt{k_1^2 + k_3^2}} . \tag{3.16}$$

In the previous study, Isaza and Collins (2009) focused on low-order moments of large-scale turbulence statistics that could be written in closed form in terms of integrals of (3.11). However, here we are interested in the PDF of the rate-of-strain tensor, vorticity and eigenvector alignments. While the PDF information can be extracted from (3.11) for a particular initial condition $\mathbf{u}'(\mathbf{k}_0, 0)$, we were not able to write down a general expression for the PDF or how it evolves. We applied (3.11) to the initial velocity field used throughout this study and analyzed the statistics of the vorticity and rate-of-strain tensor at different times.

Section §3.3.1 shows that the tails of the PDF of the vorticity move inwards with increasing shear parameter. The same trend is capture by vRDT. Figure 3.14 which shows the PDF of $z = \omega_1 / \overline{\omega_1^2}^{1/2}$ for $S^* = 27$ and $S^* = 54$. This suggests a direct effect of the large-scale anisotropy on the small scales. The coupling

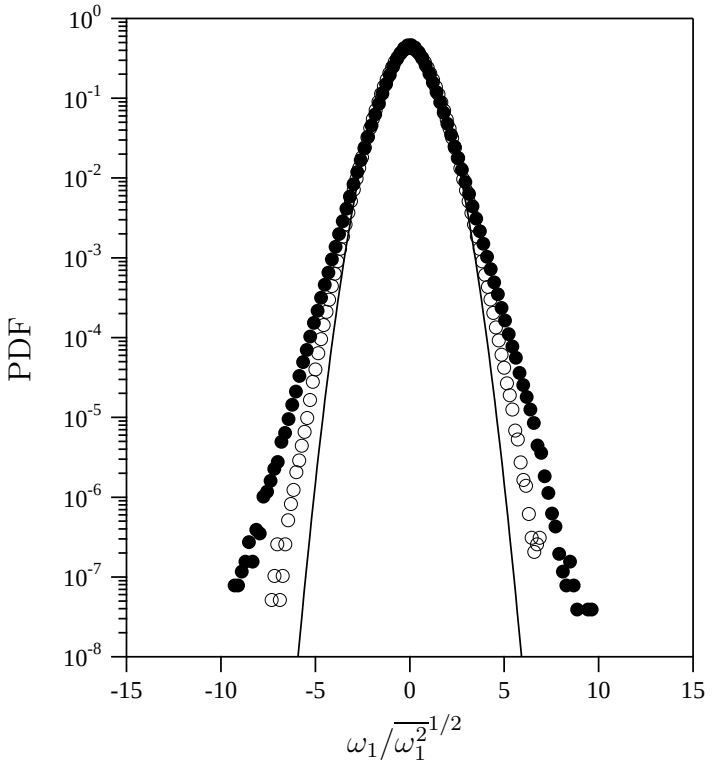

Figure 3.14: Effect of the shear parameter on the PDF of $z = \omega_1/\overline{\omega_1^2}^{1/2}$ as predicted by vRDT. The markers are: • $S^* = 27$ and ◯ $S^* = 54$. The Reynolds number is $R_\lambda \sim 68$. The solid line is a Gaussian distribution.

between the large and small scales has also been studied by Brasseur and Yeung (1991) in the context of 'distant' triadic interactions of the Fourier coefficients, indicating that the structure of the small scales is modulated by the anisotropy of the large energy-containing scales. Ayyalasomayajula and Warhaft (2006) also suggest a direct interaction of the large scales upon the small scales to explain results obtained in their irrotational axisymmetric strain experiment.

On the other hand, the linear theory misses completely the trend with increasing Reynolds number (or increasing time). Figure 3.15 shows the time evolution of the PDF $z = \omega_1/\overline{\omega_1^2}^{1/2}$. The theory predicts the vorticity PDF evolves towards a Gaussian distribution with time. Since the wavevectors $\mathbf{k}$ evolve as $k_2(t) \sim -\mathcal{S}t$,

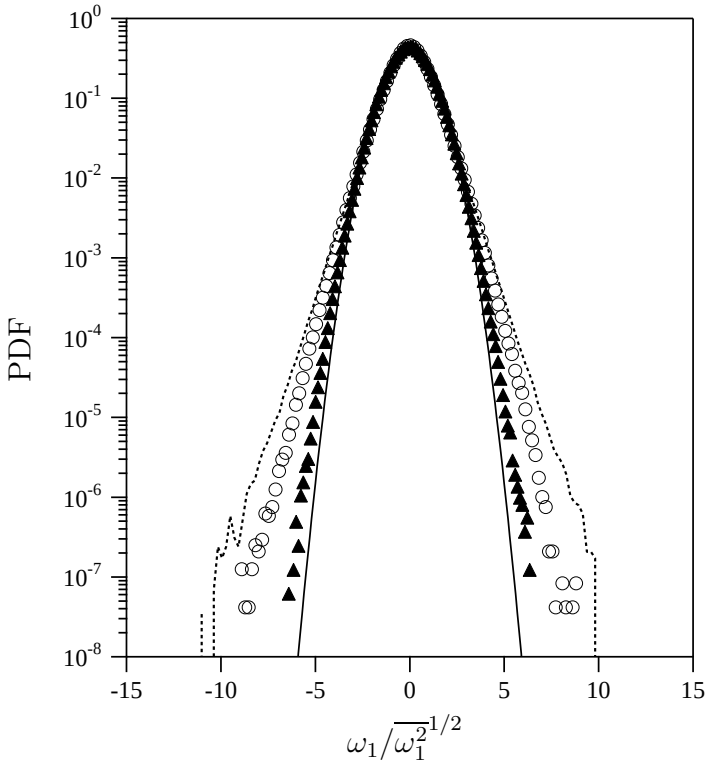

Figure 3.15: Time evolution of the normalized PDFs of the vorticity component ω_1 from RDT. The markers are: dashed-line $\mathcal{S}t = 0$, ◯ $\mathcal{S}t = 1$ and ▲ $\mathcal{S}t = 3$. The Reynolds number at $\mathcal{S}t = 0$ is $R_\lambda \sim 26$. The solid line is a Gaussian distribution. The initial condition is isotropic turbulence.

Fourier coefficients that are initially close together, become more distant with increasing time. This progressive scrambling of the correlations in Fourier space in time leads to a near-random sum of Fourier coefficients at longer times, which is Gaussian. However, in the full Navier-Stokes (DNS) this effect is counterbalanced by the growing nonlinear interactions among the Fourier coefficients which retains, and possibly enhances, those correlations, preventing the PDFs from becoming Gaussian.

The application of vRDT to small-scale statistics such as vorticity and strain is qualitatively different than its application to large-scale statistics (Isaza and Collins (2009)). It is possible to imagine a flow that is initially rapid at all scales,

Table 3.2: Flow parameters for the experiments in the self similar region of the flow. The measurements are made at the center of the tunnel and downstream distance of $x/h = 116.3$. The kinematic viscosity ν is 1.5×10^{-5} m^2/s.

$\mathcal{S}$ (s^{-1})	33
$-\rho_{uv}$	0.44
R_λ	200
ϵ (m^2/s^3)	2.4
$l = u^3/\epsilon$ (m)	0.069
$\mathcal{P}/\epsilon$	1.25
$S^* = \mathcal{S}q^2/\epsilon$	9.6

such that $\mathcal{S}\tau_\eta \gg 1$, or equivalently $S_0^* \gg R_\lambda$. While vRDT predicts the indefinite growth of S^* ensuring the large scales remain in the rapid regime for all time, it also predicts the exponential growth of ϵ and hence $\mathcal{S}\tau_\eta$ will decrease exponentially in time. Thus, vRDT predicts the small scales must eventually fall out of the rapid regime, implying vRDT will no longer apply to the small scales. This inherent breakdown of the vRDT assumptions at the small scales implies the nonlinear terms eventually balance the rapid terms and the small scales should approach an equilibrium state that is similar to the slowly-sheared case. At long times, we expect that the small scales return to being functions of the Reynolds number only and are independent of the shear parameter. We are not able to simulate the turbulence for a long enough time to test this conjecture.

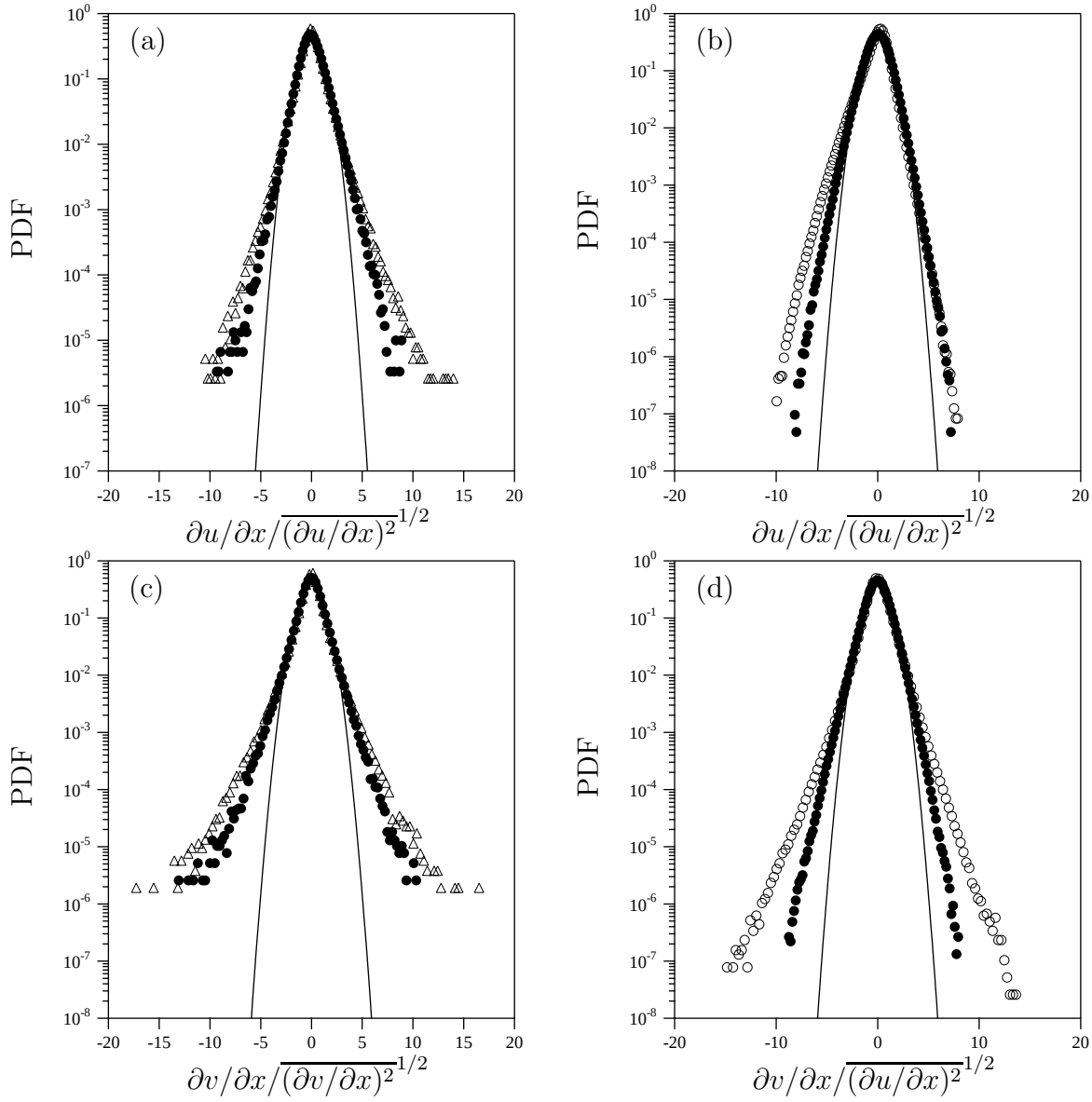

Figure 3.16: PDFs of $\partial u/\partial x$ and $\partial v/\partial x$ for experiments (a) and (c), and DNS (b) and (d). The experimental conditions are • $S^* \sim 9.6, R_\lambda \sim 200$ and △ $S^* \sim 15, R_\lambda \sim 225$. The DNS conditions are • $S^* = 10$ and ◯ $S^* = 27$. The Reynolds number is $R_\lambda \sim 68$. The solid line is a Gaussian distribution.

3.5 Comparison with Experiments

In a previous study (Isaza et al. (2009)), the authors performed experimental measurements of nearly homogeneous turbulent shear flow in a vertical, open circuit wind tunnel facility outfitted with an active grid (Mydlarski and Warhaft (1996)) to control the level of turbulence followed by a screen with varying solidity to create the uniform shear. The setup is similar to the one used by Garg and Warhaft (1998). The interested reader is referred to Isaza et al. (2009) for the details of the experiment. Table 3.2 gives a summary of the conditions of the experimental runs. As you can see, we are able to achieve $S^* \sim 10$, which matches the asymptotic value of our DNS at low shear. Due to limitations of the experiment, it is not possible to achieve as high a shear parameter as in the simulations. In contrast, the DNS is run at a much lower Reynolds number ($R_\lambda \sim 68$) than the experiment ($R_\lambda \sim 200$); however, Kholmyansky et al. (2001) and recently Gulitski et al. (2007a,b) showed that the basic physics of the turbulence is at least qualitatively the same at moderate and high Reynolds numbers. In the experiments we employ an 'X-wire' that measures the u and v components of velocity simultaneously. From these measurements we are able to deduce one component of the rate-of-strain tensor (s_{11}) and no components of the vorticity. Hence we focus our comparisons on the statistics we are able to measure, namely $s_{11} \equiv \partial u/\partial x$ and one component of shear, $\partial v/\partial x$.

Figure 3.16 shows the PDFs of $\partial u/\partial x$ and $\partial v/\partial x$ taken at the self similar region of the flow for the experiments and the DNS. The results indicate that with increasing shear, the tails of the PDFs move away from the Gaussian distribution. Notice that the data for the DNS and experiments shows the same trend. Interestingly the PDF of $\partial u/\partial x$ for the high shear case ($S^* = 27$) shows a larger negative skewness. This is due to a reduction of the positive contributions to the PDF due

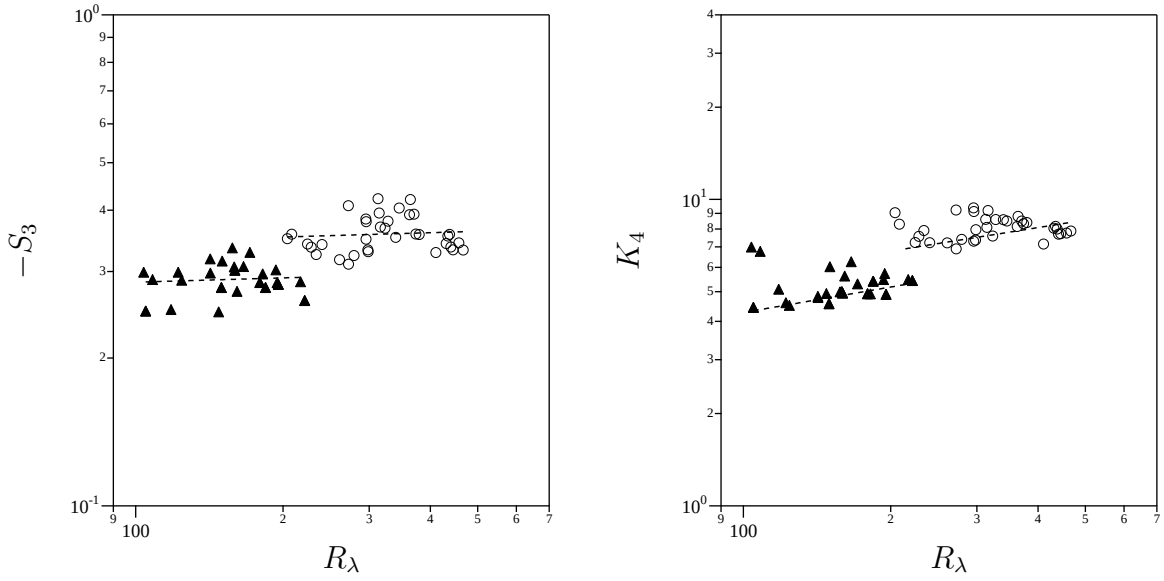

Figure 3.17: The normalized moments: $-S_3 = \overline{(\partial u/\partial x)^3}/\overline{(\partial u/\partial x)^2}^{3/2}$ and $K_4 = \overline{(\partial u/\partial x)^4}/\overline{(\partial u/\partial x)^2}^2$. Solid symbols $S^* = 10$, open symbols $S^* = 16$. The fit to the curves for $S^* = 10$ are $S_3 = 0.25R_\lambda^{0.03}$ and $K_4 = 1.2R_\lambda^{0.27}$, and for $S^* = 16$ are $S_3 = 0.30R_\lambda^{0.03}$ and $K_4 = 1.8R_\lambda^{0.26}$.

to the mean strain, as discussed in §3.3.2.

Another manifestation of the influence of S^* can be seen in the higher-order moments of the derivatives. Experimentally Shen and Warhaft (2000) and Gylfason et al. (2004) showed that the skewness $-S_3 = \overline{(\partial u/\partial x)^3}/\overline{(\partial u/\partial x)^2}^{3/2}$ and flatness $K_4 = \overline{(\partial u/\partial x)^4}/\overline{(\partial u/\partial x)^2}^2$ grow with increasing Reynolds number following a power law $\sim AR_\lambda^n$. Additionally, Gylfason et al. (2004) suggested that the prefactor in the power law may be a function of the amount of shear in the flow. However, due to their measurement error they were unable to test this conjecture. Figure 3.17 shows our measurements of the prefactor for the two experimental cases described above. The results indicate that the prefactor is indeed a function of the shear parameter, while the exponent is not. Least squares fits to the curves yield: $S_3 = 0.25R_\lambda^{0.03}$ and $K_4 = 1.2R_\lambda^{0.27}$ for $S^* = 10$ and $S_3 = 0.30R_\lambda^{0.03}$

and $K_4 = 1.8R_\lambda^{0.26}$ for $S^* = 16$. Consistent with the conjecture of Gylfason et al. (2004), we find that the prefactor is S^* dependent, while the power is not.

3.6 Conclusions

In this study, we investigated the effect of the shear parameter on velocity-gradient statistics of homogeneous turbulent shear flow using a combination of direct numerical simulations, viscous rapid distortion theory and experiments. The DNS were performed using a code that allowed the shear rate to be varied over a wide range (Brucker et al. (2007)). Over the window of time that the simulations retain good resolution of large and small scales, DNS shows that the shear parameter has a direct effect on the PDF of the components of the vorticity vector and the rate-of-strain tensor. In particular, with increasing shear parameter we find that the width of the distributions of ω_1 and ω_3 are reduced (the effect on ω_2 is much weaker). Moreover, the skewness in the PDF of ω_3 increases with increasing S^*, as fluctuations that oppose the mean vorticity are more strongly damped. We see similar results for the rate-of-strain tensor if we rotate the coordinate system 45 degrees in the x_1–x_2 plane so that the coordinates are aligned with the mean strain. We looked at the alignment of the vorticity relative to the local orientation of the three eigenvectors of the rate-of-strain tensor. It's been known for a long time that in isotropic turbulence vorticity aligns most strongly with the eigenvector corresponding to the intermediate eigenvalue. We find that alignment is enhanced with increasing shear parameter. Furthermore, the misalignment of vorticity and the eigenvector corresponding to the largest eigenvalue also grows with increasing S^*. The combination of effects causes the production of enstrophy to progressively shift from the nonlinear production term $\mathcal{P}_s$ to the rapid production term $\mathcal{P}_r$ with

increasing shear parameter.

We analyzed the influence of S^* using viscous rapid distortion theory. The theory correctly predicts the PDF of the vorticity and rate-of-strain tensor approaches a Gaussian distribution with increasing S^*. However, vRDT fails to capture the correct trend of the tails of the PDFs with increasing Reynolds number. The cause of the failure of the theory at small scales is qualitatively different than the discussion given in Isaza and Collins (2009) for the failure of vRDT at long times for the large scales. In particular, since the small scales grow smaller in time (at any S^*) causing $\mathcal{S}\tau_\eta$ to decrease with time, the small scales eventually are no longer in the 'rapid' regime. In the longtime limit, we expect the small scales to behave as turbulence that is weakly sheared and hence the nonlinear terms to be important.

The DNS results are in qualitative agreement with the experiments by Isaza et al. (2009). Namely the 'tails' of the PDF of $\partial u/\partial x$ and $\partial v/\partial x$ show the same trend with increasing shear parameter as the experiments. We show that the prefactors of the power laws for $-S_3 \sim A_S R_\lambda^{n_S}$ and $K_4 \sim A_K R_\lambda^{n_K}$ are functions of the shear parameter, confirming the conjecture by Gylfason et al. (2004).

This work was supported by the National Science Foundation under grants PHY-0554675 and CBET-0756510. JCI was partially supported by a fellowship from the Fulbright Commission.

BIBLIOGRAPHY

Ashurst, W. T., Kerstein, A. R., Kerr, R. M., & Gibson, C. H. (1987). Alignment of vorticity and scalar gradient with strain rate in simulated Navier-Stokes turbulence. *Phys. Fluids* **30**(8), 2343–2353.

Ayyalasomayajula, S. & Warhaft, Z. (2006). Nonlinear interactions in axisymmetric strained grid turbulence. *J. Fluid Mech.* **566**, 273–307.

Betchov, R. (1956). An inequality concerning the production of vorticty in isotropic turbulence. *J. Fluid Mech.* **1**, 497–504.

Brasseur, J. G. & Lin, W. (2005). Kinematics and dynamics of small-scale vorticity and strain-rate structures in the transition from isotropic to shear turbulence. *Fluid Dynamics Research* **36**, 357–384.

Brasseur, J. G. & Yeung, P. K. (1991). Large and small-scale coupling in homogeneous turbulence: Analysis of the Navier-Stokes equation in the asymptotic limit. In *Eighth Symposium on Turbulent Shear Flow*.

Browne, L. W. B., Antonia, R. A., & Chua, L. P. (1989). Calibration of x-probes for turbulent flow measurements. *Exp. Fluids* **7**, 201–208.

Brucker, K. A., Isaza, J. C., Vaithianathan, T., & Collins, L. R. (2007). Efficient algorithm for simulating homogeneous turbulent shear flow without remeshing. *J. Comp. Phys.* **225**, 20–32.

Champagne, F. H., Harris, G. V., & Corrsin, S. (1970). Experiments on nearly homogeneous turbulent shear flow. *J. Fluid Mech* **41**, 81–139.

Comte-Bellot, G. & Corrsin, S. (1966). The use of a contraction to improve the isotropy of grid-generated turbulence. *J. Fluid Mech.* **25**, 657–682.

Comte-Bellot, G. & Corrsin, S. (1971). Simple Eulerian time correlation of full- and narrow-band velocity signals in grid-generated 'isotropic' turbulence. *J. Fluid Mech.* **48**, 273–337.

Deissler, R. G. (1961). Effects of inhomogeneity and of shear flow in weak turbulent fields. *Phys. Fluids* **4**(10), 1187–1198.

Deissler, R. G. (1970). Effect of initial condition on weak homogeneous turbulence with uniform shear. *Phys. Fluids* **13**(7), 1868–1869.

DeSouza, F. A., Nguyen, V. D., & Tavoularis, S. (1995). The structure of highly sheared turbulence. *J. Fluid Mech.* **303**, 155–167.

Ferchichi, M. & Tavoularis, S. (2000). Reynolds number effect on the fine structure of uniformly sheared turbulence. *Phys. Fluids* **12**(11), 2942–2953.

Fox, J. (1964). Velocity correlations in weak turbulent shear flow. *Phys. Fluids* **7**(4), 562–564.

Garg, S. & Warhaft, Z. (1998). On small scale statistics in a simple shear flow. *Phys. Fluids* **10**, 662–673.

Gulitski, G., Kholmyansky, M., Kinzelbach, W., Luthi, B., Tsinober, A., & Yorish, S. (2007a). Velocity and temperature derivatives in high-Reynolds-number turbulent flows in the atmospheric surface layer. Part 1. Facilities, methods and some general results. *J. Fluid Mech.* **589**, 57–81.

Gulitski, G., Kholmyansky, M., Kinzelbach, W., Luthi, B., Tsinober, A., & Yorish, S. (2007b). Velocity and temperature derivatives in high-Reynolds-number turbulent flows in the atmospheric surface layer. Part 2. Acceleration and related matters. *J. Fluid Mech.* **589**, 83–102.

Gylfason, A., Ayyalasomayajula, S., & Warhaft, Z. (2004). Intermittency, pressure and acceleration statistics from hot-wire measurements in wind-tunnel turbulence. *J. Fluid Mech.* **501**, 213–229.

Hamlington, P. E., Schumacher, J., & Dahm, W. J. A. (2008). Direct assessment of vorticity alignment with local and nonlocal strain rates in turbulent flows. *Phys. Fluids* **20**(11), 111703.

Harris, G. V., Graham, A. J., & Corrsin, S. (1977). Further experiments in nearly homogeneous shear flow. *J. Fluid Mech.* **81**, 657–687.

Heskestad, G. (1965). A generalized Taylor hypothesis with application for high Reynolds number turbulent shear flows. *J. Appl. Mech.* **87**, 735–739.

Hunt, J. C. R. & Carruthers, D. J. (1990). Rapid distorition theory and the problems of turbulence. *J. Fluid Mech.* **212**, 497–532.

Isaza, J. C. & Collins, L. R. (2009). On the asymptotic behaviour of large-scale turbulence in homogeneous shear flow. *J. Fluid Mech.*. in review.

Isaza, J. C., Warhaft, Z., & Collins, L. R. (2009). Experimental investigation of the large-scale velocity statistics in homogeneous turbulent shear flow. *Phys. Fluids*. in press.

Ishihara, T., Gotoh, T., & Kaneda, Y. (2009). Study of high-Reynolds-number isotropic turbulence by direct numerical simulation. *Ann. Rev. Fluid Mech.* **41**, 165–180.

Jacobitz, F. G. & Sarkar, S. (1999). On the shear number effect in stratified shear flow. *Theoretical and Computational Fluid Dynamics* **13**(3), 171–188.

Jacobitz, F. G., Sarkar, S., & van Atta, C. W. (1997). Direct numerical simulations of the turbulence evolution in a uniformly sheared and stably stratified flow. *J. Fluid Mech.* **342**, 231–261.

Kerr, R. M. (1987). Histograms of helicity and strain in numerical turbulence. *Phys. Rev. Lett.* **59**, 783–786.

Kholmyansky, M., Tsinober, A., & Yorish, S. (2001). Velocity derivatives in the atmospheric surface layer at re[sub lambda] = 10[sup 4]. *Phys. Fluids* **13**(1), 311–314.

Kida, S. & Tanaka, M. (1992). Reynolds stress and vortical structure in a uniformly sheared turbulence. *Journal of the Physical Society of Japan* **61**(12), 4400–4417.

Kida, S. & Tanaka, M. (1994). Dynamics of vortical structures in a homogeneous shear flow. *J. Fluid Mech.* **274**, 43–68.

Lee, M. J., Kim, J., & Moin, P. (1990). Structure of turbulence at high shear rate. *J. Fluid Mech.* **216**, 561–583.

Lee, W. G. & Chung, M. K. (1995). The equilibrium states and the stability analysis of Reynolds stress equations for homogeneous turbulent shear flows. *Phys. Fluids* **7**(11), 2807–2819.

Lumley, J. L. (1964). Spectral energy budget in wall turbulence. *Phys. Fluids* **7**(2), 190–196.

Lumley, J. L. & Panofsky, H. A. (1964). *The Structure of Atmospheric Turbulence*. Interscience Publishers New York.

Lund, T. S. & Rogers, M. M. (1994). An improved measure of strain state probability in turbulent flows. *Phys. Fluids* **6**(5), 1838–1847.

Maxey, M. R. (1982). Distortion of turbulence in flows with parallel streamlines. *J. Fluid Mech.* **124**, 261–282.

Moffat, H. K. (1967). The interaction of turbulence with strong wind shear. In A. M. Yaglom and V. I. Tatarsky (Eds.), *Proceedings of the International Colloquium on Atmospheric Turbulence and Radio Wave Propagation*.

Mullin, J. A. & Dahm, W. J. A. (2006). Dual-plane stereo particle image velocimetry measurements of velocity gradient tensor fields in turbulent shear flow. II. Experimental results. *Phys. Fluids* **18**(3), 035102.

Mydlarski, L. & Warhaft, Z. (1996). On the onset of high-Reynolds-number grid-generated wind tunnel turbulence. *J. Fluid Mech.* **320**, 331–368.

Pope, S. B. (2000). *Turbulent Flows*. Cambridge University Press New York.

Press, W. H., Teukolsky, S. A., Vetterling, W. T., & Flannery, B. P. (1999). *Numerical Recipies in Fortran*. Cambridge University Press Cambridge.

Rogallo, R. S. (1981). Numerical experiments in homogeneous turbulence. Technical Report 81315 NASA.

Rogers, M. M. (1991). The structure of passive scalar field with uniform mean gradient in rapidly sheared homogeneous turbulent flow. *Phys. Fluids A* **3**(1), 144–154.

Rogers, M. M., Moin, P., & Reynolds, W. C. (1986). The structure and modeling of the hydrodynamics and passive scalar fields in homogeneous tur-

bulent shear flow. Technical Report TF-25 NASA Ames Center for Turbulence Research.

Rohr, J. J., Itsweire, E. C., Helland, K. N., & van Atta, C. W. (1988). An investigation of the growth of turbulence in a uniform-mean-shear flow. *J. Fluid Mech.* **187**, 1–33.

Rose, W. G. (1966). Results of an attempt to generate a homogeneous turbulent shear flow. *J. Fluid Mech.* **25**, 97–120.

Rose, W. G. (1970). Interaction of grid turbulence with a uniform mean shear. *J. Fluid Mech.* **44**, 767–779.

Rotta, J. (1951). Statistische theorie nichthomogener turbulenz 1. *Z. Phys.* **129**, 547–572.

Saddoughi, S. G. & Veeravalli, S. V. (1994). Local isotropy in turbulent boundary layers at high Reynolds number. *J. Fluid Mech.* **268**, 333–372.

Savill, A. M. (1987). Recent developments in rapid-distortion theory. *Ann. Rev. Fluid Mech.* **19**, 531–573.

Schumacher, J. (2004). Relation between shear parameter and Reynolds number in statistically stationary turbulent shear flows. *Phys. Fluids* **16**, 3094–3102.

Schumacher, J., Sreenivasan, K. R., & Yeung, P.-K. (2003). Derivative moments in turbulent shear flow. *Phys. Fluids* **15**, 84–90.

Shen, X. & Warhaft, Z. (2000). The anisotropy of small scale structure in high Reynolds number (R_λ) turbulent shear flow. *Phys. Fluids* **12**, 2942.

Shih, L. H., Koseff, J. R., Ferziger, J. H., & Rehmann, C. R. (2000). Scaling and parameterization of stratified homogeneous turbulent shear flow. *J. Fluid Mech.* **412**, 1–20.

Sirivat, A. & Warhaft, Z. (1983). The effect of a passive cross–stream temperature gradient on the evolution of temperature variance and heat flux in grid turbulence. *J. Fluid Mech.* **128**, 323–346.

Su, L. K. & Dahm, W. J. A. (1996). Scalar imaging velocimetry measurements of the velocity gradient tensor field in turbulent flows. II. Experimental results. *Phys. Fluids* **8**(7), 1883–1906.

Tavoularis, S. (1985). Asymptotic laws for transversely homogeneous turbulent shear flows. *Phys. Fluids* **28**(3), 999–1001.

Tavoularis, S., Bennett, J. C., & Corrsin, S. (1978). Velocity-derivative skewness in small Reynolds number, nearly isotropic turbulence. *J. Fluid Mech.* **88**, 63–69.

Tavoularis, S. & Corrsin, S. (1981). Experiments in nearly homogeneous turbulent shear flow with a uniform mean temperature gradient. Part 1. *J. Fluid Mech.* **104**, 311–347.

Tavoularis, S. & Karnik, U. (1989). Further experiments on the evolution of turbulent stresses and scales in uniformly sheared turbulence. *J. Fluid Mech.* **204**, 457–478.

Thacker, W. D., Grosh, C. E., & Gatski, T. B. (1999). Modeling the dynamics of ensemble-averaged linear disturbances in homogeneous shear flow. *Flow, Turbulence and Combustion* **63**, 39–58.

Townsend, A. A. (1970). Entrainment and the structure of turbulent flow. *J. Fluid Mech.* **14**, 13.

Townsend, A. A. (1976). *The Structure of Turbulent Shear Flow*. Cambridge University Press Cambridge.

Tsinober, A., Kit, E., & Dracos, T. (1992). Experimental investigation of the field of velocity gradients in turbulent flows. *J. Fluid Mech.* **242**, 169–192.

Yu, D. & Girimaji, S. S. (2005). DNS of homogeneous shear turbulence revisited with the lattice Boltzmann method. *J. of Turbulence* **6**, 1–17.

Zhou, T., Antonia, R. A., & Chua, L. P. (2005). Flow and Reynolds number dependencies of one-dimensional vorticity fluctuations. *J. Turbul.* **6**(28), 1–17.